

UCSF

UC San Francisco Electronic Theses and Dissertations

Title

Magnetic resonance imaging of the heart

Permalink

<https://escholarship.org/uc/item/0k34r0cv>

Author

Thompson, Michael Aaron

Publication Date

1995

Peer reviewed|Thesis/dissertation

**MAGNETIC RESONANCE IMAGING OF THE HEART:
METHODOLOGIES AND FUNCTIONAL ANALYSIS**

by

MICHAEL AARON THOMPSON

DISSERTATION

Submitted in partial satisfaction of the requirements for the degree of

DOCTOR OF PHILOSOPHY

in

BIOENGINEERING

in the

GRADUATE DIVISION

of the

UNIVERSITY OF CALIFORNIA

San Francisco

Date

University Librarian

Degree Conferred:

COPYRIGHT © 1995
BY
MICHAEL AARON THOMPSON

11007 11007 11007

ACKNOWLEDGMENTS

It is a truly wonderful feeling to finally complete my doctoral dissertation. I could not have achieved this very important goal without the assistance of many individuals who have inspired, supported, and advised me over the years. Without their efforts I would certainly have been unable to complete this achievement. My heartfelt gratitude is extended to each and everyone of these individuals.

Several persons deserve special mention. The first of these individuals is Dr. Leon Kaufman. As my research advisor and dissertation committee chairman Dr. Kaufman helped set the course and provided the work environment I required to complete my doctoral degree. I would like to express my thanks to him for the support and patience he has offered me during my time at the UCSF-RIL.

Dr. Douglas Ortendahl has been a valued friend and advisor whose hard work and kind nature has positively influenced my dissertation beyond measure. Thank you very much Doug for everything. I would also like to thank Dr. Lawrence Crooks for his careful reading of my dissertation. His efforts without a doubt improved my dissertation. Dr. Crooks has also spent a large amount of time with me sharing his expertise in magnetic resonance imaging. It is rare to find such a generous person and I am very grateful to you Larry for all that you have taught me.

Dr. Steve Lehman has been my academic advisor, a participant in my qualifying exam, and now finally a reader of my Ph.D. dissertation. In

each of these roles he has challenged and guided me along my research path. I will always be very grateful to him for his support and effort on my behalf.

The echocardiographic cardiac functional parameters presented in this dissertation were made possible by the generosity of Dr. Nelson Schiller and Laura Kee. I am especially grateful to Laura for her hard and professional work on my behalf.

The UCSF-RIL has been a unique environment for the pursuit of a doctoral degree. The efforts of the UCSF-RIL staff were crucial to my completion of this dissertation research. I am grateful to all of them for their assistance and support. Principal on this list is Minaise A. Minaise. His impressive efforts in the design and creation of the real time oblique image display program were a tremendous resource to me and a credit to himself. I wish Minaise and his growing family good health, good fortune, and the happiness they surely deserve. I would also like to express my thanks to Phil Sheldon for allowing me to use some of his artistic illustrations in my dissertation.

Outside of my doctoral research I was given a great deal of support from some very special people including Ajit Shah Ph.D. I first met Dr. Shah when we were graduate students together at the UCSF-RIL. I very much miss the days when we could explain and solve all of the world's problems in the car driving over the bay bridge, or on the golf course. Thank you for your support and friendship over the last years. Thanks also to my

fellow graduate students. We shared many fun and interesting adventures together and you were always a source of support for me.

Finally I would like to thank my family for their love and support over these long and trying years. My mother Sharon Thompson, my father Asher Thompson, his wife Cathy Roland-Thompson, Shelly, Blake, Karen, and Marcie – you mean a great deal to me and I love you very much. Lastly, very special recognition goes to Margaret Wong. Thank you Margaret for your support, guidance, and love over the last years. I love you very much and guess what, I am done!!

1100F 11DDNDV

**MAGNETIC RESONANCE IMAGING OF THE HEART:
METHODOLOGIES AND FUNCTIONAL ANALYSIS
BY
MICHAEL AARON THOMPSON**

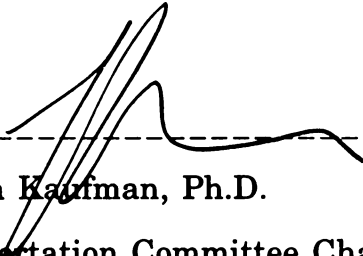
ABSTRACT

Medical imaging techniques are an important tool in the assessment of cardiovascular health. This dissertation investigates the utility of using low field (0.064 Tesla) magnetic resonance imaging techniques to analyze cardiac function. These gated low field cardiac magnetic resonance images are less susceptible, relative to higher magnetic field images, to phase encode artifacts that arise due to inconsistencies in the rate of acquisition of successive phase encoded magnetic resonance signals. Low field magnetic resonance imaging devices are also advantageous as they have significantly lower manufacturing and operating costs compared to higher field imagers. The image signal to noise ratio of low field magnetic resonance images is lower than that of the higher field magnetic resonance images, but this difference is partially compensated by changes in relaxation parameters and other imaging strategies. Additional compensation, without degrading the cardiac functional analysis, is accomplished by the application of a temporal filter that is presented in this dissertation.

Cardiac functional analysis includes measuring: ventricular chamber volumes, myocardial mass, myocardial wall thickening, and

myocardial wall motion. Multi-slice magnetic resonance images allow for the measurement of these parameters in a complete fashion.

Approximation methods for measuring these parameters can also be utilized if the cardiac images are oriented along the long and short axes of the heart. A technique for retrospectively reorienting multi-slice magnetic resonance images along these axes is presented in this dissertation. Using these techniques, cardiac functional parameters were measured from low field magnetic resonance images in a small study (n=12) of normal volunteers. The results obtained were then evaluated and compared to standard measured echocardiographic parameters obtained from these volunteers. The uncertainties in the low field magnetic resonance functional parameters were found to be consistent in magnitude with those found in the echocardiographic measurements. The magnitudes of these uncertainties are also within the normal population variation of these parameters. It is therefore possible to successfully utilize low field cardiac cine magnetic resonance images to make clinically relevant assessments of the functional parameters of the heart.



Leon Kaufman, Ph.D.
Dissertation Committee Chairman

TABLE OF CONTENTS

CHAPTER 1	INTRODUCTION.....	1
CHAPTER 2	CARDIAC ANALYSIS USING MEDICAL IMAGING MODALITIES	6
2.1	INTRODUCTION.....	6
2.2	THE ANATOMY OF THE HEART.....	7
2.3	THE CARDIAC FUNCTIONAL CYCLE	16
2.4	OVERVIEW OF CARDIAC MEDICAL IMAGING.....	21
2.5	ASSESSING CARDIAC FUNCTION FROM NON-INVASIVE MEDICAL IMAGES	29
CHAPTER 3	CARDIAC MAGNETIC RESONANCE IMAGING.....	46
3.1	INTRODUCTION TO MAGNETIC RESONANCE.....	46
3.2	MAGNETIC RESONANCE IMAGING TECHNIQUES	56
3.3	SPECIAL ISSUES RELEVANT TO CARDIAC MAGNETIC RESONANCE IMAGING.....	67
CHAPTER 4	FOURIER TEMPORAL PROCESSING TECHNIQUES FOR IMPROVING SIGNAL TO NOISE IN CARDIAC MR IMAGES.....	74
4.1	INTRODUCTION.....	74
4.2	CHARACTERISTICS OF GATED CARDIAC IMAGES	76
4.3	NOISE MEASUREMENT IN CARDIAC MAGNETIC RESONANCE IMAGES.....	89
4.4	PRACTICAL APPLICATION OF THE TEMPORAL FILTERING ALGORITHM	96

CHAPTER 5	OBLIQUE REFORMATTING OF CARDIAC MAGNETIC RESONANCE IMAGES.....	103
5.1	INTRODUCTION.....	103
5.2	THE METHOD OF RETROSPECTIVE OBLIQUE REFORMATTING OF TOMOGRAPHIC IMAGES ...	106
5.3	EXAMPLES OF RETROSPECTIVELY REFORMATTED OBLIQUE CARDIAC IMAGES.....	116
CHAPTER 6	FUNCTIONAL ANALYSIS OF THE LEFT VENTRICULAR CHAMBER VOLUME	121
6.1	INTRODUCTION.....	121
6.2	MAGNETIC RESONANCE CARDIAC FUNCTIONAL PARAMETER UNCERTAINTIES	125
6.2.1	CARDIAC FUNCTIONAL PARAMETER MEASUREMENT.....	125
6.2.2	TYPES OF PARAMETER UNCERTAINTIES.....	129
6.2.3	SYSTEMATIC CALIBRATION UNCERTAINTIES	133
6.2.4	SYSTEMATIC BOUNDARY UNCERTAINTIES	134
6.2.5	SYSTEMATIC FORESHORTINING UNCERTAINTIES	137
6.2.6	SYSTEMATIC APPROXIMATION UNCERTAINTIES	138
6.2.7	SYSTEMATIC SYSTOLIC BLOOD UNCERTAINTIES	143
6.2.8	SYSTEMATIC ATRIAL KICK UNCERTAINTIES	145
6.2.9	RANDOM PARTIAL VOLUME UNCERTAINTIES	147
6.2.10	CONCLUSION	151
6.3	LEFT VENTRICULAR CHAMBER LENGTH MEASUREMENTS	155
6.4	END DIASTOLIC LEFT VENTRICULAR CHAMBER VOLUME MEASUREMENTS	158

6.5	END SYSTOLIC LEFT VENTRICULAR CHAMBER VOLUME MEASUREMENTS	164
6.6	LEFT VENTRICULAR EJECTION FRACTION MEASUREMENTS	169
6.7	CONCLUSION.....	173
CHAPTER 7	MEASUREMENT OF THE LEFT VENTRICULAR MYOCARDIAL MASS.....	174
CHAPTER 8	ANALYSIS OF THE LEFT VENTRICULAR MYOCARDIAL WALL THICKENING AND MOTION.....	179
CHAPTER 9	CONCLUSION.....	188
BIBLIOGRAPHY	191
APPENDIX	196

LIST OF FIGURES

Figure 2.1	Anterior view of the heart in the mediastinum.....	7
Figure 2.2	Cross section view of the left ventricular myocardium.....	9
Figure 2.3	Cross section of all four cardiac chambers.....	10
Figure 2.4	Sagittal view of the mediastinum showing the forward tilt of the heart.	14
Figure 2.5	The normal electrocardiogram.	16
Figure 2.6	Shaded slices represent planes parallel to the respective cardiac long and short axes.	30
Figure 2.7	Single plane area length method for approximating the left ventricular volume.	35
Figure 2.8	The biplane method of discs method for approximating the left ventricular volume.	36
Figure 2.9	Left ventricular myocardial mass approximation method.....	39
Figure 3.1	Diagram of a Toshiba America MRI Access Imager.....	56
Figure 3.2	An example of a timing diagram for a spin echo MR image acquisition.....	59
Figure 3.3	Example of MR signal.....	60
Figure 3.4	Illustrations of MR spatial encoding methods.....	62
Figure 3.5	Illustration of the acquisition sequence of a cine MR cardiac protocol.....	65
Figure 4.1	Set of cardiac MR images acquired on a Toshiba ACCESS imaging system.	81
Figure 4.2	Calculated magnitude Fourier coefficient images of the Figure 4.1 images.	82
Figure 4.3	Measured coefficient intensity values.....	84
Figure 4.4	Magnitude plot of the Fourier coefficients from a static phantom imaged with a cardiac protocol.	85
Figure 4.5	Graphic representation of the temporal filtering process.....	88

Figure 4.6	The theoretical temporal filter R_{SNR} without any structure noise.....	96
Figure 4.7	The theoretical temporal filter R_{SNR} including estimated structure noise.....	99
Figure 4.8	Temporally filtered cardiac images.	100
Figure 4.9	Average R_{SNR} for filtered images in Figure 4.8.	101
Figure 5.1	Original and oblique coordinate axes reference frames.	107
Figure 5.2	Direction cosines for the oblique coordinate axes	107
Figure 5.3	Example of a three dimensional oblique slice display.	112
Figure 5.4	Simplified direction cosine definition based upon tilt and rotation angles.	114
Figure 5.5	Retrospective oblique reformatting of transaxial cardiac MR images.....	118
Figure 5.6	Retrospective oblique reformatting of coronal cardiac MR images.	119
Figure 6.1	Examples of LV volumetric and linear dimension MR functional parameter components.....	126
Figure 6.2	Short axis ventricular cross sections with inner endocardial and outer epicardial boundaries.....	140
Figure 6.3	Intersection of a sequence of long axis images with the short axis cross-section.....	150
Figure 6.4	A comparison of the measured LV diastolic chamber lengths.	155
Figure 6.5	A comparison of the measured LV systolic chamber lengths.	156
Figure 6.6	Comparison of end diastolic volumes: MR biplane and echocardiographic biplane methods.	159
Figure 6.7	Comparison of MR end diastolic volumes: long axis summed multi-slice and biplane methods.	159
Figure 6.8	Comparison of MR end diastolic volumes: short axis summed multi-slice and biplane methods.	160
Figure 6.9	Comparison of MR end diastolic volumes: short and long axes summed multi-slice methods.....	160

Figure 6.10	Comparison of MR end diastolic volumes: long axis summed multi-slice and area length methods.	161
Figure 6.11	Comparison of MR end diastolic volumes: short axis summed multi-slice and area length methods.	161
Figure 6.12	Comparison of end systolic volumes: MR biplane and echocardiographic biplane methods.	164
Figure 6.13	Comparison of MR end systolic volumes: long axis summed multi-slice and biplane methods.	165
Figure 6.14	Comparison of MR end systolic volumes: short axis summed multi-slice and biplane methods.	165
Figure 6.15	Comparison of MR end systolic volumes: short and long axes summed multi-slice methods.	166
Figure 6.16	Comparison of MR end systolic volumes: long axis summed multi-slice and area length methods.	166
Figure 6.17	Comparison of MR end systolic volumes: short axis summed multi-slice and area length methods.	167
Figure 6.18	Comparison of ejection fractions: MR biplane and echocardiographic biplane methods.	169
Figure 6.19	Comparison of MR ejection fractions: long axis summed multi-slice and biplane methods.	170
Figure 6.20	Comparison of MR ejection fractions: short axis summed multi-slice and biplane methods.	170
Figure 6.21	Comparison of MR ejection fractions: short and long axes summed multi-slice methods.	171
Figure 6.22	Comparison of MR ejection fractions: long axis summed multi-slice and area length methods.	171
Figure 6.23	Comparison of MR ejection fractions: short axis summed multi-slice and area length methods.	172
Figure 7.1	Comparison of myocardial mass: MR truncated ellipsoid and echocardiographic truncated ellipsoid methods.	175

Figure 7.2	Comparison of myocardial mass: MR area length and echocardiographic truncated ellipsoid methods.	175
Figure 7.3	Comparison of MR myocardial mass: long axis summed multi-slice and truncated ellipsoid methods.	176
Figure 7.4	Comparison of MR myocardial mass: short axis summed multi-slice and truncated ellipsoid method.....	176
Figure 7.5	Comparison of MR myocardial mass: long and short axes summed multi-slice methods.....	177
Figure 8.1	Abbreviated single slice short axis cardiac cine.....	183
Figure 8.2	Wall thickness measurement on Figure 8.1.....	184
Figure 8.3	Endocardial radial distance measurement on Figure 8.1.....	185
Figure 8.4	Myocardial wall thickness and radial distance.	186
Figure 8.5	Myocardial wall thickening and wall motion.....	187

LIST OF TABLES

Table 2.1	Typical myocardial wall thickness.....	11
Table 2.2	Analysis criteria for cardiac images.....	21
Table 2.3	Differentiation of cardiac imaging modalities.....	24
Table 2.4	Volumetric functional analysis measurements.....	32
Table 2.5	Normal left ventricular end diastolic volumes.....	37
Table 2.6	Normal left ventricular mass.....	40
Table 3.1	Steady state magnetization and static magnetic field.....	69
Table 4.1	Theoretical R_{SNR} from Equation 4.9.....	98
Table 6.1	Summary of abbreviations used to identify measurement uncertainties.....	130
Table 6.2	Summary of ventricular chamber length uncertainties.....	130
Table 6.3	Summary of ventricular chamber functional parameter uncertainties.....	131
Table 6.4	Summary of myocardial mass functional parameter uncertainties.....	132
Table 6.5	Summary of contractility functional parameter uncertainties.....	132
Table 6.6	Typical linear dimension partial volume uncertainties.....	148
Table 6.7	Summed multi-slice parameter slice axis partial volume uncertainties.....	149
Table 6.8	Average value and variation of the measured cardiac functional parameters.....	153
Table 6.9	Summary of combined systematic and random uncertainties.....	153
Table A.1	Measured magnetic resonance and echocardiographic cardiac functional parameters.....	196

CHAPTER 1

INTRODUCTION

During this century a revolution in medical science has occurred in the form of diagnostic medical imaging. The creation and advancement of medical imaging modalities have been driven by an enormous growth in the evolution of electronic technology which has allowed for the effective utilization of well known physical phenomena. The beginning of the medical imaging revolution occurred just before the turn of the century when Wilhelm Roentgen discovered the capability of x rays to produce, in vivo, true representations of the internal human bones. Further scientific advances in physics during the first half of this century laid the foundation necessary for the medical imaging techniques of nuclear isotope imaging, ultrasound imaging, and magnetic resonance imaging. These advances include: the ability to produce and utilize radioactive substances, the understanding of the properties of high frequency sound waves, and the characterization of the magnetic properties of the atomic nucleus.

Advances in transistor technology, digital computer technology, and detector technology, which began to rapidly occur during the last half of this century, allowed for the construction of medical images utilizing the aforementioned physical properties. Specifically, the advances in digital computer technology have been especially felt in the field of medical imaging. The mathematical processing capabilities of the digital computer are indispensable in the production of magnetic resonance images as well as the images produced from x-ray CT imaging, ultrasound imaging, and

persons suffer from systemic hypertension [1]. Unfortunately cardiovascular disease results in an extremely high number of deaths annually. For example, 968,000 persons died of cardiovascular disease within the United States during the year of 1986 [1]. This number represented 46 percent of all deaths for that year. Current treatment of cardiovascular disease relies on early detection of the disease process. When medical treatment for cardiovascular disease is applied early it is possible that long term physical damage to the heart may be avoided or reduced, limiting the course of the disease and extending the patients life [1]. It is interesting to note that, for reasons that are not well understood, the number of deaths and the degree of affliction of persons in the United States from cardiovascular disease has fallen since 1972 and continues to decline [1].

Medical imaging modalities currently play an enormous role in the investigation, diagnosis, and treatment of cardiovascular disease. X-ray angiography, x-ray ventriculography, nuclear isotope imaging and ultrasound (echocardiography) imaging of the heart are currently utilized throughout the world in the modern practice of cardiology. The motivation for cardiac imaging is to aid in the assessment of cardiac health and function in living human beings. Cardiac imaging is concerned with producing both anatomical information as well as information about cardiac functional performance. While the former goal is important in accessing congenital cardiac defects and anomalies resulting from insult and morbidity, the later is a physiologic assessment useful in assessing cardiomyopathies and ischemic damage to the heart. It is possible to generate cardiac images using magnetic resonance imaging. Though not

currently utilized in the general practice of cardiology, magnetic resonance imaging has been utilized by researchers in various laboratories to expand and improve the current standard of cardiac diagnosis [2-4].

The research project described in this dissertation sought to further explore aspects of cardiac magnetic resonance imaging. The purposes of this work have been to expand the field of cardiac magnetic resonance imaging to include low field (0.064 Tesla) imaging systems, to seek out image enhancements specific to cardiac magnetic resonance images, to expand the presentation of the cardiac magnetic resonance images through retrospective reorientation of the image planes, and finally to make a comparison of quantitative data recorded from cardiac magnetic resonance images to similar data recorded using echocardiography. Specifically, a study of healthy volunteers was undertaken in which corresponding cardiac images were acquired from a low field magnetic resonance imaging system and from an echocardiographic system. Techniques for improving the image signal to noise ratios of cardiac magnetic resonance images were explored utilizing temporal filtering techniques. In addition, the utility of retrospective reorientation of the acquired magnetic resonance images is explored as a method for facilitating the use of approximated functional parameter measurements of the heart. These techniques are applied to the acquired cardiac MR images and the cardiac functional parameters are then measured using a variety of methods. A comparison is then made between the functional cardiac measurements recorded from the two imaging modalities.

CHAPTER 2

CARDIAC ANALYSIS USING MEDICAL IMAGING MODALITIES

2.1 INTRODUCTION

In the modern clinical setting a patient's heart is examined by a physician in order to screen for potential diseases or in the assessment of an occurring disease. Listening to heart sounds, measuring blood pressure, interpreting a patient's history, and analyzing the electrical activity of the heart are all common non-invasive assessment techniques which yield a large amount of useful information about the state of the heart. In cases where cardiac disease is evident it is common to further examine the heart using cardiac imaging techniques. The current array of cardiac imaging modalities, listed in Chapter 1, differ in many important ways including invasiveness, specificity to certain cardiac structures, length of acquisition time, image quality, and expense. In order to fully utilize the information available in a cardiac image it is required to have an understanding of the anatomy of the heart, the functional characteristics of the heart, the effects of common cardiovascular diseases, and the characteristics of the different imaging modalities utilized in the study of the heart. As a result of acquisition limitations, which occur in several imaging modalities, techniques have been developed for estimating cardiac functional performance from a minimal set of cardiac images. In the following sections these topics will be briefly presented.

2.2 THE ANATOMY OF THE HEART

The heart is a muscular organ responsible for circulating the blood throughout the human body and hence transporting material necessary for life. The heart is surrounded by the fibroserous pericardial sac and is located in the middle mediastinum between the two lung containing

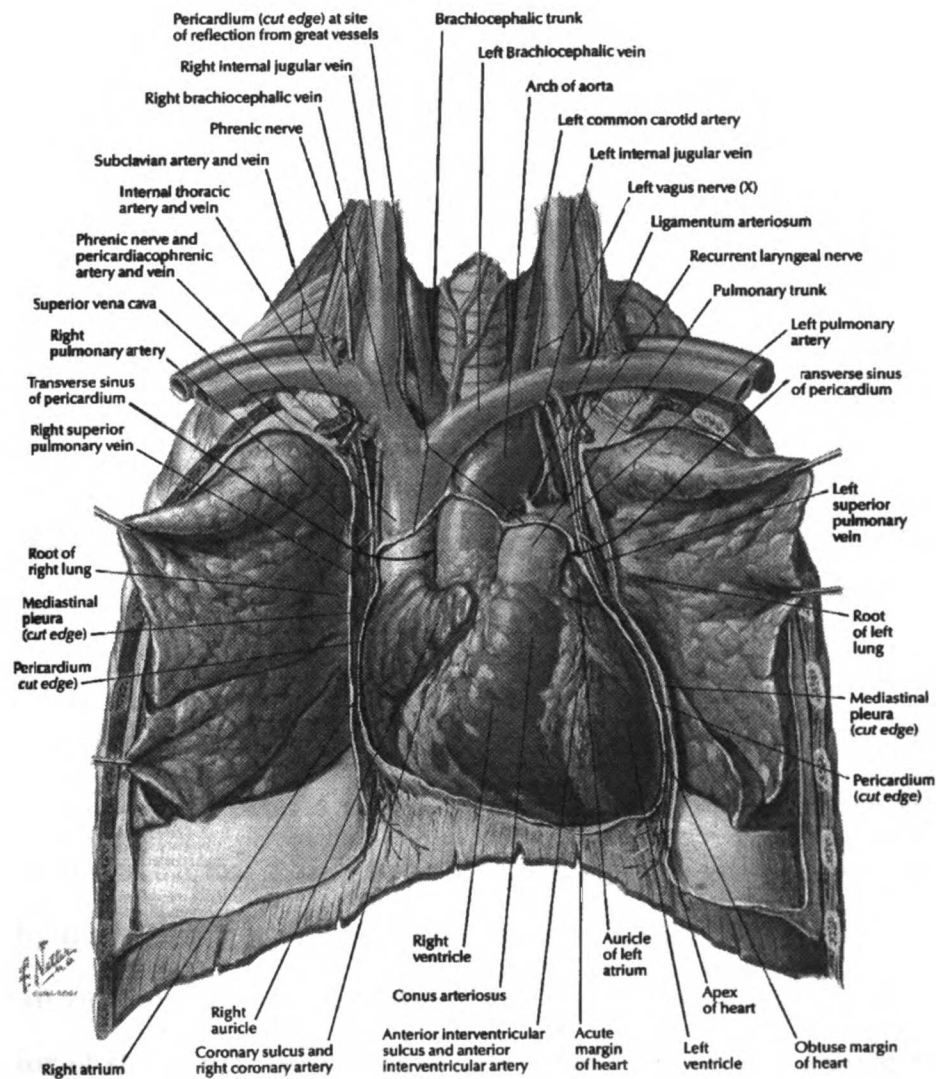


Figure 2.1 Anterior view of the heart in the mediastinum. Note the leftward tilt of the cardiac apex.

© Copyright 1989 CIBA-GEIGY Corporation. Reprinted with permission from the ATLAS OF HUMAN ANATOMY, illustrated by Frank H. Netter, M.D. All rights reserved.

pleural sacs. The most superior portion of the heart is referred to as the base while the most inferior portion, at the bottom of the ventricular chambers, is referred to as the apex. The position of the heart is variable from individual to individual and during normal respiration and cardiac contraction. It is common though to find that approximately two-thirds of the heart's mass is located to the left of the midline and that the apex of the heart is directed inferioventrally (down and towards the patient's front) and laterally to the patient's left (Figure 2.1 and Figure 2.4) [1]. The inferior border of the heart is adjacent to the diaphragm where the diaphragm and the pericardium are connected together at the diaphragm's central tendon. At the base of the heart the pulmonary artery and the aorta emerge, while at the upper right margin of the heart the superior vena cava enters and at the inferior right margin of the heart the inferior vena cava enters. Finally the four pulmonary veins enter the heart posteriorly just below the base. The pericardium extends around the heart and surrounds the roots of these vessels connecting them with the pericardial sac.

Internally the heart is divided into four chambers. The chamber walls are composed of interlacing bundles of cardiac muscle fiber known as the myocardium (Figure 2.2). The outflow orifice of each chamber is guarded by leaflets of tissue which act as valves, closing off the output of the chamber in response to pressure generated by reverse blood flow. Lining the interior of the heart, including the myocardium and the valves, is a layer of endothelial tissue and connective tissue called the endocardium. The exterior of the heart is covered by a layer of mesothelium tissue and connective tissue known as the epicardium. The epicardium is also known

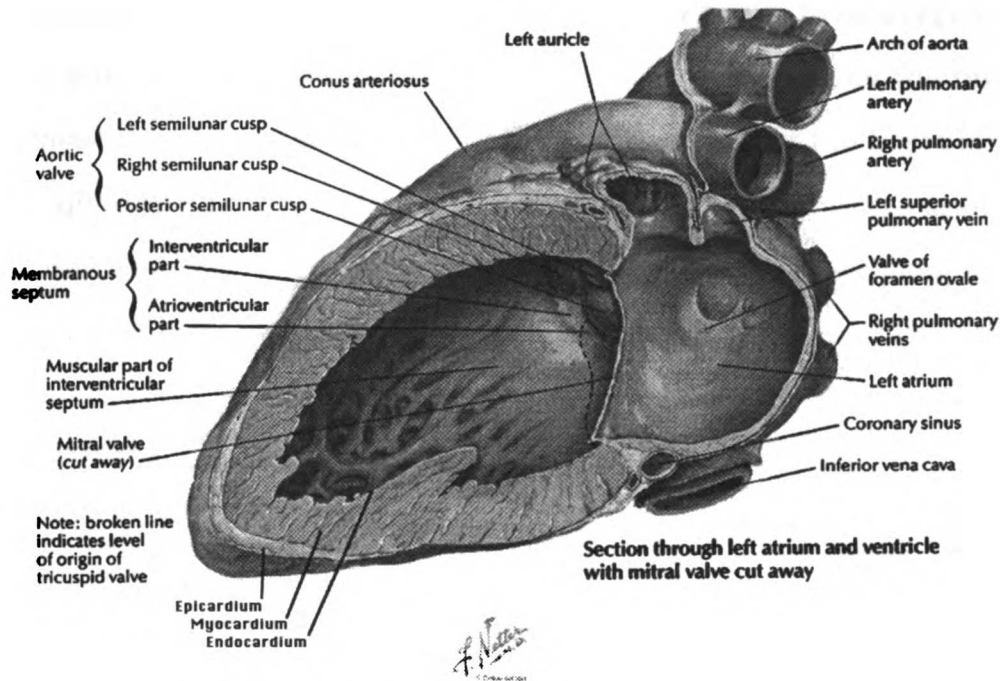


Figure 2.2 Cross section view of the left ventricular myocardium.

© Copyright 1989 CIBA-GEIGY Corporation. Reprinted with permission from the ATLAS OF HUMAN ANATOMY, illustrated by Frank H. Netter, M.D. All rights reserved.

as the visceral pericardium since this tissue actually makes up the interior wall of the pericardial sac. The outer wall of the pericardium, the parietal pericardium, is also made up from mesothelial tissue and connective tissue and it encloses and faces the visceral pericardium. This tissue secretes a serous fluid providing a lubricated cavity enabling the heart's smooth, frictionless motion as it contracts and relaxes. The pericardial connective tissue is a tough fibrous tissue which provides a strong containing sac, attached at the diaphragm and the cardiac vessels, which supports the heart and maintains the heart's position within the mediastinum.

The four chambers of the heart functionally divide into two pumps (Figure 2.3). The right half which pumps deoxygenated blood gathered from

the body through the pulmonary artery over to the lungs to be oxygenated, and the left half which pumps oxygenated blood received from the lungs throughout the rest of the body via the aorta. Each half of the heart is further divided into a two stage pump made up of two chambers known as the atrium and the ventricle. Viewing the heart along its own long axis, the atria are each located superiorly to their respective ventricles. The two atria

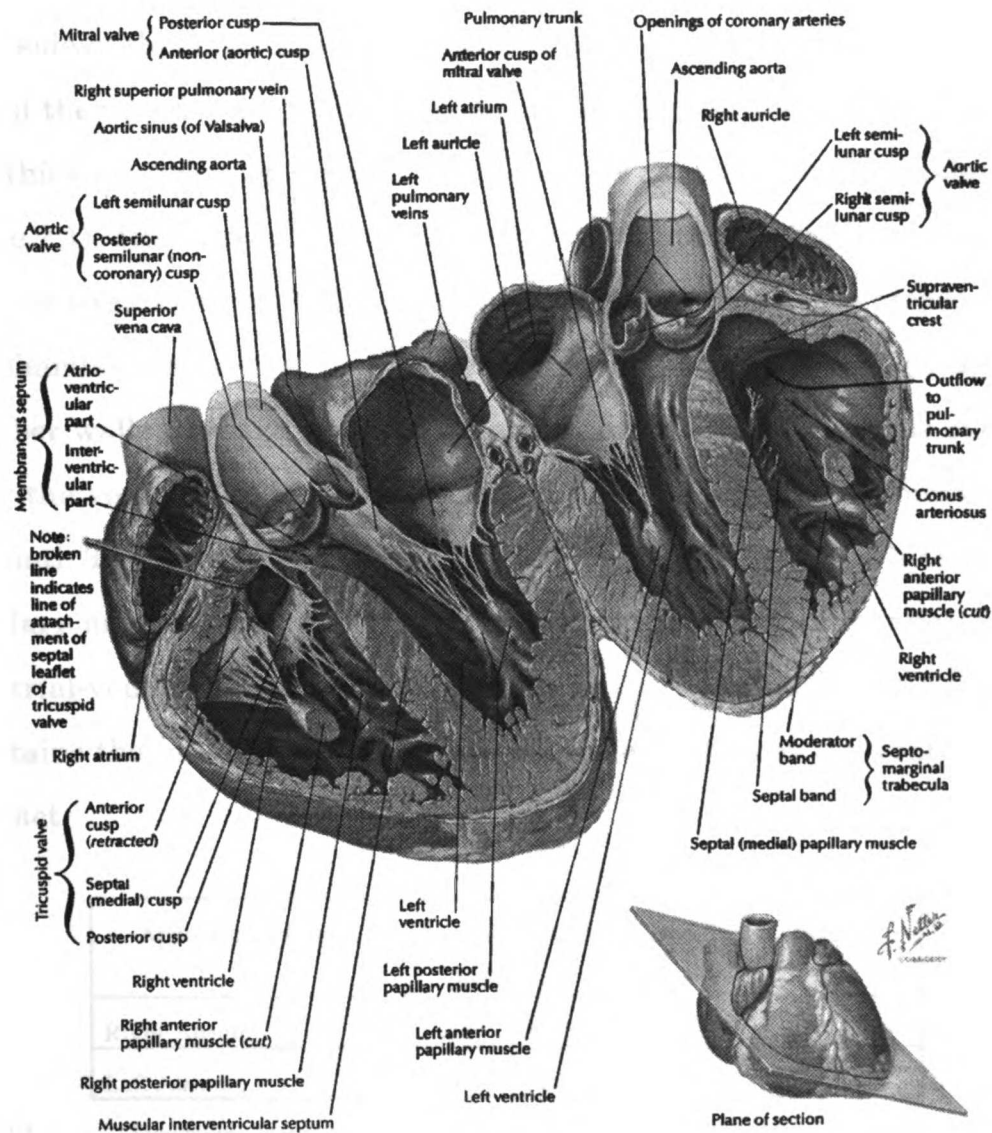


Figure 2.3 Cross section of all four cardiac chambers.

share a common muscular wall, known as the atrial septum, and the two ventricles share a common muscular wall known as the ventricular septum. The right ventricle is shaped similar to a crescent, partially wrapped around the elliptical-cone shaped left ventricle. The thickness of the myocardial chamber walls is normally related to the resistance experienced during contraction. This results in chamber walls of differing thickness as the atria experience less resistance than the ventricles and the right side of the heart experiences less resistance than the left side. In the case of the ventricles a typical healthy individual may have a left ventricle wall thickness between 2 and 3 times as thick as the right ventricular wall (Table 2.1). The thickness of the left ventricular apex is often found to be 2 mm or less, relatively thin compared to the rest of the left ventricle [1]. The chamber walls vary from being very smooth at points such as the inner chamber walls to rough and fibrous along the chamber free walls such as along the ventricular trabeculae carneae or the right atrium's musculi pectinati. The interior of the ventricular chambers is occupied by small papillary muscles, anchored in the myocardium, which are connected to the atrial-ventricular valves through the chordae tendineae. This structure maintains the integrity of the atrial-ventricular valves as the ventricles contract.

Approximate Cardiac Chamber Wall Thickness In A Typical Healthy Individual			
Individual			
Right Atrium	2 mm	Right Ventricle	4- 5 mm
Left Atrium	3 mm	Left Ventricle	8-15 mm

Table 2.1 Typical myocardial wall thickness. This table is constructed from reference [1], pp. 19-20. It is representative of wall thickness from autopsied hearts and is only a rough average of typical wall thicknesses. It is expected that variation will occur from individual to individual.

The heart wall is supplied with oxygenated blood through the two coronary arteries which traverse the epicardium before branching and entering the myocardium. The right and left coronary arteries are the first branches off of the aorta emerging respectively from the aortic sinuses associated with the anterior and left posterior aortic valve cusps located at the root of the aorta. The right and left coronary arteries straddle the anteriorly located pulmonary artery one on each side. The right coronary artery then runs in between the right atrium and the right ventricle along the coronary groove. At the inferior border of the heart this artery gives off the marginal branch which extends towards the apex, supplying the inferior border of the heart with oxygenated blood. The right coronary artery then goes on to form the posterior interventricular (sometimes called the posterior descending) branch which supplies the posterior portion of the two ventricles. The left coronary artery passes beside the pulmonary artery and then extends to the coronary groove where it divides into an anterior interventricular (sometimes called the anterior descending) branch and a circumflex branch. The anterior interventricular branch runs along the anterior portion of the heart in between the two ventricles where it supplies them with oxygenated blood. The circumflex branch continues in the coronary groove to the posterior portion of the heart where it supplies the posterior left atrium and the posterior left ventricle with oxygenated blood. Deoxygenated blood returns to the circulatory system from the myocardium through the coronary veins and then into the coronary sinus which runs from left to right in the posterior coronary groove. The coronary sinus conveys the deoxygenated blood to the right atrium. To a lesser degree

11005 11000000

deoxygenated blood also returns through the small Thebesian veins which drain directly into the chambers of the heart.

The cardiac valves act to open and close the cardiac chambers in a fashion that inhibits reverse flow of blood as the heart contracts and hence facilitates blood flowing correctly through the heart. The path that the flow of blood follows begins with the right atrium which acts as a reservoir, receiving blood from the inferior vena cava, the superior vena cava, and the coronary sinus. As the right atrium contracts blood is channeled through the tricuspid valve into the right ventricle. The contraction of the right ventricle follows next propelling blood through the pulmonary valve and into the pulmonary artery towards the lungs where the blood is oxygenated. Oxygenated blood then flows through the four pulmonary veins to be collected in the left atrium. The left atrium contracts synchronously with the right atrium, propelling blood through the mitral valve and into the left ventricle. The left ventricle then contracts, synchronous with the right ventricle, pumping blood through the aortic valve and into the aorta for delivery throughout the body.

Visualizing the orientation of the heart within the body is extremely important when identifying anatomical structures from cardiac images and when registering quantitative measurements from these images. The orientation of the heart is defined by describing the direction of a three dimensional vector directed along the cardiac long axis and the rotation of the heart about this cardiac long axis. The long axis vector of the heart is directed from the base of the heart inferiorly to the apex of the heart through the cardiac center of mass. Empirically the cardiac long axis

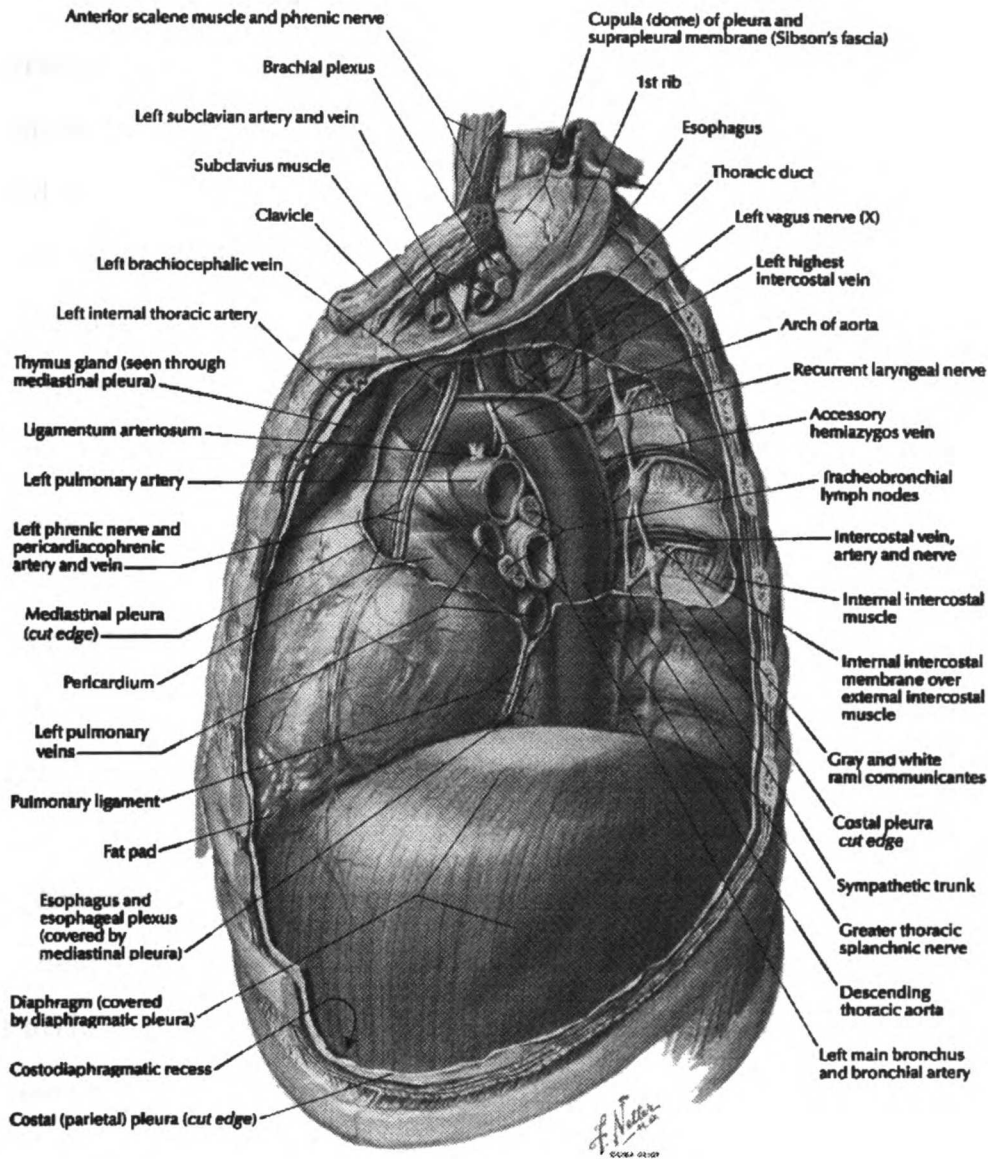


Figure 2.4 Sagittal view of the mediastinum showing the forward tilt of the heart.

© Copyright 1989 CIBA-GEIGY Corporation. Reprinted with permission from the ATLAS OF HUMAN ANATOMY, illustrated by Frank H. Netter, M.D. All rights reserved.

vector can be defined to follow the cardiac interventricular septum. With respect to the patient's body the heart is normally slightly rotated to the patient's left about the cardiac long axis. As a result of this rotation the left and right halves of the heart are not evenly positioned with respect to the

patient's body. The orientation of the heart can usually be classified into one of three categories [6]. The first is the vertical type which is characteristic of persons with long narrow chests. In this case the cardiac long axis is aligned parallel to the body's own long axis which is directed from the most cephalic point along the patient's midline caudally. The second is the transverse type which is found in persons who are stocky, obese, or in pregnant women. In this case the heart has a very large lateral tilt to the left such that the cardiac long axis points almost to the patient's side. The third and most common orientation is the oblique type presented at the beginning of this section. In this orientation the heart is tilted anteriorly and to the left (Figure 2.1 and Figure 2.4). One source estimates the cardiac long axis of the oblique type cardiac orientation to be tilted with respect to the bodies long axis by 45 degrees anteriorly and 60 degrees to the left [8].

Examining the heart in the oblique type orientation, the right margin of the heart (from the patient's perspective) is made up superiorly by the right atrium, and inferiorly by the right ventricle. Due to the leftward tilt of the heart the inferior border is primarily made up of the right ventricle. The apex is made up of the inferior end of the left ventricle. Almost the entire left margin of the heart is made up of the outer wall of the left ventricle. Owing to the rotation of the heart about the cardiac long axis, the bulk of the anterior surface of the heart is formed from the outer wall of the right ventricle. The posterior inferior surface of the heart is formed by the left ventricle, while the posterior superior surface is made up from the left atrium. At the anterior superior surface of the heart the great vessels emerge with the root of the pulmonary artery the most anterior, followed by the aortic root.

2.3 THE CARDIAC FUNCTIONAL CYCLE

The heart carries out its function through a repetitive process of contraction and relaxation referred to as the systolic phase and the diastolic phase respectively. Cardiac contraction is triggered by electrical impulses generated in specialized cardiac muscle tissue known as the sinoatrial node located at the posterior wall of the right atrium. The electrical impulses from this tissue first cause the atria to contract and then trigger the ventricles to contract through the conduction of the sinoatrial pulse to the atrioventricular node located in the posteroinferior portion of the interatrial septum. The atrioventricular signal is conducted throughout the

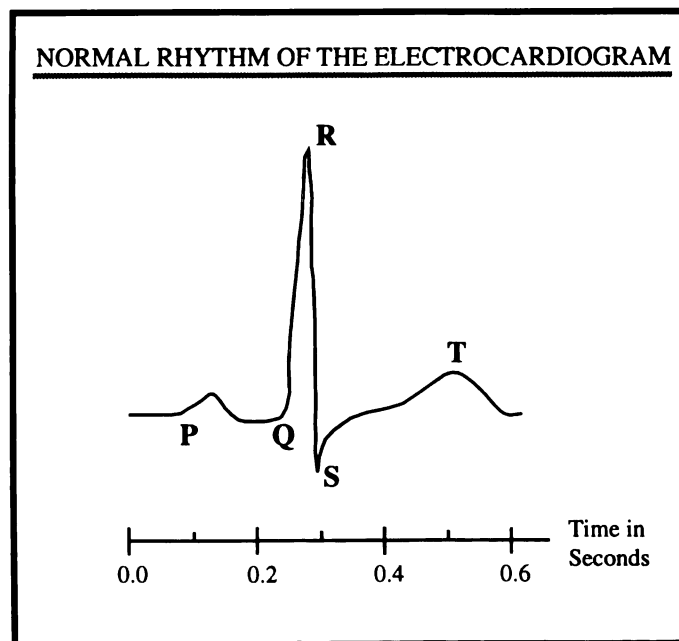


Figure 2.5 The normal electrocardiogram [15].

ventricles by another specialized muscle tissue called the Purkinje fibers. The electrical signal which causes the heart to contract can be externally monitored using skin electrodes attached to an electrocardiogram (ECG) machine [7]. The initial contraction impulse from the sinoatrial node can

JCSF LIBRARY

be seen as the P wave on the ECG. The delayed second pulse, which is significantly larger, indicates the beginning of the ventricular contraction and is known as the QRS wave on the ECG. Note that in a healthy heart the right and left sides of the heart contract synchronously at a rate of roughly 70 beats per minute.

Utilizing the left side of the heart, the cardiac contraction cycle can be divided into several distinct phases starting with the beginning of systole [7]. This phase is known as the isovolumetric phase and it is initiated by the spreading of the atrioventricular electrical impulse through the left ventricle beginning the ventricular contraction which forces closed the mitral valve. During this phase the pressure in the left ventricle increases as the chamber contracts with both the aortic valve and the mitral valve closed. When the chamber pressure matches the aortic pressure the aortic valve opens beginning the next phase, maximum ejection, where blood rushes out of the left ventricle into the aorta. The following phase, reduced ejection, occurs as blood starts flowing more slowly out of the left ventricle. As the volume of blood in the chamber becomes reduced the chamber pressure of the left ventricle decreases. When the left ventricular chamber pressure falls to a level just below the aortic pressure the outflow of blood into the aorta subsides and the aortic valve begins to close. This phase is viewed as the end of the systolic period in the contraction cycle.

The diastolic period of the contraction cycle begins in the protodiastole phase as the systolic period ends. In this phase blood flow out of the left ventricle has stopped and the aortic valve has just about closed. The aortic valve will close in response to a momentary reversal of blood flow

UCSF LIBRARY

responding to the reduced pressure in the left ventricle with respect to the aorta. When the aortic valve closes it begins the second diastolic phase, isovolumetric relaxation. As the chamber relaxes with the valves closed the pressure in the left ventricle reduces. When the ventricular pressure falls below the pressure in the left atrium the mitral valve opens and allows blood to rush into the left ventricle increasing the ventricular volume in the rapid filling phase and then the reduced filling phase. The final phase of the diastolic period occurs with the contraction of the left atrium. This phase causes a significant increase in both the volume of blood in the left ventricle and the stretching of the muscular fibers of the left ventricle in what is known as the atrial kick.

The amount of blood which is pumped out of the heart is controlled by four factors. The first factor is the preload the heart experiences. Preload is an expression of Starling's law of the heart which states: "the energy of contraction is proportional to the initial length of the cardiac muscle fiber" [7]. This implies that the force of cardiac contraction is governed by how much the cardiac muscle fibers have been stretched by the inflow of blood into the cardiac chamber. The longer that the fibers are stretched the more forceful the contraction. The amount of blood that is able to flow into the cardiac chamber produces the stretch of the cardiac muscle fibers and hence regulates the force of the cardiac contraction. Next, the amount of blood which is expelled by the contracting cardiac chamber is inhibited by the afterload the chamber experiences. Afterload is the force that the cardiac chamber must contract against as it squeezes blood out into the circulatory system. The end diastolic volume of the chamber, the impedance of the aorta, the peripheral vascular resistance, and the

viscosity of the blood are a few of the factors which contribute to the afterload force. The contractility of the myocardium is another factor which controls how much blood the heart is able to pump out of a cardiac chamber. Contractility is a measure of the strength and health of the myocardial tissue and is responsible for the degree and speed of the myocardial tissue shortening and hence chamber contraction. Logically the final factor responsible for cardiac output is the rate at which the heart undergoes contraction, known simply as the heart rate.

As the heart undergoes contraction the shape and position of the cardiac chambers vary. It has been reported that ventricular cardiac contraction may be effectively occurring in a two step fashion [8]. The first step proceeds as a radial shortening of the ventricular chamber which results in the initial increase in chamber pressure which lasts approximately 50 msec [8]. The second step in ventricular contraction results in the shortening of the long axis of the ventricular chamber which maintains the outflow of blood against the afterload present in the circulatory system. This step lasts until the ventricle begins to relax in the diastolic cardiac phase [8]. Hence contraction of the left ventricle results in the anterior and posterior chamber walls moving inward in a transverse fashion [9] and then the base of the heart descending towards the apex as the apex remains relatively fixed [8]. As a result of this pattern of contraction the directional axis of the heart, as viewed along the heart's long axis, shifts anteriorly as the heart contracts. In addition to the original rotation of the heart as a whole about the cardiac long axis, described in Section 2.2, the heart also undergoes a further slight rotation about the cardiac long axis as the myocardial muscle fibers contract.

Analysis of myocardial wall motion is used in the assessment of cardiac disease. In ischemic or infarcted myocardial tissue the contractility of the myocardium may become reduced or regionally impaired resulting in a noticeable change in cardiac wall motion. This change may be detected as a relative difference in motion for a myocardial region compared to the surrounding tissue. The motion abnormality may be so substantial that the affected myocardial region may appear to be static during cardiac contraction. Another technique used to analyze the contractility of the myocardium is myocardial thickness analysis. Healthy myocardial tissue increases in thickness as the heart contracts [10]. This is related to the shortening of the cardiac muscles fiber which occurs in healthy myocardial tissue. Diseased myocardium may experience reduced contractility and hence reduced thickening. Abnormalities in myocardial wall motion and myocardial thickness should occur simultaneously as a result of the occurring cardiac pathology. As will be discussed in Section 2.5, the sensitivity of these two techniques though may vary independently as a result of the circumstances of the underlying cardiac disease.

JCSF LIBRARY

2.4 OVERVIEW OF CARDIAC MEDICAL IMAGING

Cardiac images are produced to allow physicians to analyze the anatomic integrity and the functional performance of the heart in the assessment of cardiovascular disease. Table 2.2 lists a set of criteria for evaluating cardiac images. The anatomic structures which must be examined to produce this assessment include the myocardium, the cardiac valves, the coronary arteries, the great vessels, and the interior of the cardiac chambers. Abnormalities in these structures resulting from congenital defects, physical trauma, or cardiovascular disease are all significant in the evaluation of the condition of the heart. A person suffering from cardiovascular disease will often show abnormalities in more than one of the criteria in Table 2.2.

What are the sizes of the cardiac chambers?
What is the state of the chamber myocardium?
What is the state of the cardiac circulatory system?
What are the global and segmental cardiac function?
What is the metabolic state of the cardiac tissue?

Table 2.2 Analysis criteria for cardiac images [11].

The first criteria listed is size of the cardiac chambers. Enlarged cardiac chambers are often found in the disease processes which result in cardiac failure [8]. Cardiac chambers can become enlarged as a result of impaired cardiac valves or systemic hypertension. Quantification of the size of a cardiac chamber can be accomplished by measuring the end diastolic blood volume of the chamber. The second criteria listed in Table 2.2 is concerned with the size or mass of the chamber myocardium. Enlargement

of the myocardium, hypertrophic cardiomyopathy, is one potential myocardial disease state. It can occur as a result of systemic hypertension, due to tissue damage from a myocardial infarction [8] or from other conditions which cause chamber pressure overload [10]. One problem of hypertrophic myocardial tissue is that it places an increased demand upon the circulatory system of the heart and may result in myocardial ischemia. Estimating the extent of hypertrophy can be accomplished by measuring the diastolic volume occupied by the chamber myocardium. Myocardial mass can be calculated from this volume using an accepted standard for myocardial density. Hypertrophic myocardial tissue often enlarges at the expense of the chamber lumen as opposed to increasing the external size of the heart. Hence the estimation of myocardial mass is a more reliable estimate of hypertrophy over basic chest x-ray analysis [10]. The state of the chamber myocardium is also related to the degree of myocardial contractility and the amount of myocardial blood perfusion. The next assessment criteria, the state of the cardiac circulatory system, is concerned with both myocardial tissue perfusion and coronary artery patency. Indirect measurement of myocardial tissue perfusion can be achieved through radioactive isotope imaging techniques. The coronary arteries are of concern because they can become narrowed or obstructed from coronary heart disease which may result in myocardial ischemia. Examination of the coronary arteries can be accomplished using x-ray angiography.

When the myocardium becomes ischemic it may exhibit reduced cardiac function and decreased myocardial metabolism. An assessment of cardiac function includes estimating the amount of blood pumped out of the

UCSF LIBRARY

heart and detecting abnormalities in myocardial contraction. During the early stages of ischemic cardiac disease it may be necessary to place the heart under stress—one method is through aerobic exercise—in order to evoke a potential decrease in cardiac function. Functional analysis produces global and regional information. The total blood volume pumped in one cardiac cycle for example is a global quantity. Regional analysis techniques include relative wall motion and relative wall thickening measurements of the myocardium. These two analysis techniques are used to estimate indirectly the contractility of the myocardium. Certain cardiac imaging techniques can be used to register the metabolic activity of the heart. A measurement of cardiac metabolism can be used to locate necrotic tissue that may have resulted from a myocardial infarction or to help distinguish ischemic regions of the heart.

Cardiac images are produced from standard medical imaging techniques which have been adapted to produce images of the heart. These imaging modalities include: x-ray angiography, x-ray ventriculography, nuclear isotope imaging, echocardiography, magnetic resonance imaging (MRI), cine x-ray computed tomography (CT) imaging, and positron emission tomography (PET) imaging. As a result of characteristic differences in these cardiac imaging modalities the images they produce are not interchangeable. In order to produce a complete analysis of the heart satisfying the criteria listed in Table 2.2 it is common to utilize more than one of the listed imaging modalities. The differences in these imaging modalities can be categorized as shown in Table 2.3.

JCSF LIBRARY

	X-RAY ANGIO.	X-RAY VENTRIC.	CINE CT	ECHO	MRI	NUCLEAR. MEDICINE	PET
TOMOGRAPHIC			√	√	√	√	√
FUNCTIONAL ANALYSIS		√	√	√	√	√	
PERFUSION ANALYSIS	√				√	√	√
METABOLIC ANALYSIS					√		√
IONIZING RADIATION	√	√	√			√	√
CONTRAST AGENT	√	√	√		√	√	√
REAL-TIME ACQUISITION	√	√		√	√		
EXERCISE TESTING			√	√	√	√	√
PORTABILITY				√		√	

Table 2.3 Differentiation of cardiac imaging modalities.

Cardiac tomographic imaging modalities, introduced in Chapter 1, produce cross sectional images of finite thickness which slice through the heart. Magnetic resonance imaging is one of the most flexible tomographic modalities allowing for the acquisition of multiple slices oriented along almost any directional axis. Two-dimensional echocardiography is not as flexible as it is limited in the orientations from which slices can be acquired. This limitation is due to the physical constraints of viable acquisition windows into the patient's body and due to the physical constraints of the acquisition probe.

Standard x-ray imaging modalities, in contrast to tomographic imaging modalities, produce projection images where the entire three dimensional volume is represented in a two-dimensional image. Projection images of the coronary arteries produced using x-ray angiography are better suited for tracing the path of the coronary arteries and for identifying coronary occlusions. The coronary arteries twist and curve around the

heart in different directions over a rather large volume. Hence a projection image can be used to display the entire path of the coronary arteries in one image frame. A tomographic view of the coronary arteries would require many slices to fully present the path of the coronary arteries. The directional changes of the coronary arteries also pose a problem for tomographic imaging techniques complicating the selection of the correct orientation for the image plane. As a result of these difficulties, identifying and tracing the coronary arteries in tomographic slices is not as straight forward as in the x-ray projection images. On the other hand tomographic images are better suited for displaying the chamber cavity including the myocardium. Here every segment of the cavity can be displayed separately instead of all at once. As will be seen later this allows for measurements of chamber volume and myocardial motion which are more specific and do not require approximation techniques.

Functional analysis of the heart is performed using imaging modalities where the myocardium can be distinguished from the chamber blood pool and from the epicardial boundary. This may occur as a result of the imaging process or require the injection of a contrast agent. It is also necessary that images are generated for the different phases of the cardiac cycle from the beginning diastolic phases to the end systolic phases. The acquired images are usually displayed one after another in a cine format in order to give the appearance of the heart actually contracting. Cardiac imaging modalities which produce images of the heart over all of the cardiac phases in a single cardiac cycle are known as real-time imaging modalities. Imaging techniques that require more time than a single cardiac cycle to acquire the cardiac images use a technique called cardiac

UCSF LIBRARY

gating. In this method the temporal acquisition points are synchronized to the cardiac cycle using the ECG signal. The synchronization is performed by using the Q-R interval of the ECG as the beginning of a timed sequence of image acquisitions which are then repeated until the image data is complete. Cardiac gating techniques tend to work well because the heart beats in a periodic fashion where at a given temporal point in the cardiac cycle the heart is essentially in the same physical position cycle after cycle. Three circumstances that can disturb the desired periodic position of the heart as it contracts are: patient movement, respiratory motion of the heart, and a variable heart rate. There are researchers that have reported developing real-time MRI techniques but commercially these machines are still very rare.

The invasiveness of an imaging modality can often be a very important issue in the utilization of the modality. One of the motivations for imaging the heart is to track the course of a patient's cardiovascular disease as a treatment is administered. Hence it may be required that a patient be imaged on a regular basis. In addition, cardiac patients are often very ill and do not tolerate invasive procedures easily. Both of these situations make it undesirable to subject a patient to repeated invasive imaging procedures where ionizing radiation is used or that require the injection or infusion of a contrast agent. Echocardiography and magnetic resonance imaging are both non-invasive imaging modalities and are excellent choices for the long term analysis of cardiac disease in a patient. Currently, MRI contrast agents are increasingly being utilized although they were not used to produce any of the cardiac MR images presented in this dissertation.

UCSF LIBRARY

Exercise testing, as introduced previously, can evoke symptoms of early cardiovascular disease and hence has great importance in cardiac imaging. Not all imaging modalities can be used to acquire images as a patient exercises. Invasive contrast imaging modalities where a catheter is introduced into the heart make the further stress of the heart with exercise undesirable. Another impediment to exercise testing is the duration of an acquisition procedure. Cardiac imaging protocols can be selected to reduce the acquisition time although often in exchange for reduced image quality. The physical structure of a medical imaging device can also be an impediment, making exercise while the patient is imaged impractical.

The utilization cost of a cardiac imaging modality is becoming an important issue in the modern day clinical setting. Less expensive imaging modalities such as echocardiography are more likely to be used in the modern clinical environment than the more expensive modalities such as MRI and cine x-ray CT imaging. Another important utilization concern is the portability of the imaging modality. A mobile modality such as echocardiography and nuclear isotope imaging, which can be wheeled to a patient's bedside, is more likely to be used than a permanently situated imaging modality. The quality of the cardiac images produced by the imaging modality is an additional utilization issue. High quality cardiac images should offer good contrast between the chamber blood pool, the myocardium, and the epicardium. In plane pixel resolution is required to be fine enough to visualize internal cardiac structures such as the papillary muscles and the position of the cardiac valves. Finally the slice thickness

UCSF LIBRARY

should be appropriate to identify the extent of the cardiac chambers without causing excessive partial volume effects.

UCSF LIBRARY

2.5 ASSESSING CARDIAC FUNCTION FROM NON-INVASIVE MEDICAL IMAGES

Common cardiac functional performance measurements can be differentiated into three groups: volumetric measurements, myocardial contraction measurements, and pressure measurements of the cardiac chamber and arteries. The first two functional parameters of this list can be measured using non-invasive cardiac imaging techniques. Measuring in vivo pressure parameters though requires the use of an invasive catheter with an integrated pressure transducer. The cardiac functional analysis methods presented in this section will be restricted only to non-invasive functional measurement techniques. While the effects of cardiovascular disease can be present in any of the four cardiac chambers the functional performance of the heart is usually measured by examining the state of the left ventricle. The motivation for selecting left ventricular function is due to the left ventricle's large role in systemic circulation and the fact that cardiovascular diseases often manifest changes in left ventricular function [1]. Cardiac functional analysis techniques can either be qualitative or quantitative evaluations. The qualitative methods produce results through the application of subjective methods of observation. Quantitative techniques strive to produce an objective numeric or graphic result directly related to the state of the heart. The later of these two evaluative methods will be the primary focus of this and later discussion.

Two imaging modalities which non-invasively produce an assessment of left ventricular function are magnetic resonance imaging and two-dimensional echocardiography. Although it is possible to acquire functional information using M-mode echocardiography the

JCSF LIBRARY

echocardiographic techniques presented here utilize two-dimensional imaging only. Cardiac images from which the functional analysis is performed are acquired along both the long axis and the short axis of the left ventricle (Figure 2.6). The long axis orientation, referred to as an apical view, produces images oriented through the apex of the heart towards the cardiac valves. A two-chamber (sagittal) apical view shows only the left ventricle and the left atrium while a four-chamber (coronal) apical view includes portions of each of the left and the right cardiac chambers. Short axis (transaxial) views are oriented perpendicular to both of the apical orientations. When the apical views of the left ventricle are properly oriented an image slice through the center of the chamber should present the maximal ventricular chamber area. In contrast, when the short axis view is properly oriented, an image slice through the chamber center should present a minimal chamber area.

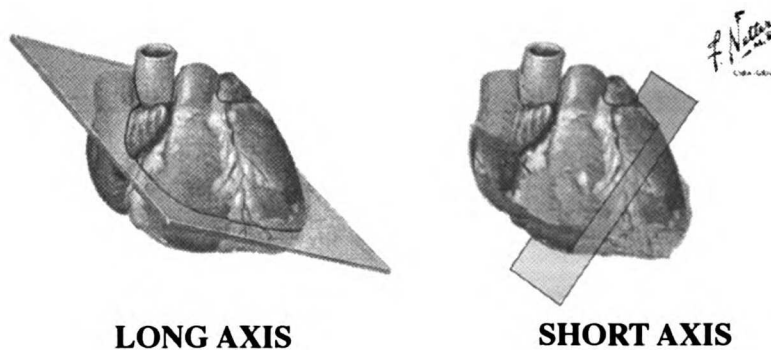


Figure 2.6 Shaded slices represent planes parallel to the respective cardiac long and short axes.

© Copyright 1989 CIBA-GEIGY Corporation. Reprinted with permission from the ATLAS OF HUMAN ANATOMY, illustrated by Frank H. Netter, M.D. All rights reserved.

Quantitative cardiac functional parameters are measured from cardiac images using an interactive computer system. Typically an image

is displayed on a computer video screen and a screen pointing device is used to define some combination of the endocardial border, the epicardial border, or a specific chamber linear dimension. The computer then translates these measurements into an actual quantitative value based upon the voxel dimensions of the image. Volumetric measurements of the blood in the left ventricle are defined by the endocardial border of the myocardium. Myocardial mass and myocardial contraction measurements are defined by both the endocardial and the epicardial borders of the myocardium. The convention for defining the endocardial border is to outline the interface between the ventricular blood pool and the myocardium. Internal structures, such as the papillary muscles, are defined to be a part of the blood volume and hence they are ignored [12]. The chamber volume is closed by drawing a line along the path of the closed valve leaflets. When the valve leaflets are not visible a straight line joining the roots of the valve leaflets is drawn. The epicardial boundary is defined along the outer margin of the myocardium. At the ventricular septum the left ventricular epicardial boundary is actually the endocardial boundary of the right ventricle. Finally, care must be taken to standardize the setting of the image window (pixel intensity lookup table) parameters. These guidelines are adhered to in order to achieve a consistent method of defining boundaries on the heart images.

Cardiac volumetric measurements are categorized into static measurements or dynamic measurements [5]. Static measurements are those measurements which represent the state of the heart at a specific moment in time. Dynamic measurements represent the state of the heart at more than one moment in time, usually through a comparison of two or

JCSF LIBRARY

more static measurements. The blood volume of the left ventricle at the end of the diastolic period for example, known as the end diastolic volume (EDV), is a static measurement. Subtracting the end systolic volume (ESV), another left ventricular static measurement, from the EDV yields the stroke volume (SV). Stroke volume is a dynamic measurement which indicates the volume of blood that is pumped by the left ventricle in a single contraction cycle. Another common dynamic measurement is the ejection fraction (EF), a measure of the amount of blood pumped out of the left ventricle in relation to the amount of blood contained in the left ventricle before contraction begins. Actual formulas for these two measurements can be found below, in Table 2.4.

STROKE VOLUME	EJECTION FRACTION
$SV = EDV - ESV$	$EF = \frac{EDV - ESV}{EDV}$

Table 2.4 Volumetric functional analysis measurements [5].

The cardiac EF is used by cardiologists as a quick assessment of the effectiveness of a patient's cardiac contraction cycle. The measured EF parameter can be correlated to the eventual outcome in many cardiac disease situations. An example would be the case of a patient who has just experienced a myocardial infarction where the EF provides some insight towards the short term survivability of this individual [10]. It should be noted that the EF is not a good indicator for the degree of contractility of the myocardial tissue. The reason for this is that the EF is very dependent upon the preload and the afterload experienced in the cardiac chamber [10].

Determining the EDV and the ESV first relies upon selecting cardiac images at the correct end diastolic and end systolic temporal points in the cardiac cycle. The end diastolic point occurs just before the left ventricle begins to contract. Ideally the end diastolic frame is chosen to occur at the temporal point where the mitral valve closes in response to the beginning of left ventricular contraction [12]. A simultaneously recorded ECG signal can also be used to select the end diastolic temporal point at the image frame where the QRS complex is first evident [12]. If there are difficulties in using these techniques to determine the end diastolic time point then the contraction cycle frame with the largest left ventricular area can also be used to select the end diastolic temporal point. The end systolic temporal point is usually selected from the temporal image frame just prior to the opening of the mitral valve which occurs as the left ventricle begins to relax [12]. This temporal point occurs at the end of the diastolic isovolumetric relaxation phase of the cardiac cycle. Though this point is beyond the actual end systolic point of the cardiac cycle the chamber volume has not changed significantly and it is a reliable measure of the amount of blood remaining at the end of cardiac contraction [7]. If the leaflets of the mitral valve are not visible then the end systolic frame can be selected at the temporal point where the chamber area appears to be at its minimum [12].

Quantifying ventricular volumes from cardiac images requires coming to terms with the realities and limitations of the cardiac imaging modalities. Echocardiographic imaging for instance is currently unable to produce a complete set of multi-slice images over the extent of the ventricular chamber. Instead only cross sectional slices oriented along each of the described apical axes and the single short axis are typically

acquired. Ventricular volumes are measured from this minimal set of cardiac images through the use of approximation techniques discussed below. In contrast, cardiac magnetic resonance images are typically acquired in a multi-slice fashion over the entire extent of the left ventricular volume. Ventricular volume measurements can then be made by defining the ventricular volume in each of the slices and then summing the volumes together. Volumes measured using cardiac MRI are limited in their accuracy by slice thickness partial volume effects and in systolic images by the blending of myocardial and blood signals. Both of these limitations tend to interfere with the proper identification of the ventricular endocardial border and the position of the mitral and aortic valve planes. An additional consideration is that echocardiographic images are acquired in real-time while MR images require that the image acquisition be performed using cardiac gating techniques over many cardiac cycles.

Measuring the left ventricular volume from a set of minimal image data is required when utilizing certain imaging modalities and is otherwise desirable to allow for expediency. There are several accepted techniques for approximating the volume of the left ventricle from parameters measured on cardiac images. The area length method of approximating the left ventricular volume is based upon measuring only the chamber area and the long axis length from a centered apical slice. On either the two-chamber slice or the four-chamber slice the endocardial border is outlined using a computer. The chamber area and long axis length are determined by the computer from this border using the image voxel dimensions. This information is used to generate an approximate volume according to the algorithm illustrated in Figure 2.7 [12]. Taking into

JCSF LIBRARY

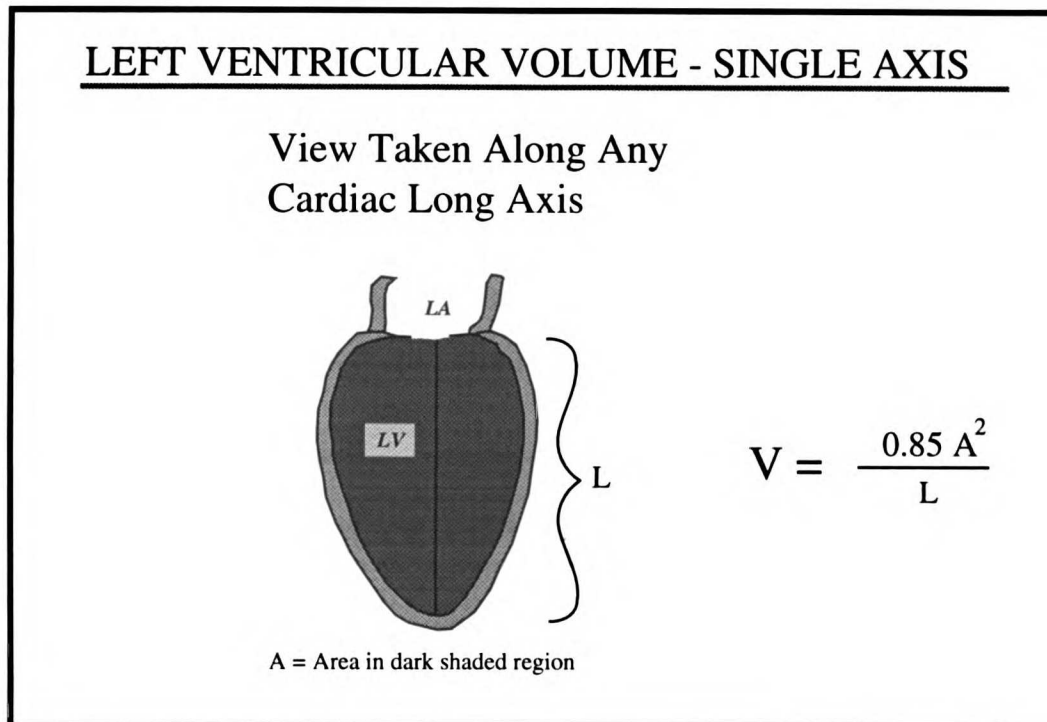


Figure 2.7 Single plane area length method for approximating the left ventricular volume [12].

account only one cross sectional image this technique is not expected to be a very accurate method. It is recommended that this method be used only when one apical image is available or usable [12].

A more accurate volume approximation technique commonly used in echocardiography is the biplane method of discs. In this technique cardiac images are acquired along both of the apical long axis orientations. The left ventricular chamber is then outlined in both images. These boundaries are then used by the computer to determine the chamber long axis in each orientation. The next step in the algorithm is to divide the left ventricular volume into approximately 20 volume discs with axial center positioned along the cardiac long axis. The diameter of the discs is determined by the computer from both of the boundaries drawn on the two apical orientations.

The volumes occupied by the discs are then summed up to yield the total volume of blood contained within the left ventricle. This algorithm is illustrated in the drawings and formula shown in Figure 2.8 [12]. It is not unusual to find a difference in the length of the left ventricular long axis measured from the two-chamber image and the four-chamber image. As long as this difference is less than 20% the method of discs can still be utilized. It is recommended that the longer of the two apical axes be used in

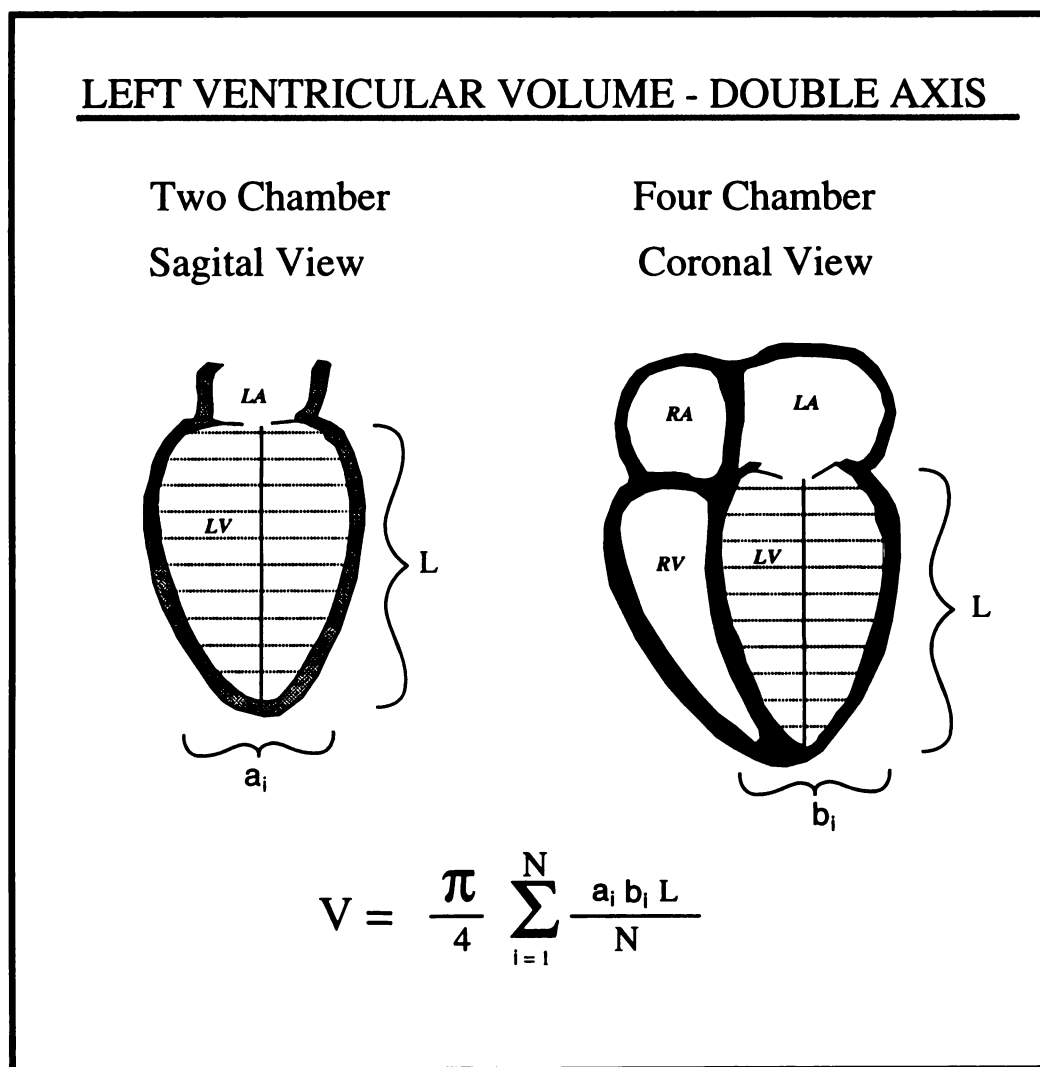


Figure 2.8 The biplane method of discs method for approximating the left ventricular volume [12].

the calculation of ventricular volume. A correction for discrepancies in the lengths of the apical axes is to proportionally lengthen the width of the disc segments along the shortened axis to match the disc segments along the longer axis [12].

The two described approximation techniques are used to determine the ventricular volume in both the end diastolic and the end systolic image frames. Published values for normal left ventricular end diastolic volume measured using these approximation techniques are presented in Table 2.5. The limitation of these approximation techniques is their reliance upon preconceived notions of the shape of the cardiac chamber and the hope that the cross sectional image acquired is representative of what would be found for any slice orientation along the apical long axis. Clearly if the chamber narrows in a non-homogenous manner then the presented approximation techniques will suffer. This problem is what makes multi-slice imaging of the heart superior although certainly more time consuming as the endocardial volume is traced in each cardiac slice.

APPROXIMATION TECHNIQUE FOR DETERMINING LEFT VENTRICULAR VOLUME	END DIASTOLIC CHAMBER VOLUME MEAN \pm SD (RANGE) ml
AREA LENGTH FOUR-CHAMBER APICAL VIEW: NORMAL MALE	112 \pm 27 (65-193)
AREA LENGTH FOUR-CHAMBER APICAL VIEW: NORMAL FEMALE	89 \pm 20 (59-136)
AREA LENGTH TWO-CHAMBER APICAL VIEW: NORMAL MALE	130 \pm 27 (73-201)
AREA LENGTH TWO-CHAMBER APICAL VIEW: NORMAL FEMALE	92 \pm 19 (53-146)
BIPLANE METHOD OF DISCS USING BOTH APICAL VIEWS: MALE	111 \pm 22 (62-170)
BIPLANE METHOD OF DISCS USING BOTH APICAL VIEWS: FEMALE	80 \pm 12 (55-101)

Table 2.5 Table of normal left ventricular end diastolic volumes as determined by approximation methods from echocardiographic images. Males: n = 52 and females: n = 84 [12].

Volumetric quantification techniques can also be used to determine the left ventricular mass. Using multi-slice tomographic imaging techniques, such as magnetic resonance imaging, the volume occupied by the left ventricular myocardium can be measured in each slice and then summed to yield a total myocardial volume. The myocardial volume is measured at the end diastole and is defined between the epicardial and the endocardial edges as previously described. Internal cardiac structures are again ignored and standardized selection of the image window values is again important. Myocardial mass is determined by multiplying the number of myocardial voxels in the measured volume by the voxel dimensions and the density of myocardium, 1.05 gm/ml [12].

Limitations in echocardiographic images again require that volume approximation techniques be utilized to determine the volume occupied by the left ventricular myocardium. An area length technique is one such method for measuring the myocardial mass (Figure 2.9) [12]. The formula for the area length volume requires two image orientations: a short axis image at the papillary muscle tip level and an apical long axis image. A more sophisticated technique commonly used in echocardiography is the truncated ellipsoid technique (Figure 2.9) [12]. In this formula the typical shape of the myocardium is taken into account to hopefully produce a more reliable measure of the myocardial volume. The same image orientations used in the area length myocardial volume measurement are used in the truncated ellipsoid measurement. Published echocardiographic normal values for the left ventricular myocardial mass found using the truncated ellipsoid technique are listed in Table 2.6. As was the case with the

JCSF LIBRARY

chamber volumes the myocardial volume approximation techniques suffer when the myocardium is not homogeneously distributed. It is expected that a more accurate measure of myocardial mass can be achieved by summing the entire myocardial volume visible in the multi-slice MR images.

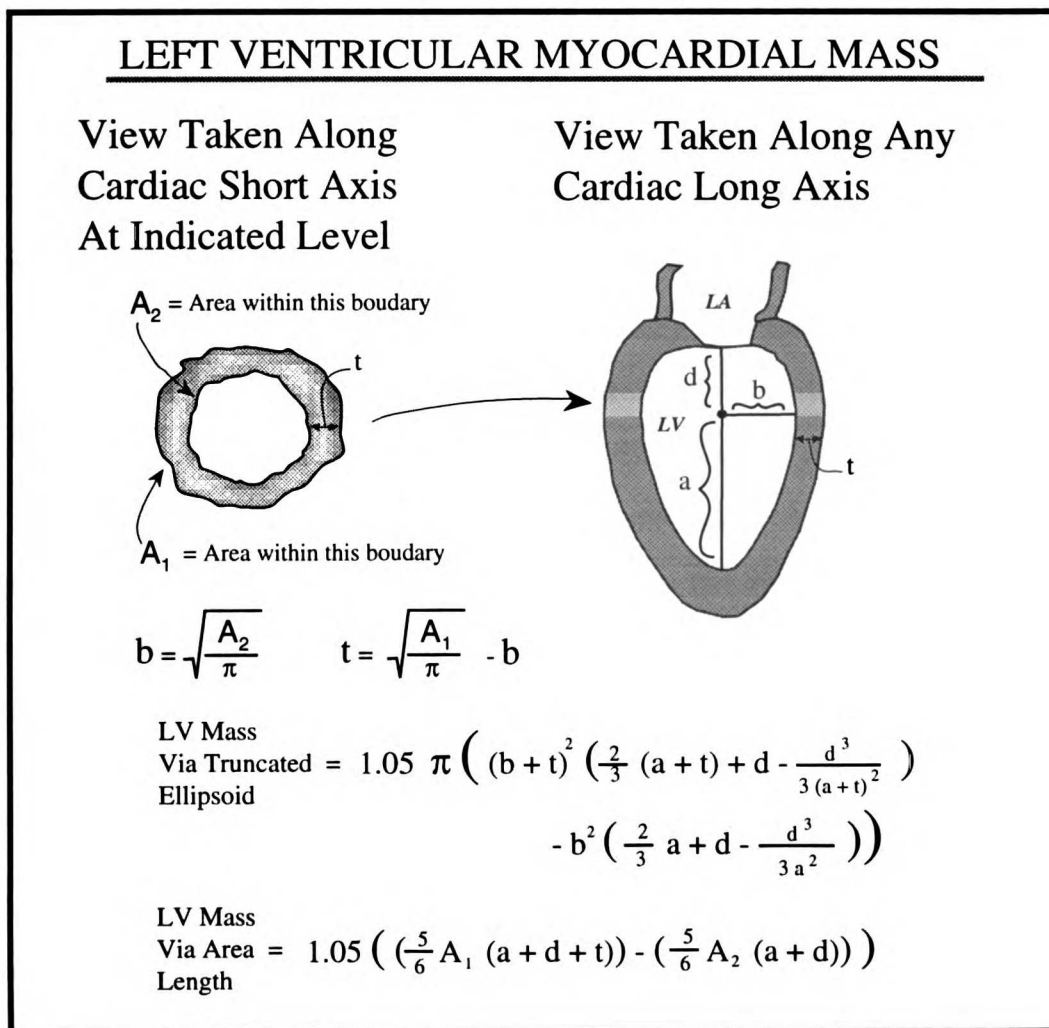


Figure 2.9 Left ventricular myocardial mass approximation method [12].

NORMAL LEFT VENTRICULAR MASS	
(MEAN \pm SD) gm	
MALES	148 \pm 26
FEMALES	108 \pm 21

Table 2.6 Table of normal left ventricular mass determined by approximation using the truncated ellipsoid technique from echocardiographic images. Males: n = 44 and females: n = 40 [12].

The volumetric measurements described above are global in their scope. They relate the state of the heart as a whole without discriminating regionally. Cardiac conditions may affect only a specific region of the myocardium as is the case with coronary artery disease where the flow of blood to a localized region of the myocardium may be interrupted. As introduced in Section 2.3, localized myocardial disease can result in myocardial contractility dysfunction. The common technique for analyzing regional myocardial contractility is based upon the examination of myocardial wall motion. The normal pattern of motion that the left ventricular myocardial walls follow was described in Section 2.3.

Analysis of myocardial wall motion can be either qualitative or quantitative. The qualitative approach entails displaying the acquired images in a cine format and observing the wall motion. A standardized segmenting scheme divides the myocardium into distinct regions and a scoring system is applied to describe the wall motion [12]. A more quantitative approach is to draw endocardial boundaries on the cardiac images from the end diastolic phase to the end systolic phase. Images acquired in the apical long axis orientation are often used for wall motion analysis in order to detect abnormal motion of the apex [13]. The endocardial borders are then superimposed by a computer onto a single

image. If any extrinsic cardiac motion (i.e. unwanted motion of the echocardiography probe or patient motion) is detected then a floating frame of reference must be used in order to properly align the endocardial boundaries. The physical shift in either a known anatomic landmark or the boundary center of mass [13] are used to determine the correction shift for the frame of reference in each of the temporal images. This correction shift is designed to remove the effects of the extrinsic cardiac motion. The distance that the endocardial border has moved during contraction in each temporal image is then measured and displayed numerically or in a graphical fashion relative to the end diastolic border. The result is examined for asymmetries or lack of motion which may be indicative of a contractility abnormality.

When attempting to study localized cardiac tissue every tomographic imaging modality suffers from the intra-cardiac motion that occurs during cardiac contraction. The downward motion of the cardiac base as the heart contracts will shift the original cardiac tissue out of view from a fixed short axis acquisition slice bringing into the slice a physically different portion of the cardiac tissue. In a similar fashion the rotation of the heart about the cardiac long axis during contraction will shift the original cardiac tissue out of view from a fixed apical long axis slice. Techniques have been developed which allow the cardiac tissue to be "tagged" or marked in such a fashion that the intra-cardiac motion can be assessed [14]. These methods are often times used not to trace the motion of a specific tissue but to illustrate the overall motion of the heart walls during contraction.

JCSF LIBRARY

The primary reason why the study of wall motion has emerged as the most common technique of contractility analysis is due to the poor resolution of the epicardial border of the myocardium in common imaging modalities such as echocardiography [13]. When not bound by limitations in visualizing the epicardial border, as is the case with MRI, it becomes possible to attempt a different approach to myocardial contractility assessment. The measurement and analysis of myocardial wall thickness is one such alternative technique. Determining the myocardial wall thickness begins with the definition of the endocardial boundary and the epicardial boundary on either a short axis image or an apical image. Short axis image orientations are limited in that the thickness of the apex can not be determined. The endocardial and epicardial boundaries are used to identify the myocardial center of mass. The myocardial wall thickness is specified as a thickness at a particular radial location around the circular ventricular cross section. The thickness is calculated by taking the difference of the radial length from the left ventricular center of mass to the epicardial border and the radial length from the same center of mass to the endocardial border. Sweeping the radial line through 360 degrees completely specifies the radial thickness of the left ventricular cross section. Myocardial thickness is determined for each temporal image from the end diastolic temporal phase to the end systolic temporal phase. A comparative graph of radial thickness is then generated relative to the end diastolic myocardial thickness over each of the temporal image frames.

Normally as the heart contracts it is expected that the radial thickness of the myocardium increases. As discussed in Section 2.3 myocardial thickening is directly related to the contractility of the

JCSF LIBRARY

myocardial tissue. If the contractility is reduced regionally then there should be concurrent reduction in the change in thickness over the same region. Myocardial wall thickness has a number of advantages over the myocardial wall motion method of contractility assessment.

First, thickness measurements are relative measurements made between two structures in the same image. Any extrinsic cardiac motion will be subtracted out and hence will not require a readjustment of the frame of reference as was the case in wall motion analysis. This reduces potential errors caused by misalignment of the systolic and diastolic endocardial boundaries which may mask actual myocardial abnormalities or introduce false myocardial abnormalities.

Second, it has been found that myocardial thickness is more sensitive to localized abnormalities than cardiac wall motion. This is conveyed in reports that wall thickness is superior at distinguishing infarcted myocardial zones from adjacent non-infarcted cardiac zones [13]. The additional information provided by the inclusion of the epicardial boundary is the reason for the increased sensitivity to the state of the myocardium. An example of such a situation is when the endocardial border is moving normally while the epicardial border moves abnormally. In this case a wall motion analysis of the myocardium appears normal, but a thickness analysis will appear abnormal.

Finally, wall thickness information gathered over the entire cardiac volume can be correlated directly to the physical anatomy of the heart. This information can be used in identifying and tracking a region of myocardial

tissue as it moves from one image plane to another. Cardiac wall motion analysis provides little anatomic information which could be used to identify and follow cardiac structures as they move through several image planes.

There are also disadvantages in myocardial wall thickness measurements. If the epicardial boundary is not clearly visible then the measured thickness can not be considered accurate. When calculating the myocardial thickness it is assumed that the projected radii will intersect the endocardial and epicardial boundary at a right angles. This may not be the case if the cardiac contraction is asymmetric. If the radial lines intersect the myocardial boundaries at an oblique angle it is likely that a distortion of the wall thickness measurement will occur [13]. It is also possible that the myocardial wall thickness measurement may be hindered by what is known as "threshold phenomenon" [13]. This effect describes a situation where an upper limit is reached in the percentage of tissue affected by myocardial ischemia or myocardial infarction. Beyond this limit there will be no further decline in wall thickening. Hence it is possible that the measured wall thickness may underestimate the actual myocardial disease.

It has been reported that, for all of the apparent advantages of myocardial wall thickness analysis, when the myocardial thickness is compared directly with myocardial wall motion they both tend to correctly identify and describe occurring myocardial dysfunction [13]. The varying sensitivity of these two techniques is the remaining issue which is still being examined. In the foreseeable future there will still be clinical

environments that will be unable to produce myocardial wall thickness measurements due to limitations in cardiac imaging hardware and expertise. In situations though where myocardial thickness can be measured it is expected that this will become a standard part of the cardiac imaging functional examination of the cardiovascular system.

UCSF LIBRARY

CHAPTER 3

CARDIAC MAGNETIC RESONANCE IMAGING

3.1 INTRODUCTION TO MAGNETIC RESONANCE

Cardiac magnetic resonance (MR) imaging is the modality which is the primary focus of this dissertation. The methods presented in later chapters will each be focused on either improving the image quality of cardiac MR images or the investigation of cardiac functional analysis techniques applied to cardiac MR images. In preparation for these chapters it is first necessary to discuss some of the basic principles of MR imaging. The following discussion is by no means a complete discussion of the concepts and issues involved in the physics of MR acquisition. Instead what follows is a brief discussion targeted towards providing the necessary framework for later chapters. For a more complete treatment of MR imaging the references [16-22] should be consulted.

Magnetic resonance is a physical phenomena of the atomic nucleus. Inside the nucleus are protons and neutrons. These nucleons each have a angular momentum and a colinear magnetic moment [21]. The angular momentum and the magnetic moment of these nucleons add to yield the respective nuclear angular momentum, \mathbf{J} , and the nuclear magnetic moment, μ which are related to each other as follows [21]:

$$\mu = \gamma \mathbf{J} \quad (3.1)$$

γ is known as the gyromagnetic ratio which is a constant specific to each nuclear isotope [21]. A nucleus of special interest to MR is the proton, ${}^1\text{H}$.

This atom, with a single nucleon, has the highest MR sensitivity of the stable isotopes and is the most common isotope of hydrogen with a natural abundance of 99.9% [21]. The proton is also important because it is very common in human tissue. For all of these reasons the proton is the atom of choice when producing MR images.

A complete description of the nuclear angular momentum and the nuclear magnetic moment requires the concepts and tools of quantum mechanics [23]. However, MR imaging acquisitions are produced from the response of a very large ensemble of protons. The correspondence principle allows the behavior of the net proton magnetic moment of such a large ensemble of protons to be described using classical electrodynamics. Classically, a magnetic moment in a static magnetic field, \mathbf{B}_0 , has potential energy given by Equation 3.2:

$$E = -\boldsymbol{\mu} \cdot \mathbf{B}_0 \quad (3.2)$$

In order to make use of Equation 3.2 it is necessary to first recall from quantum mechanics that the proton has spin of $\frac{1}{2}$. This implies that the proton's angular momentum is quantized and can be in only one of two possible states: spin up or spin down [25]. Quantum mechanics sets the angular momentum for these two states to have component values along the direction of the applied magnetic field equal to [21, 25]:

$$\mathbf{J}_{\text{spin up}} = \frac{1}{2} \frac{\hbar}{2\pi} \quad (3.3a)$$

$$\mathbf{J}_{\text{spin down}} = -\frac{1}{2} \frac{\hbar}{2\pi} \quad (3.3b)$$

where h is Planck's constant. Equation 3.3 and Equation 3.1 imply that the proton magnetic moment in a static magnetic field is also quantized into either the spin up state or the spin down state. Note that the magnetic moment is parallel to the applied magnetic field in the spin up state and anti-parallel to the applied magnetic field in the spin down state. The energy of these two quantized states can be found through Equations 3.3, 3.1 and 3.2 to be:

$$E_{\text{spin up}} = - \frac{\gamma h B_0}{4\pi} \quad (3.4a)$$

$$E_{\text{spin down}} = \frac{\gamma h B_0}{4\pi} \quad (3.4b)$$

Among these two proton energy states, spin up has the lower energy and their energy separation is:

$$\Delta E = \frac{\gamma h B_0}{2\pi} \quad (3.5)$$

When an ensemble of protons is placed into the B_0 magnetic field a thermal equilibrium is established between the number of protons in the spin up state and the number of protons in the spin down state. The distribution of this equilibrium follows a Boltzmann's distribution and is given by the following equation [25]:

$$\frac{N_{\text{spin down}}}{N_{\text{spin up}}} = e^{-\Delta E/kT} \quad (3.6)$$

In Equation 3.6, $N_{\text{spin down}}$ and $N_{\text{spin up}}$ are the population of protons with magnetic moment in the higher and lower energy states respectively. T is

the absolute temperature and k is Boltzmann's constant. ΔE comes from Equation 3.5. The equilibrium satisfying Equation 3.6 is such, that for the magnetic fields used in MR imaging there will be a surplus of protons with magnetic moment in the spin up orientation. This surplus is large enough that the net magnet moment in an image voxel will have a measurable MR signal.

Classical electrodynamics shows that a magnetic moment placed in a magnetic field will experience a torque (τ) as expressed by the following equation [24]:

$$\tau = \mu \times \mathbf{B} \quad (3.7)$$

Classical electrodynamics also shows that the torque acting on an object is equal to the rate of change of the object's angular momentum [24]:

$$\tau = \frac{\partial \mathbf{J}}{\partial t} \quad (3.8)$$

Restating Equation 3.7 using Equation 3.8 it can be said that the rate of change of a magnetic moment's angular momentum is set by the magnetic field that the magnetic moment experiences according to the following equation:

$$\frac{\partial \mathbf{J}}{\partial t} = \mu \times \mathbf{B} \quad (3.9)$$

Equation 3.9 can be applied when classical mechanical dynamics are valid. This will be the case for the net angular momentum, \mathbf{J}_{net} , and the net magnet moment, μ_{net} , of the nuclei in a typical MR imaging voxel.

Equation 3.9 can be converted to a more useful form by differentiating Equation 3.1 and applying the result to recast Equation 3.9 into the following form:

$$\frac{\partial \mu_{\text{net}}}{\partial t} = \gamma \mu_{\text{net}} \times \mathbf{B} \quad (3.10)$$

The net magnet moment for an ensemble of protons has an equilibrium value determined by Equation 3.6. The net magnet moment is customarily termed the net magnetization, \mathbf{M} . Replacing μ_{net} in Equation 3.10 with \mathbf{M} and assuming a γ suitable for the proton gives the differential equation:

$$\frac{\partial \mathbf{M}}{\partial t} = \gamma \mathbf{M} \times \mathbf{B} \quad (3.11)$$

that has a solution which details the motion of the equilibrium magnetization in a magnetic field, \mathbf{B} . The solution to Equation 3.11 is significant to MR imaging because the motion of the net magnetic moment will cause a measurable electrical signal in a correctly designed and placed conductive wire coil. This is the MR signal. Equation 3.11 implies that the magnetic moment will precess about the applied magnetic field at a specific angular frequency. This frequency is given by the Lamor equation [21]:

$$\omega = -\gamma B \quad (3.12)$$

Equation 3.11 and Equation 3.12 set out the two most important principles of MR imaging. From 3.11 it is known that the net magnetization will spin or precess about the applied magnetic field. Equation 3.12 fixes the frequency at which this precession will take place. The process of MR imaging will be to alter the applied magnetic field in such a manner as to

cause a selected portion of an object's magnetization to tip away from equilibrium and point into a plane perpendicular to that of the original magnetic field. The applied magnetic field is then configured to spatially encode the MR signal as the magnetization precesses at the Larmor frequency about the applied magnetic field. The significance of the Larmor equation is actually much more than has been indicated. The method which is used to tip the magnetization away from equilibrium requires applying an oscillating magnetic field which varies at the magnetization's precessional frequency, the Larmor frequency. This frequency is determined by the imaged nuclear isotope (through the value of γ) and the static magnetic field. This is the nature of MR, that the magnetization will be altered by the absorption of energy from an oscillating magnetic field only at a specific frequency determined by Equation 3.12 and the received signal frequency is also set by Equation 3.12.

The magnetization, after it has been tipped away from equilibrium and the perturbing oscillating field is removed, will eventually return to its equilibrium state. MR tissue contrast is largely a result of the fact that this rate of return to equilibrium, or relaxation, varies from tissue to tissue. This relaxation introduces a temporal variation in the magnetization intensity as detected by the MR signal reception coil. MR image intensity is a measure of the amount of voxel magnetization which remains measurable in the tipped plane at a specific time point after the magnetization has been moved from equilibrium. This time point is referred to as the TE or echo time. It is necessary to tip the magnetization several times during the acquisition of a MR image. The time between tips,

ARVARD LIBRARY

the amount of time allowed for the magnetization to return to equilibrium, is referred to as the TR or repetition time of the acquisition.

In order to account for the behavior of the magnetization after it has been tipped away from equilibrium it is necessary to expand Equation 3.11 to include the relaxation processes. This new differential equation is known as the Bloch equation:

$$\frac{\partial \mathbf{M}}{\partial t} = \gamma \mathbf{M} \times \mathbf{B} - \frac{(M_z - M_0) \mathbf{k}}{T_1} - \frac{M_x \mathbf{i} + M_y \mathbf{j}}{T_2} \quad (3.13)$$

\mathbf{M} is the net proton magnetic moment, \mathbf{B} is the applied magnetic field, γ is the gyromagnetic constant for the proton, M_0 is the magnitude of the equilibrium magnetization oriented along the axis of static magnetic field, \mathbf{B}_0 (z axis). M_x , M_y , M_z are the components of \mathbf{M} along each of the Cartesian coordinate axes. T_1 is the spin-lattice relaxation time constant and T_2 is the spin-spin relaxation time constant. The T_1 decay is a representation of the previously indicated process where the magnetization returns to its equilibrium value oriented along the axis of \mathbf{B}_0 , the longitudinal direction. T_2 is a second relaxation effect which occurs within the transverse plane perpendicular to the longitudinal direction. This relaxation causes the ensemble of nuclei in the precessing magnetization to dephase and hence the measured MR signal decreases. A similar effect is also represented by a revised T_2 decay constant not shown in Equation 3.13, T_2^* . T_2^* includes the dephasing in the precessional plane due to magnetic field inhomogeneities. This dephasing effect is constant with respect to time but varies with position. It is possible to compensate for this dephasing by tipping the magnetization through an additional 180 degrees thereby

allowing the magnetization precession to reverse the inhomogeneity component of the dephasing. At the time point equal to twice the time when the 180 degrees tip occurs the magnetization will be rephased from the inhomogeneity effect. After this time point the magnetization in the perpendicular plane will begin to dephase again from the same inhomogeneity effect. Among these time constants T_2^* is the shortest followed by T_2 and then T_1 .

Solutions to the Bloch equation can be written for the magnetization along each of the coordinate reference axes. These equations describe the time course of the magnetization after it has been tipped from equilibrium at $t = 0$. Including appropriate boundary conditions for $t = 0$ yields the following solutions to Equation 3.13:

$$M_{x,y}(t) = M_{x,y}(0) e^{i\omega_0 t} e^{-t/T_2} \quad (3.14a)$$

$$M_z(t) = M_z(0) e^{-t/T_1} + M_0 (1 - e^{-t/T_1}) \quad (3.14b)$$

These equations assume that the inhomogeneity component of the T_2^* relaxation effect is fully compensated. ω_0 is the Larmor frequency for the static magnetic field found from Equation 3.12. $M_z(0)$ and $M_{x,y}(0)$ are the boundary values for these respective equations at $t = 0$, right after the magnetization excitation has been completed. The cardiac MR imaging technique to be presented shortly tips the magnetization by 90 degrees into a plane perpendicular to the static magnetic field. Hence $M_z(0)$ will equal zero since there will be no magnetization left oriented along the z axis at $t = 0$. Assuming that just before $t = 0$ the magnetization had fully recovered to its equilibrium value along the static magnetic field axis, then $M_{x,y}(0)$

will equal M_0 . Hence the above equations can be rewritten using these boundary value assumptions to be:

$$M_{x,y}(t) = M_0 e^{i \omega_0 t} e^{-t/T_2} \quad (3.15a)$$

$$M_z(t) = M_0 (1 - e^{-t/T_1}) \quad (3.15b)$$

These equations are very useful for estimating the magnetization in the respective planes once the T_1 , T_2 and ω_0 values are known. While ω_0 will be fixed for all tissues, the relaxation constants are not fixed. Each of these parameters will also vary with the strength of the static magnetic field. Reference [21,27,28] can be consulted for actual values of these parameters.

Up until now it has been taken for granted that it is possible to tip the magnetization from equilibrium to a plane perpendicular to the static magnetic field. This is accomplished by applying a RF pulse at the proton Larmor frequency along an axis orthogonal to the static magnetic field. When a constant amplitude pulse is applied for the appropriate time duration the magnetization will be tipped onto the remaining axis, orthogonal to both the static magnetic field axis and the applied RF axis. This magnetization will be coherent at the moment it is tipped into the orthogonal plane. As the magnetization moves away from the static field axis it begins to precess about the static magnetic field. As previously indicated both the T_2 and the inhomogeneity processes will disrupt the coherence of the magnetization. To calculate the time duration needed for the applied RF pulse the following equation is used [19, 26]:

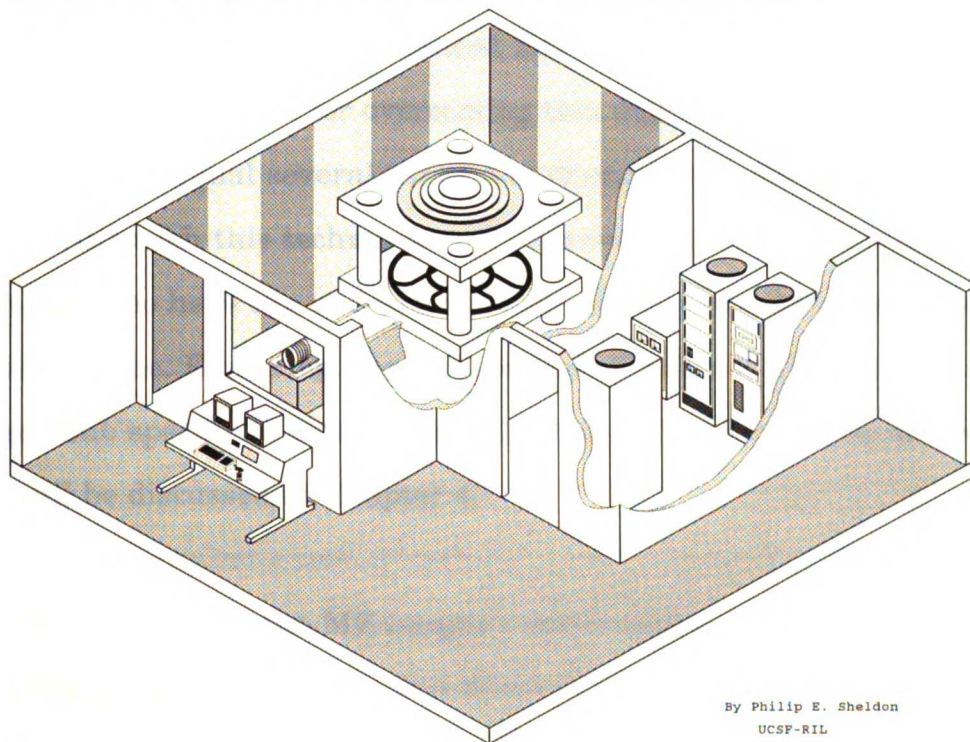
$$\theta = \gamma B_{RF} T_{RF} \quad (3.16)$$

B_{RF} is the magnitude of the applied oscillating magnetic field. T_{RF} is the duration of the RF pulse. The oscillatory frequency of B_{RF} is set by Equation 3.12. Note that the magnetic field along the axis of the static magnetic field, including the applied gradient magnetic fields to be discussed in the next section, is the determining factor of ω , the oscillatory frequency of B_{RF} . The flip angle, θ , will be either 90 degrees or 180 degrees for the imaging protocols discussed in this dissertation. The 90 degree pulse will flip the magnetization away from equilibrium and begin the process of building a MR image. The 180 degree pulse will flip the magnetization in order to refocus the inhomogeneity component of the T_2^* dephasing.

This completes the introduction to the physical properties necessary to construct an MR image. In the next section an introduction of the MR imaging hardware is presented. A description of the techniques for spatially encoding the MR signal for a specific image voxel will also be discussed along with the application of these techniques to acquisition of multi-slice cardiac MR images. What follows, as was the case with this section, will necessarily not be comprehensive in its nature. For a more complete description of MR imaging hardware and MR imaging acquisition techniques the following references should be consulted: [19-22].

3.2 MAGNETIC RESONANCE IMAGING TECHNIQUES

A magnetic resonance imaging device is composed of a magnet, a set of orthogonal gradient coils, a RF transmitter/receiver system, and a digital computer with image display capabilities. The MR magnet is designed to produce a sufficiently homogeneous static magnetic field over a volume large enough to encompass the desired imaging volume [22]. In common clinical practice today are found MR imagers with magnetic fields ranging from 0.064 Tesla up through 1.5 Tesla. Toshiba America MRI (located in South San Francisco, CA) manufactures a permanent magnet based low field MR system called the Toshiba Access MR Imager. The static magnetic field strength for this system is 0.064 Tesla and a schematic diagram of its appearance is shown in Figure 3.1. This is the MR imaging device used to produce the images presented throughout this dissertation.



By Philip E. Sheldon
UCSF-RIL

Figure 3.1 Diagram of a Toshiba America MRI Access Imager.

The strength of a MR imager's magnetic field is an important issue with a variety of implications. Practically speaking, as the magnetic field strength increases so does the MR imager's manufacturing and maintenance costs [29]. This can have significant adverse effects on the utilization and availability of a MR imager. In the cost conscious environment that exists today there is a great incentive to take advantage of the cost savings inherent in low field MR imagers.

The impact that magnetic field strength has on actual MR images is an issue relevant to this dissertation. A reduced static magnetic field in a MR imager is accompanied by a correlated reduction in the signal to noise ratio found in the acquired MR images. This is a result of the reduced magnitude in equilibrium magnetization and resonant frequency which occurs at lower static magnetic field strengths. The reduced equilibrium magnetization will result in a reduced MR signal which is a function of magnetization. A method for overcoming this deficit in signal to noise is to reacquire a MR signal several times and then average these MR signals together. Although this technique will improve the image signal to noise ratio it will also have the undesired result of increasing the total image acquisition time. Exploring another method of improving the image signal to noise ratio specific to cine cardiac imaging was a goal of this dissertation and it will be discussed in Chapter 4.

The strength of the MR imager's static magnetic field will further impact the acquired images in that tissue T_1 relaxation constants are dependent upon magnetic field strength. Specifically, T_1 relaxation constants shorten in response to decreasing magnetic field [28,29]. In an

imaging procedure the tissue magnetization is driven to a steady state value determined by the tissue T_1 relaxation constant and the imaging procedure's TR value. Shorter T_1 relaxation constants result in a steady state tissue magnetization which more quickly approaches the equilibrium magnetization [29]. This allows for more efficient utilization of the available magnetization which may partially compensate for the loss in equilibrium magnetization which occurs at lower magnetic fields. Image artifacts can also be affected by the static magnetic field strength as low field MR imagers have been reported to have reduced sensitivity to motion artifacts [29]. A potential source of phase encoding artifacts can be related to the duration of the tissue T_1 relaxation constants and hence also be dependent upon the static magnetic field strength. This will be discussed further in Section 3.3 as it relates to cardiac imaging. Finally, low field MR imaging also has the potential benefit of enhanced tissue contrast as well as reduced RF power deposition in the imaged tissue [29].

MR images are acquired through a process of altering the magnetic field within a MR imager in order to excite and spatially localize an MR signal. The magnetic field is altered by energizing the three orthogonally oriented gradient coil systems of the MR imager in an ordered fashion. The gradient coil systems each produce a gradient magnetic field, directed along the static magnetic field axis, which varies in intensity with position along the independent gradient coil axes. In the spin echo imaging process, utilized in this dissertation, RF pulses are applied along with a gradient magnetic field in order to excite and then refocus the MR signal in the selected imaging slice. The MR signal is then measured by the RF reception system and the acquired time domain signal is stored using a

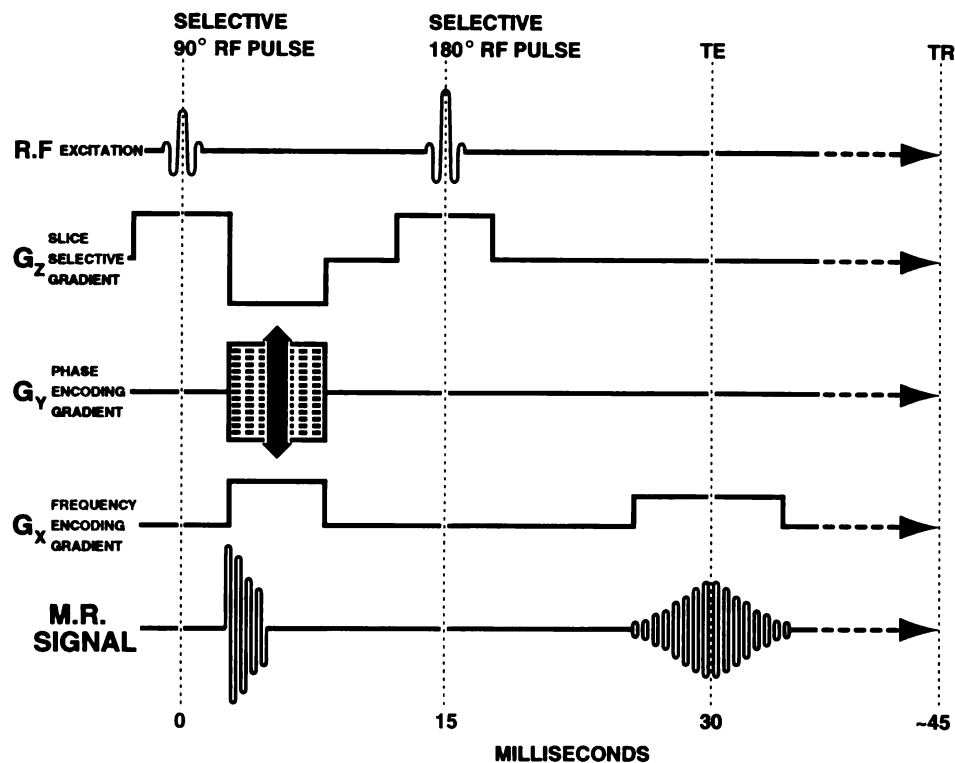


Figure 3.2 An example of a timing diagram for a spin echo MR image acquisition.

digital computer system. The sequence with which the gradient magnetic fields and the RF pulses are applied is illustrated in Figure 3.2 for a typical spin echo MR acquisition [21].

As shown in Figure 3.2 and Figure 3.4a, a MR image slice is selected for excitation by first setting up a gradient magnetic field along the desired slice axis. This gradient creates a distribution of Larmor frequency in the imaging volume along the slice axis. In the spin echo imaging technique an image slice is excited through the application of a 90 degree RF excitation pulse as the slice select gradient is maintained. This excitation RF pulse will tip the slice magnetization parallel to the static magnetic field into the perpendicular precessional plane as described in the previous section. The magnetization tipped by the excitation pulse is specified in both

slice position and slice thickness by the frequency characteristics of the perturbing RF pulse. Specifically, the frequency span of the RF pulse is tuned to correspond to the Larmor frequencies of the desired image slice.

The excited tissue magnetization precesses about the axis of the static magnetic field and induces an electrical signal in the imager's RF reception coil system proportional to the magnetization oriented in the precessional plane. This MR signal will decay in intensity with the described tissue relaxation constants. The spin echo imaging method used in this dissertation recovers the MR signal lost due to the inhomogeneity dephasing by tipping the magnetization through an additional 180 degrees at a time point equal to one half the time when the MR signal is actually measured and recorded [19, 21]. The 180 degree refocusing RF pulse is applied along with the same slice select gradient used in the original slice excitation. The frequency characteristics of the refocusing RF pulse are identical to the 90 degree excitation pulse except that the time duration of the pulse and/or the intensity will be increased in order to produce the

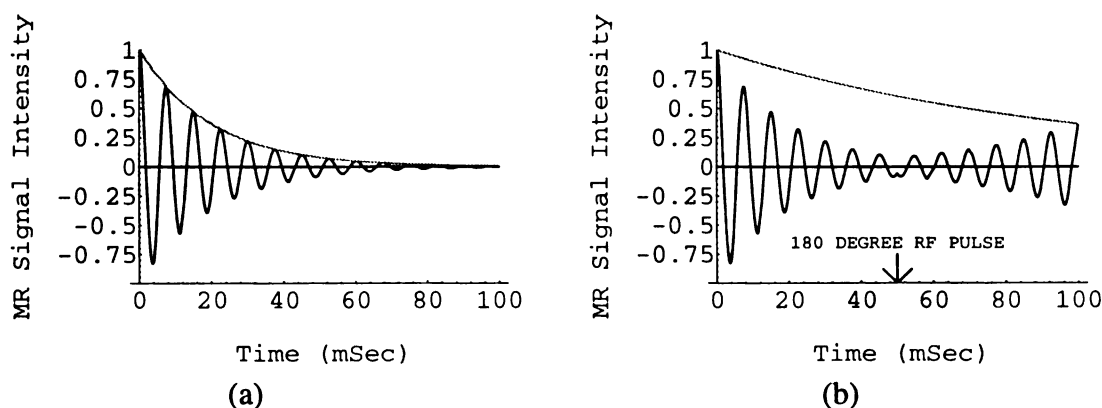


Figure 3.3 Example of MR signal. (a) Off resonance decay of an excited slice's MR signal that is not refocused for field inhomogeneity effects. Curve shows the T_2^* decay rate. (b) Off resonance decay of an excited slice's MR signal that is refocused for field inhomogeneity effects. Curve shows the T_2 decay rate.

additional rotation of the magnetization. Tipping the precessing magnetization through 180 degrees reverses the magnitude of the localized inhomogeneity dephasing and thereby allows the magnetization to be refocused by the same magnetic field imperfections that created the dephasing in the first place. The time point where the MR signal becomes refocused is termed the TE (echo time) of the acquisition procedure. An illustration comparing the MR signal with and without the refocusing pulse is found in Figure 3.3.

The refocused MR signal from the excited slice is spatially encoded by applying gradient magnetic fields orthogonal to the orientation of the slice select gradient and parallel to the axes of the slice plane. These two gradient fields are termed the frequency encoding gradient and the phase encoding gradient. The frequency encoding gradient is applied during the period when the MR signal is measured and recorded. The gradient establishes a distribution of Larmor frequency that varies linearly with position along the frequency encoding axis. The MR signal that is then acquired by the MR imager's RF receiver system is a combination of sinusoids at the frequencies established by the frequency encoding gradient. The spectral intensity of each sinusoidal signal is proportional to the total magnetization in a strip through the slice. Each strip corresponds to the Larmor frequency during the time when the MR signal is recorded (Figure 3.4b). The frequency encoded time domain signal can be processed into a frequency spectrum, representative of the slice magnetization localized to one slice dimension, by the application of a Fourier transformation.

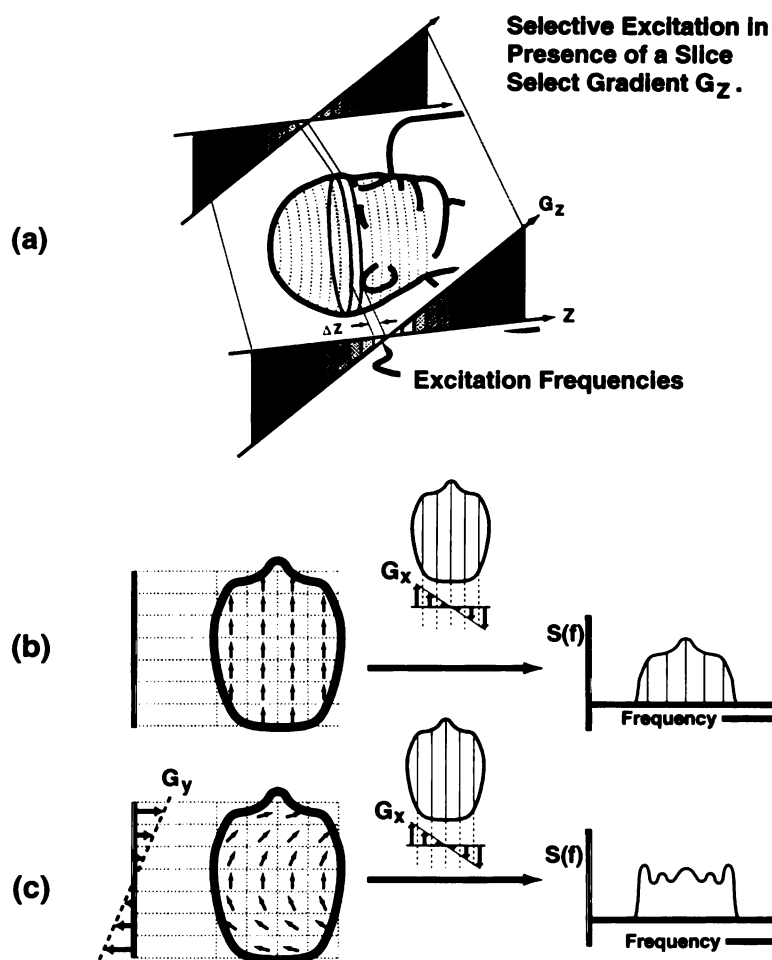


Figure 3.4 Illustrations of MR spatial encoding methods: (a) Slice select, (b) Frequency encoding, (c) Frequency encoding with phase encoding.

Phase encoding is the method used to encode the excited slice's MR signal along the second slice dimension (Figure 3.4c). Phase encoding is accomplished by applying a gradient magnetic field oriented along the unresolved slice dimension for a prescribed duration of time after the slice excitation and before the signal is recorded. The intensity of this gradient is stepped through a range of values for separately acquired time domain MR signals with identical frequency encoding (Figure 3.2). The effect of the stepped phase encoding gradient is to allow a variable precessional rate along the phase encoding axis thereby varying the phase of the MR signal

along this dimension. This will produce a sinusoidal variation in the MR signal arising from each frequency encoded strip over the range of phase encoding steps. The apparent frequency of these phase induced sinusoidal variations will vary along the phase axis just like the frequency encoding pattern. Hence the MR signal can be localized along the remaining slice dimension by aligning the acquired phase stepped time domain data to a common frequency axis strip and applying a Fourier transformation along the phase axis at each strip or frequency step. A Fourier transformation along the frequency axis of each of the acquired phase stepped MR signals then produces a complex valued two dimensional MR signal now spatially localized within the selected image slice. The final step required to produce a displayable MR image is to take the magnitude of the complex valued MR signal.

A few final notes about the spin echo imaging process. In Figure 3.2 there are pulses of the slice select and frequency encoding gradients in addition to what have already been described. These pulses are used to compensate for the dephasing that occurs to the slice magnetization due to the varying precessional frequency through the slice when a gradient magnetic field is applied. The goal of the phase encoding gradient is to impart this type of dephasing as a method of spatial encoding. Hence there is no phase compensation for this gradient. Next, spin echo acquisition procedures require a delay between the acquisition of the different phase encoded MR signals. This delay allows the magnetization to relax towards equilibrium and it is measured by the interval between the application of slice excitations given by the TR of the acquisition procedure. While the magnetization in one slice is relaxing it is possible to acquire a MR signal

from other image slices. A set of time domain data from multiple images can thus be acquired in a process where the MR signal is sequentially recorded from each of the slices at the same phase encoding step. Then the phase encoding step is advanced and the process is repeated. This process is known as multi-slice image acquisition.

The cine cardiac MR images utilized throughout this dissertation were acquired using an adapted multi-slice spin echo imaging technique synchronized to the cardiac cycle. The contractile motion of the heart prevents a free running MR acquisition from acquiring successive phase encoded MR signals from the same tissue. To synchronize the acquisition of successive phase encoded MR signals a technique known as cardiac gating is utilized. In this technique the slice excitation of each phase encoding step in a spin echo acquisition is begun at a fixed point, with respect to the R wave, along an ECG signal (Figure 2.5) measured from the imaged patient. Cardiac gating is successful because heart tissue appears to be moving in a periodic fashion through the same physical space at a fixed rate relative to the ECG signal. A cine representation of the heart contracting can be constructed from a series of images acquired at evenly spaced temporal points along the cardiac cycle. These images are acquired by advancing the interval from the R wave where the slice excitation begins by the cine frame temporal resolution through a range covering the entire cardiac cycle. The Toshiba Access imager's cardiac imaging protocol utilizes the temporal separation of the multi-slice image slices as the temporal resolution required to build the progressive cine frames of the cardiac cycle.

The cine cardiac imaging procedure is thus dependent upon the heart rate of the imaged patient. The heart rate of an individual is a parameter specific to that individual and it will vary in response to a variety of external and internal stimuli. When subjected to a MR acquisition procedure a relaxed individual will usually have a heart rate of less than 80 beats per minute. Selecting 80 beats per minute as an upper bound, a trigger from the cardiac gate signal will occur at the fastest every 750 msec. The TE of the cardiac spin echo procedure used in this dissertation is 30 msec. Thus the cine cardiac acquisition protocol can accommodate fourteen multi-slice cardiac image slices and still have time remaining to prepare for the next phase encoding step and gate signal. Maximizing the number of image slices and temporal acquisition points within the period of

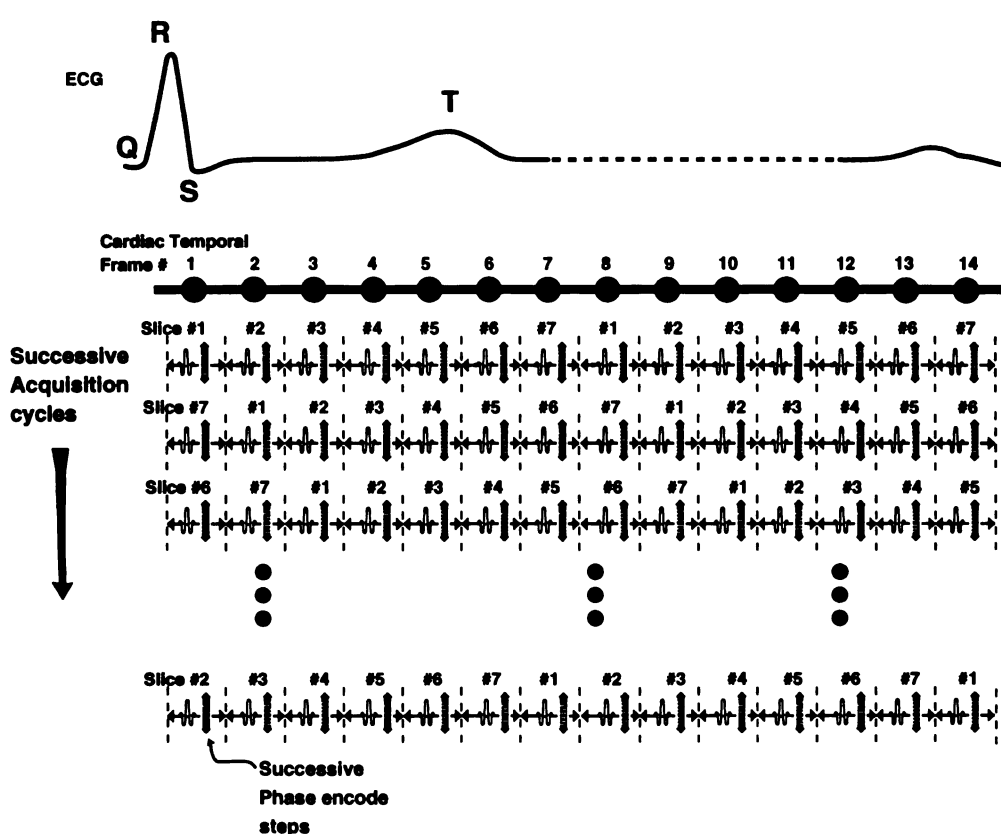


Figure 3.5 Illustration of the acquisition sequence of a cine MR cardiac protocol.

cardiac contraction results in seven spatially adjacent 10 mm thick image slices taken at fourteen sequential temporal points. With fourteen temporal data points the multi-slice imaging protocol can be doubled up to acquire time domain data from two separate temporal points for each of the seven image slices during each phase encoding step. When all of the phase steps in the acquisition protocol have been completed the order in which the images are acquired is shifted as shown in Figure 3.5 and the imaging acquisition begins again. The cine acquisition is completed after the time domain MR signals have been acquired for each of the seven slices over all of the fourteen temporal points along the cardiac contraction cycle.

The time domain MR signal from each image is reconstructed into cardiac images as described above. To display a cine of a heart contracting specialized video hardware is necessary to store each frame of the cardiac cine and then display them in a sequential series at frame rates high enough to match a reasonable heart rate. Digital computer systems are rapidly evolving to contain this hardware capability as an integral part of their component systems. Thus it is expected that most modern computers will be capable of displaying the temporal cardiac images in a cine format. An example of a single image slice of a gated cardiac imaging acquisition is displayed in Figure 4.1 for each of the fourteen temporal points in the acquisition. Enhancements and functionality of this format of cardiac imaging is the primary interest of this dissertation.

3.3 SPECIAL ISSUES RELEVANT TO CARDIAC MAGNETIC RESONANCE IMAGING

The cine cardiac MR imaging technique, as presented above, is affected by a variety of issues both unique to cardiac imaging and common to all MR imaging modalities. Unique to cine cardiac MR imaging is the role that magnetic field strength plays in phase encoding artifacts induced by the rhythmic characteristics of cardiac contraction. An examination of this issue can be made by selecting a MR acquisition procedure where only 90 degree RF slice excitation pulses are applied and refocusing RF pulses are not applied. In this acquisition procedure the steady state longitudinal (parallel to the static magnetic field) magnetization is given by Equation 3.17 as a function of M_0 , the equilibrium magnetization.

$$M_{SSz}(TR) = M_0 (1 - e^{-TR/T_1}) \quad (3.17)$$

This equation is a statement of the fact that the steady state longitudinal magnetization is a function of the TR time period between successive phase encoded acquisitions. A more complicated version of Equation 3.17 is available which takes into account the effects of the 180 degree spin echo refocusing pulse [30]. The value of the steady state longitudinal magnetization is important because it is this magnetization which is flipped into the transverse plane by the 90 degree RF slice excitation and hence directly influences the magnitude of the recorded MR signal.

Normally the acquisition TR and thus the steady state magnetization are both constant. In a cine cardiac MR acquisition this is not the case

since successive phase encode steps advance at the rate of cardiac contraction. Thus the TR of the cine cardiac acquisition will not be fixed and from Equation 3.17 neither will the steady state longitudinal magnetization. As a result of this, MR parameter quantification measurements, such as T_1 calculations, should be applied with caution.

The rate of cardiac contraction in a resting healthy individual is known to be influenced by a process known as respiratory sinus arrhythmia. In this process the heart rate is characterized by alternating periods of increasing and decreasing rates of contraction. During respiratory inspiration the heart rate tends to increase while during respiratory expiration the heart rate tends to decrease [31]. There are other types of cardiac arrhythmia which may be of concern but the case of respiratory sinus arrhythmia will serve as a satisfactory model of the effects of a variable TR during a cardiac acquisition. In this model it is expected that for typical heart rates, below 80 beats per minute, the variation in the period between R to R intervals in the ECG can range over +/- 200 msec [32]. A typical variation in the R to R interval between sequential contraction cycles may in some cases be as much as 75 msec [32].

The cine cardiac acquisition procedure described in Section 3.2 excites each slice twice over a single cardiac phase encode step in order to maximize the number of temporal frames acquired at each phase step. In this process the image slices from the later seven temporal frames will always have a fixed TR of 350 msec. The image slices from the first seven temporal frames though will have a variable TR caused by the variation in

the period of the cardiac contraction cycle. For these first seven temporal frames, assuming a typical resting heart rate of 70 beats per minute, the TR of a particular phase step may be approximately 500 msec. Based upon the assumptions given above this TR can be assumed to increase due to variations in heart rate such that a later TR may be as much as 575 msec. Likewise this TR may even later decline in value to as little as 425 msec. The effect of this variation in TR upon observed MR signal will be dependent upon the static magnetic field strength at which the MR imager operates. The reason for this dependence is that T_1 relaxation constants are a function of magnetic field as discussed in Section 3.2. This property of T_1 relaxation constants is significant because the steady state longitudinal magnetization, as related by Equation 3.17, is dependent upon not only the acquisition TR but also the T_1 of the imaged tissue.

An example of the effect of a particular static magnetic field on the steady state longitudinal magnetization in a cine cardiac MR acquisition for three magnetic field strengths currently used to perform cardiac imaging: 0.064 Tesla, 0.35 Tesla, and 1.5 Tesla, is presented below. The T_1 of

Static Magnetic Field Strength (Tesla)	Approximate Muscle T_1 (msecs)	Stead State Magnetization for TR of 500 msec	Stead State Magnetization for TR of 575 msec	Percent Difference in Steady State Magnetization
0.064	145	$0.968 * M_0$	$0.981 * M_0$	1.34 %
0.35	625	$0.550 * M_0$	$0.601 * M_0$	9.27 %
1.5	1392	$0.302 * M_0$	$0.338 * M_0$	11.92 %

Table 3.1 Steady state magnetization and static magnetic field. For measured and approximated muscle T_1 values from [28] two steady state magnetization values are calculated for two anticipated values of the cine cardiac imaging protocol's TR values. This calculation is based upon Equation 3.17. Finally the present difference of these two steady state magnetization is calculated.

muscle at these field strengths is available from [28] and is presented in Table 3.1. Table 3.1 also includes the steady state magnetization calculated from Equation 3.17 based upon two potential TR values listed above: 500 msec and 575 msec. What is significant to note from Table 3.1 is that at lower magnetic field strengths the steady state longitudinal magnetization relaxes to a value more closely approaching the equilibrium value. Hence the percent difference of the steady state longitudinal magnetization from one phase encode step to the next is reduced.

When the steady state magnetization is varied over the course of a MR image acquisition the result is a phase encode artifact. A simple example of a phase encode artifact is when the steady state magnetization is varied in a sinusoidal fashion. This will result in an image artifact where an image ghost is present in the reconstructed image data propagated along the phase encode axis. In the cine cardiac imaging procedure the steady state magnetization will vary due to inconsistencies in TR. It is difficult to predict this TR variation but the case of respiratory sinus arrhythmia provides a realistic example. In this case the TR variation may be approximated by a sinusoidal function. This translates into a steady state magnetization which is a periodic function varying in magnitude exponentially. This variation in steady state magnetization may be approximated by the sum of a series of sinusoidal signals. The resulting phase encode artifact appears as a series of image ghosts propagated along the phase encoding axis.

The phase encode artifact is further complicated by the variety of T_1 relaxation constants specific to each of the tissues within the image

JUST LIBRARY

volume. This tends to blur the image ghost found in the phase encode artifact. Table 3.1 does not give a conclusive measurement of the magnitude or position of the phase encode artifact. It does show that the magnitude of the steady state magnetization variation due to inconsistent TR values increases with magnetic field. This implies that the cine cardiac imaging technique presented in section 3.2 will be less sensitive to inconsistent TR periods as the MR imager's static magnetic field is reduced. The cardiac images acquired for this dissertation on the 0.064 Tesla Toshiba Access MR imager should thus have relatively minimal phase encode artifact compared to images acquired using the same technique at higher magnetic fields.

There is a final point to be discussed regarding the effects of inconsistent TR values upon the cine cardiac images acquired with the technique presented in Section 3.2. As described above, the fourteen acquired temporal image frames differ in that the first seven temporal frames have a variable TR while the later seven temporal frames have a fixed TR. The average TR of the first seven temporal frames is expected to be approximately 500 msec while the TR of the later seven temporal frames will be a fixed 350 msec. At 0.064 Tesla, the magnetic field used to produce the images in this dissertation, the steady state magnetization for a TR of 500 msec is $0.968 * M_0$ and for a TR of 350 msec it is $0.910 * M_0$. The difference in steady state magnetization which will occur between the first half and the last half of the temporal image frames in the cardiac cine will result in a variation in the voxel intensities unrelated to cardiac motion. This will produce an artifact within the cardiac cine which will be discussed in Section 4.2.

Another series of important issues are related to the efficiency of the implemented acquisition procedure. The cardiac gating method must be designed to accurately track the same point in the R to R interval of the ECG. The acquisition protocol should be optimized to acquire the MR signals of one phase encode step over a single cardiac cycle. In order to speed the imaging procedure signal averaging should be avoided. It will be possible to enhance the image signal to noise by post acquisition methods as presented in Chapter 4. If the cardiac images are to be obliquely reformatted, as discussed in Chapter 5, then it is desirable to spend additional acquisition time to acquire image slices covering as large a volume as possible. This will expand the field of view of the reoriented oblique images. It has been found that acquiring fourteen 10 mm slices centered in the left ventricle is a satisfactory data set for use in this dissertation. Another method of expanding the oblique reformatted image's field of view is to introduce spatial gaps between the image slices. Unfortunately this tends to reduce the image quality of the obliquely reformatted images.

Cine cardiac imaging techniques are not immune to the pitfalls that affect other MR image techniques. Partial volume uncertainties are an example of one such pitfall which can create errors in measured volumes in the blood chambers or the myocardium. Another is patient motion which must be avoided in order to maintain the integrity of the slice positions. Once the cardiac images have been acquired they can then be used to analyze the structural integrity of the heart and to assess cardiac function as introduced in Chapter 2. Examples of assessments of cardiac function

using the cardiac imaging technique discussed in this chapter will be presented later in Chapters 6, 7, and 8. In the next chapter a discussion of a technique for improving the signal to noise in these cardiac images is presented.

CHAPTER 4

FOURIER TEMPORAL PROCESSING TECHNIQUES FOR IMPROVING SIGNAL TO NOISE IN CARDIAC MR IMAGES

4.1 INTRODUCTION

In a cardiac image it is the contrast which allows the observer to discern the varied anatomy. Contrast is determined by the difference in the acquired voxel intensity for different tissues. In the case of conventional spin echo MR imaging the voxel intensity at a specific point in the image is dependent upon the acquired MR signal from the voxel tissue. The voxel MR signal is a function of the density of free spins in the voxel tissue, the T_1 and T_2 MR relaxation times of the voxel tissue, and the TR and TE MR acquisition parameters [21]. The density of free spins and the tissue relaxation constants are characteristics related to the state of the imaged tissue and are not manipulated in the non-invasive imaging protocols. The image contrast can be altered at acquisition time through the selection of the TR and TE parameters. These parameter values are chosen so as to maximize the MR signal difference for those tissues that are of interest and hence enhance the image contrast in the available acquisition period.

The observed MR signals produced in the tissue are altered by the superposition of noise onto the acquired signal. The magnitude of the noise is usually small when compared to the magnitude of the MR image. However the magnitude of the noise may be comparable to the difference in voxel intensity values of tissues with similar MR characteristics. The effect

JUST LIBRARY

of the noise in this situation is to reduce the certainty with which a particular tissue contrast can be observed [22]. In order to optimize the perceived contrast in the image it is thus desirable to reduce the noise in the image.

Methods of reducing the noise in a MR image include the use of quadrature signal detection hardware in the imaging device and the use of signal averaging in the imaging protocols. As the acquired time domain data is processed into magnitude image data it is also subjected to mathematical filtering steps which are designed to reduce the image noise. These noise reduction filters operate by exploiting features of the imaging process or properties of the noise. Temporal filtering is an example of this type of image processing.

A temporal filter operates by incorporating information gathered over time to reduce noise in a particular image. Gated cardiac imaging protocols produce multiple images of the same imaging volume at different cardiac contraction phases. These images vary over time as a result of random image noise and contraction motion of the heart. The approach of the temporal filtering method presented in this chapter is to reduce the noise while leaving unchanged the data contributing to the image of the heart contracting. In order to design an algorithm which achieves this goal it is necessary to characterize the noise and the MR signal present in the gated cardiac images. An ideal filtering algorithm will seek to separate these two elements of the acquired cardiac images and then reduce the noise wherever possible while at the same time keeping the underlying MR signal unchanged.

1000110011

4.2 CHARACTERISTICS OF GATED CARDIAC IMAGES

Gated cardiac imaging protocols generate a series of MR images which are acquired from a fixed slice volume during the different phases of cardiac contraction. In the following discussion it will be assumed that the imaging protocol results in fourteen sequential images separated by an equal time period along the cardiac cycle. It is further assumed that the protocol is a spin echo technique in which the chamber blood pool produces a small signal intensity relative to the surrounding myocardial tissue. The acquired MR signal begins as a real signal registered in the receive coil of the MR imaging device. This signal is then converted by the acquisition hardware into a digitized complex signal known as the time domain data. Image reconstruction transforms the time domain data into complex valued image data. An intensity image is then constructed by calculating the magnitude of the complex image data at each voxel location.

Cardiac images are displayed using a cine loop format where the images are rapidly presented one after another giving the appearance of a motion picture. From the cine loop it is evident that the motion occurring in the cardiac images is localized in the cardiac tissues. Other tissue structures remain relatively fixed spatially and relatively constant in voxel intensity throughout the fourteen images of the cardiac cycle. These constraints may become disrupted by extrinsic cardiac motion of the patient, by slight magnetic field drift in the imaging magnet, or by the effects of inconsistent TR periods. If throughout the cardiac cycle the images satisfy the above constraints then the image intensity at specific voxels becomes either a static voxel value resulting from a constant MR

1107 110711

signal and added noise or a dynamic voxel value with intensity variation related to myocardial motion with added noise. The complex motion of the contracting myocardium results in variation in voxel intensity due to transitions in voxel tissue from one myocardial tissue to another or from blood to myocardial tissue.

The noise in the cardiac MR images is composed of two elements: stochastic image noise and structured image noise. The structured image noise results in a variation of image intensity over an otherwise homogeneous tissue region [38, 39]. The stochastic noise can first be observed in the time domain data. This noise originates as thermal noise which occurs as a result of the conductivity of the imaging subject's body and the resistance in the acquisition coil [22, 33]. Additional thermal noise is generated from the semiconductor components used in the amplification, filtering, and sampling of the MR signal. Thermal noise is characterized as random in value, independent of time, and specified by a normal distribution. A normal distribution implies that the noise has a mean of zero and a standard deviation (σ_{ND}). After the complex time domain data has been reconstructed into an intensity image the stochastic noise is still present and retains the thermal noise characteristics [33] throughout the image with one important exception. If the magnitude of the voxel MR signal intensity is not much larger than the magnitude of the stochastic noise then the stochastic noise distribution will be altered when the magnitude of the complex reconstructed image data is taken. In this situation the superposition of the stochastic noise in voxels with minimal or no signal may result in voxels with negative intensity values [22]. When the magnitude of these voxels is taken the stochastic noise will then become

1107 1 100000

specified by a Rayleigh distribution [33]. The mean and standard deviation of the Rayleigh distributed stochastic noise are given by the standard deviation of the stochastic noise in the complex image data ($\mu_{\text{Rayleigh}} = 1.25 \sigma_{\text{ND}}$, $\sigma_{\text{Rayleigh}} = 0.66 \sigma_{\text{ND}}$) [27]. It is likely that this effect will occur in portions of the image which contain no tissue or within tissue regions of low MR signal intensity such as the blood filled cardiac chambers.

The above discussion describes the characteristics of the noise present in a single cardiac image. In each of the fourteen images in a cardiac acquisition the noise is produced from the same tissue and from the same imaging hardware. The stochastic noise in each of these images will have the same statistical characteristics. The structured noise will be assumed to be constant in value for a particular image voxel over the acquired temporal frames of the cardiac cine. Thus it is also assumed that the noise variation in individual image voxels over the sequence of cardiac images is due only to stochastic noise and it is this intensity variation that the temporal filter will be directed towards. The intensity values of sequentially static image voxels, those from tissue that is not expected to move, are sampled directly from the acquired cardiac images. Hence the temporal static voxel intensity will share the same constant MR signal value and stochastic noise characteristics that is found in each of the spatial images at this same voxel location. The assumption that the structured noise is temporally constant will be consistent with what is observed in the static image voxels. Dynamic image voxels vary temporally in intensity with stochastic noise characteristics equivalent to that found in the individual cardiac images. Dynamic image voxels will in addition have intensity variation which occurs due to myocardial tissue motion. The

1107 110111

effects of the myocardial tissue motion are usually larger than the effects of both the stochastic noise and the structured noise and hence the tissue motion is more likely to dominate the variation in temporal voxel intensity.

Applying a Fourier transform to a time varying signal produces the Fourier series coefficients necessary to reproduce the original signal through the superposition of weighted sinusoids at the specific coefficient frequencies [34]. The Fourier coefficients which describe a particular signal are complex in value and are referred to as the frequency spectrum of the original signal. The frequency spectrum resulting from the superposition of two signals is found by summing the individual frequency spectrums of the two signals [34]. Hence if the frequency spectrum of the component signals can be determined then it is possible to produce the combined signal frequency spectrum. Further, if the frequency spectrum of one of the superimposed signals is known and the final combined frequency spectrum is known, then it is possible to determine the frequency spectrum of the unknown second signal. The purpose of investigating the frequency spectrum of a time varying signal is to reveal its fundamental nature. The time varying signal for which the frequency spectrum will be investigated is the individual voxel intensity variation through the temporal sequence of acquired cardiac images.

In the case of static image voxels the frequency spectrum over the cardiac cycle will include both the constant MR signal intensity value and the intensity values of the superimposed stochastic noise. The Fourier transform of the constant MR signal will result in a frequency spectrum with DC coefficient value only. If the static voxels' MR signal is not constant

1107-10000

in value then the frequency spectrum will contain non-zero frequency coefficients other than the DC coefficient. This undesired intensity variation results from a combination of inconsistent TR values, magnetic field drift, and any extra-cardiac patient motion. The nature of the dynamic image voxels' MR signal is more complicated than that of the described static image voxels' MR signal. As a result of the variability and motion of the underlying anatomic structure of the heart it is not possible to a priori describe the frequency spectrum of the dynamic image voxels' MR signal. Instead, the combined frequency spectrum of the dynamic image voxels' MR signal and the noise is calculated from the acquired temporal voxel intensity values as will be described below.

The stochastic noise present in the cardiac images can be described as white noise [33]. The frequency spectrum of this noise will be random in value and will be bounded by a uniform frequency distribution [22]. Due to the limited number of temporal samples in the cardiac sequence the stochastic noise frequency spectrum for voxels over time will only approximate the underlying uniform distribution. Summation of the noise and the MR signal frequency spectrums results in the combined frequency spectrum expected when the Fourier transform of the temporal voxel intensities is calculated over the sequence of acquired cardiac images.

In order to continue this analysis of the gated cardiac images it is necessary to calculate the frequency spectrum of the cardiac images' temporal voxel intensities from a representative cardiac acquisition. Applying a discrete Fourier transform (DFT) to a temporal voxel's intensity signal converts the fourteen voxel intensity values into fourteen complex

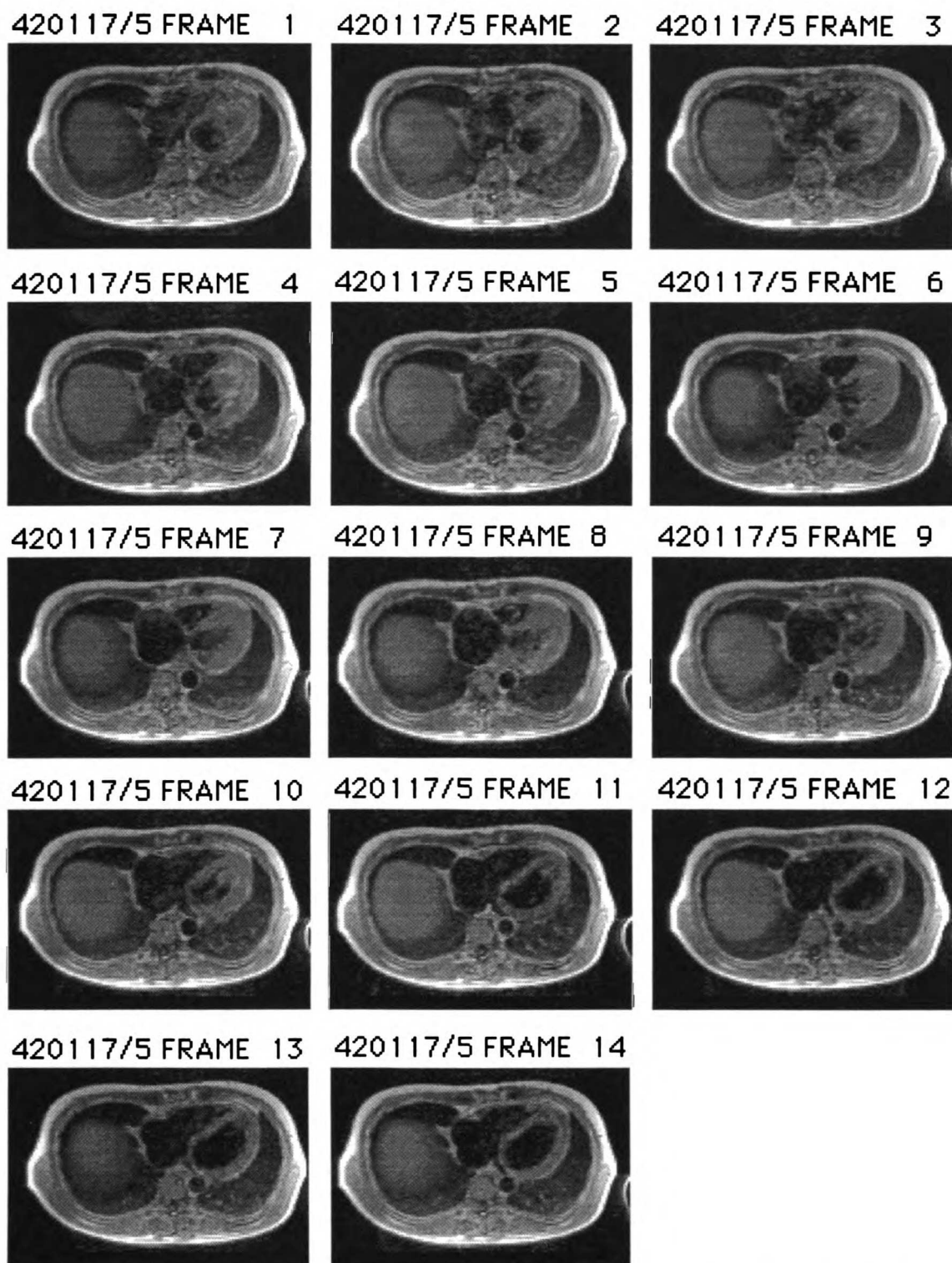


Figure 4.1 Set of cardiac MR images acquired on a Toshiba ACCESS imaging system. These images are acquired using a gated spin echo imaging technique. Only a single slice level over the cardiac cycle is shown. These images are transaxial and located midway through the left ventricle. Note that all normal image filtering has been disabled.

1107 110711

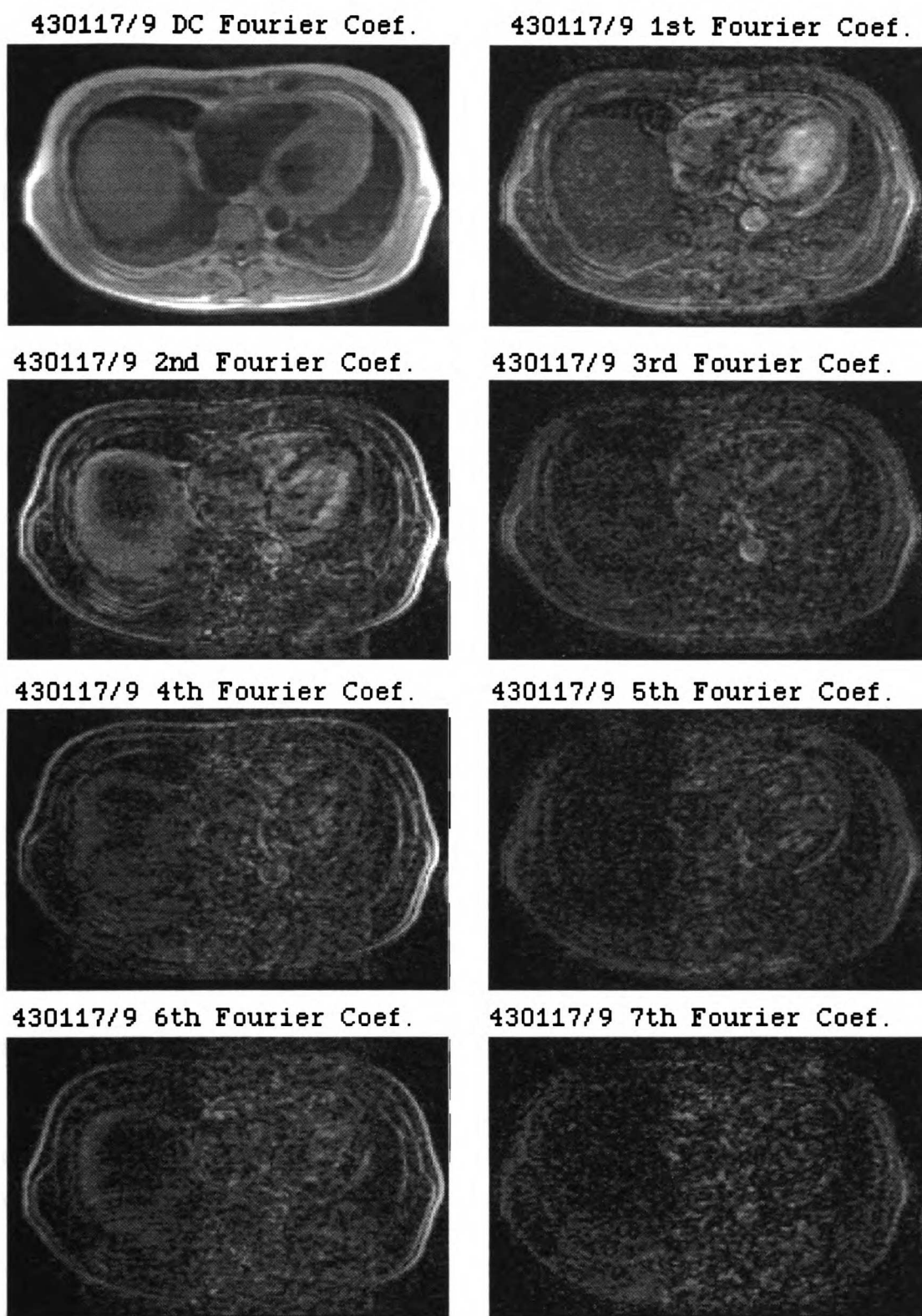


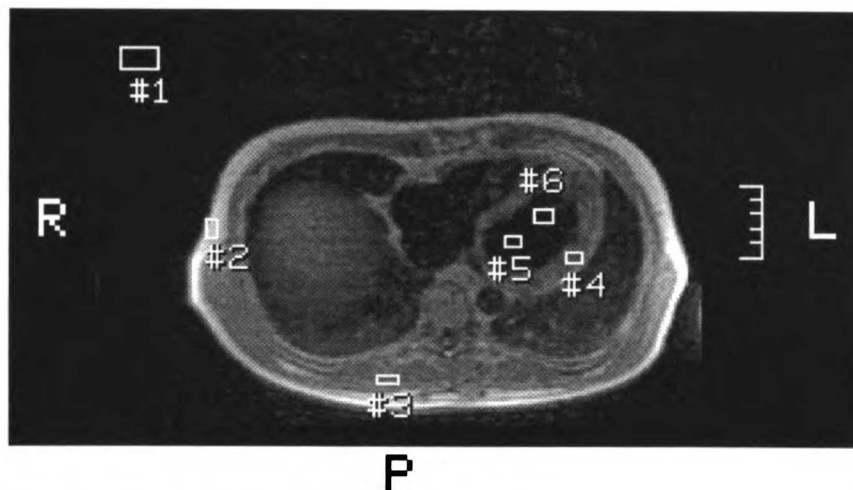
Figure 4.2 Calculated magnitude Fourier coefficient images of the Figure 4.1 images. Coefficients from DC through seven are shown. Note that the first through the seventh coefficient share the identical gray scale setting while the DC coefficient has an independently set gray scale.

1107 110101

frequency coefficients. The frequency spectrum over the entire image space can be calculated in this manner and can then be displayed one coefficient at a time by retaining the voxel position of the calculated frequency spectrums and storing the magnitude of each of the coefficient values into corresponding coefficient images. Since the voxel intensity values are real valued the resulting frequency spectrum will be a conjugate symmetric series of coefficients centered about DC. The discrete Fourier transform of the set of cardiac images shown in Figure 4.1 gives the example set of magnitude coefficient images presented in Figure 4.2. The DC and following seven coefficients are shown in Figure 4.2. The remaining six coefficients are left out of Figure 4.2 because they are just complex conjugates of the middle six coefficients. The set of coefficient images gives the temporal spectral power of the acquired cardiac images.

Examining the coefficient images in Figure 4.2 it is apparent that there is non white noise spectral power in the higher frequency coefficient images. This fact can be surmised by the appearance of ordered coefficient intensity related to the actual anatomic structure of the tissue represented in the coefficient images. The coefficient intensity values for selected voxel regions in Figure 4.2 are presented in greater detail in Figure 4.3. In Figure 4.3 the average spectral power is calculated over several indicated regions of interest (ROI) and plotted for each non DC Fourier coefficient. The ROI DC coefficient values are presented at the top of each plot. Figure 4.2 and Figure 4.3 show that, for the most part, the voxel spectral power declines in intensity after the second coefficient image to a relatively constant value.

1107 110711

420117 -15
GATED/30 5/13 A

TOSHIBA ACCESS RELEASE

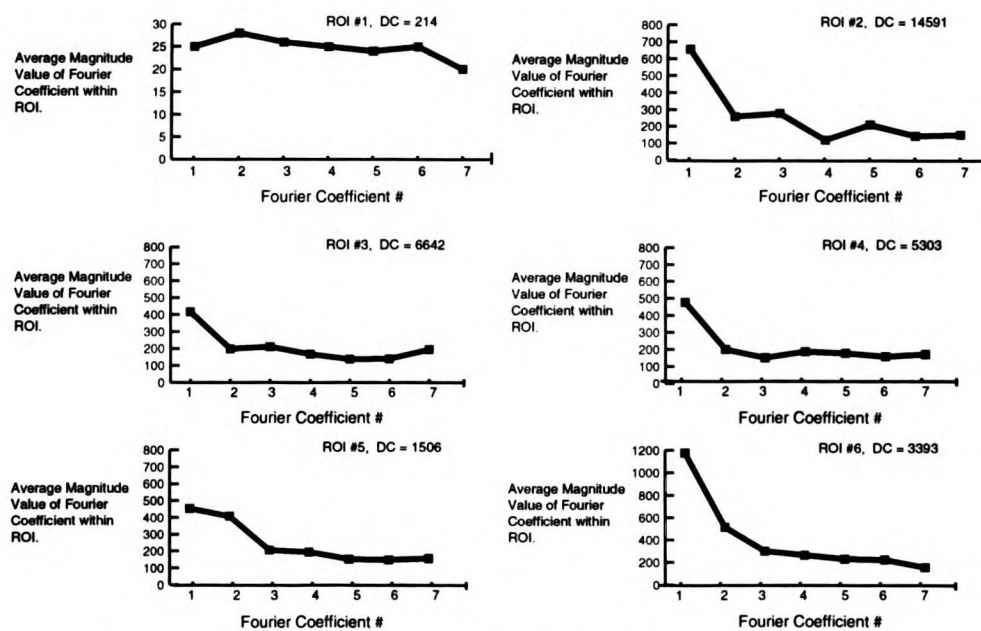


Figure 4.3 Measured coefficient intensity values for the six ROIs shown in the above image. The coefficient intensity values were measured directly from Figure 4.2. Note that the plots of ROI #1 and ROI #6 utilize a different Y axis scale then the other plots.

Static image voxels ideally should have spectral power in just the DC coefficient. Most of the static voxels (i.e. ROI #2 and ROI #3) exhibit constant spectral power consistent with the frequency spectrum of white

JULY LIBRARY

1107 1 100000

noise in the non DC Fourier coefficients above the first coefficient. In Figure 4.2 and Figure 4.3 the static voxel regions have significant spectral power in the first Fourier coefficient. Experiments with a static image phantom subjected to an automatically triggered gated cardiac spin echo MR acquisition also contain significant first Fourier coefficient spectral power (Figure 4.4). This spectral power is believed to be an artifact of the specific cardiac protocol used to produce the cardiac images. Recall from Sections 3.2 and 3.3 that the gated cardiac protocol has effectively two different TR periods. This inconsistency results in slightly different magnetization levels in the later seven temporal image slices compared to the first seven temporal image slices. The difference in the magnetization levels will result in slightly different image voxel intensities between the first half and the second half of the acquired temporal slices. It is this inconsistency in image voxel intensity which is believed to be the cause of a significant portion of the spectral power present in the first Fourier coefficient.

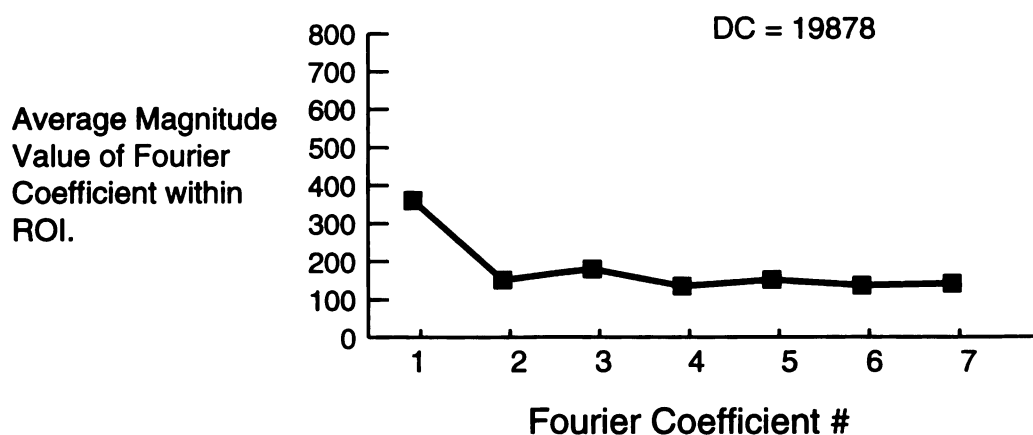


Figure 4.4 Magnitude plot of the Fourier coefficients from a static phantom imaged with a cardiac protocol. The increased magnitude of the first coefficient is due to voxel intensity variation which occurs between the first seven and the last seven acquired image frames. This occurs due to inconsistent TR values in the acquisition protocol.

1107 110711

An additional cause of undesired voxel intensity variations in static image voxels is caused by a phase encode artifact. The phase encode artifact results in increased spectral power intensity which can be observed in each of the non DC coefficient images along a vertical band containing the heart. Lastly, it is possible that magnetic field drift or patient motion may also contribute to non DC spectral power in the static image voxels of acquired cardiac images due to the voxel intensity variations that they will cause.

In the process of temporal filtering it is desired to retain the temporal voxel variation due to cardiac contraction and to eliminate the voxel variation from other sources. The intensity variation of the former temporal voxels occurs smoothly at the fundamental rate of cardiac contraction. Hence the spectral power related to this temporal voxel variation should be distributed into a narrow spectral region. In Figure 4.2 and Figure 4.3 it can be observed that there is pronounced spectral power concentrated in the first and second Fourier coefficients from voxels located in and around the cardiac chambers and the myocardium. This is the spectral power that occurs due to cardiac contraction. At higher coefficient frequencies the spectral power is unrelated to the temporal voxel variation caused by cardiac contraction. Thus the spectral power above the second coefficient can be eliminated without altering the cine representation of the heart contracting in the temporal frames. The eliminated spectral power should result in reduced stochastic noise in addition to a reduction in phase encode artifacts.

In summary, the static image voxels require only the DC coefficient to correctly specify the voxel image intensity. Where the MR signal in the

INDUSTRY

static image voxel is not exactly constant in value the DC coefficient will adequately approximate the correct static voxel intensity. Dynamic image voxels have been shown to contain the myocardial motion information in just the DC, first, and second coefficients. The DC, first, and second coefficients contain some extraneous spectral power as a consequence of the described variable TR effect, patient motion, magnetic field drift, and stochastic noise. This extra spectral power can not be separated from the essential spectral power related to cardiac contraction. Static and dynamic voxels will be treated identically in order to have a filtering process that is homogeneous over every image voxel.

The isolation of the significant image information to the DC, first, and second coefficients favors a noise reduction technique that utilizes a low pass temporal filtering process uniformly applied to each temporal image voxel (Figure 4.5). A temporal low pass filter can be accomplished by calculating the temporal voxel frequency spectrum and zeroing all but the DC, \pm first, and \pm second Fourier coefficients. The filtered frequency spectrum is then inverse Fourier transformed back into a set of complex temporal domain voxel image intensities and the magnitude is taken. These filtered voxel values are then stored at the original voxel location into a set of corresponding filtered cardiac images. Since there is some non-white noise spectral power above the second coefficient some alteration in the underlying MR signal may occur. As this discussion has indicated though, the removed spectral power is not expected to contribute significantly to the depiction of the anatomic structure in the cardiac images. Hence the resulting filtered cardiac images will correctly represent the myocardial tissue as it contracts during the cardiac cycle.

100-1-1000

This result is borne out in the application of the temporal filter later in this chapter.

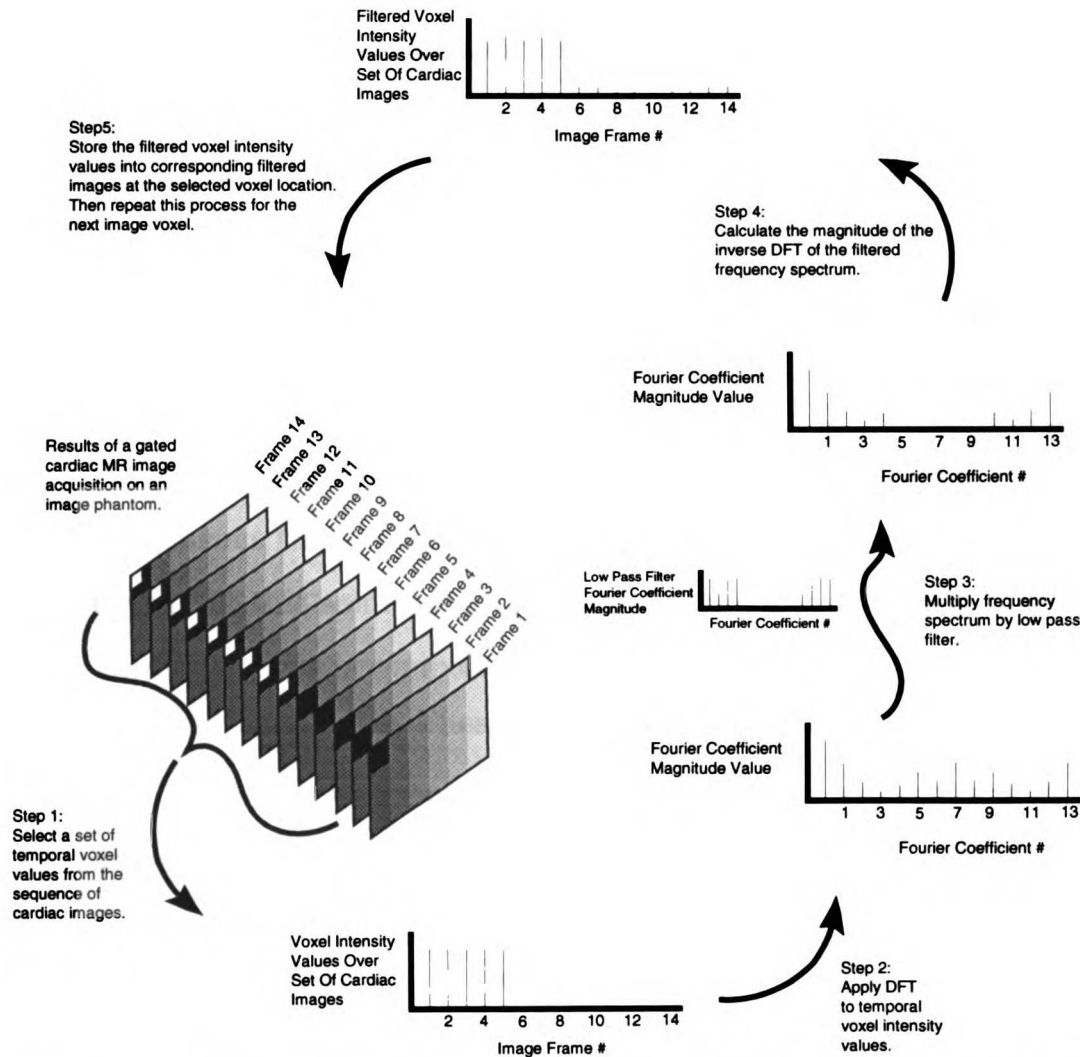


Figure 4.5 Graphic representation of the temporal filtering process described in section 4.2 and implemented throughout the rest of Chapter 4.

1107 1 100000

4.3 NOISE MEASUREMENT IN CARDIAC MAGNETIC RESONANCE IMAGES

A measure of the amount of noise in a given image is related by the image signal to noise ratio (SNR). A comparison of the SNR between a filtered image and the original image is useful for assessing the effects of the filtering process and is given by Equation 4.1:

$$R_{\text{SNR}} = \frac{\text{SNR}_{\text{filtered}}}{\text{SNR}_{\text{original}}} \quad (4.1)$$

The SNR of an image is defined to be the ratio of the mean image intensity of a homogeneous tissue region to the standard deviation of the image intensity within this same region [22]. As discussed in Section 4.2, the noise in the cardiac images is composed of two elements: stochastic noise (σ_s) and structured noise (σ_I). These two noise elements are independent of each other and hence by propagation of error [36] they will combine in quadrature:

$$\sigma_{\text{total noise}} = \sqrt{\sigma_s^2 + \sigma_I^2} \quad (4.2)$$

The stochastic noise was described in Section 4.2 to have the characteristics of white noise while the structured noise was assumed to be constant in value for a particular image voxel over the temporal image frames of the cardiac cine. The result of these properties of the image noise is that the temporal filter will reduce the stochastic noise while leaving the structured noise intact. As the stochastic noise is reduced in value it is possible that the image noise will become dominated by the structured noise term. This effect will depend upon the relative values of the structured

INCORPORATED

noise and the stochastic noise. If the structured noise dominates Equation 4.2 then further reduction in the stochastic noise through temporal filtering will not substantially reduce the noise measured in the cardiac images [38].

In some instances the structured noise may not be temporally constant, as was assumed. One such example is the structured noise that is produced by respiration. In this case it is possible that the temporal filter will attenuate this structured noise. This attenuation occurs if the structured noise has a frequency spectrum with power in the filter band of the temporal filter. Otherwise it can be assumed that the structured noise is constant as it will not be affected by the temporal filter. In the discussion that follows the structured noise is assumed to follow the characteristics of temporally constant structured noise.

The temporal filtering process proposed in the previous section of this chapter does not alter the DC coefficient of the temporal frequency spectrum. Hence the temporal filter will leave the image intensity mean value of a selected static homogeneous tissue region unchanged. As a result of this property the two image intensity means used to calculate R_{SNR} in Equation 4.1 should be equal in value. Equation 4.1 can thus be written in terms of the measured image noise which is found by calculating the image intensity standard deviation over a homogeneous tissue region:

$$R_{\text{SNR}} = \frac{\sigma_{\text{original}}}{\sigma_{\text{filtered}}} = \frac{\sqrt{\sigma_{\text{original}}^2 + \sigma_{\text{I}}^2}}{\sqrt{\sigma_{\text{filtered}}^2 + \sigma_{\text{I}}^2}} \quad (4.3)$$

Note that this measure of R_{SNR} is largely independent of the choice of tissue

1107 1101101

used in the selected image region. Equation 4.3 also depicts the quadrature nature of the image noise for a structured noise term which is unaffected by the temporal filter. The structured noise in a cardiac image can be approximated in order to analyze the effects of the temporal filter. This approximation is found by producing a temporally filtered image in which the stochastic noise has been eliminated. A measurement of the structured noise, σ_I , for a particular homogeneous tissue region of the image can then be found by calculating the image intensity standard deviation over this region.

Unfortunately it is not possible to produce a temporally filtered cardiac image where all of the stochastic noise has been removed. The best that can be accomplished by the temporal filter is to remove the stochastic noise contributed by the non DC Fourier coefficients. This filtered image (DC image) will contain unattenuated structured noise as well as an amount of stochastic noise that has been greatly reduced. It will be assumed that in practice this remaining stochastic noise is small relative to the structured noise and hence the measured noise in the DC image will be an adequate approximation of the structured noise. The stochastic noise in the unfiltered image can then be approximated from a measure of the image noise, σ_{original} , and the approximated structured noise which are applied in the solution of Equation 4.2 for the unfiltered stochastic noise, σ_{original} . The measurement of the image noise must be performed upon the same image region from which the structured noise was estimated.

In an idealized MR image there would be no structured noise present. A treatment of the improvement in SNR when such a set of cardiac

images are temporally filtered will relate the upper bound in potential SNR improvement that the temporal filter may be expected to achieve. This improvement in image SNR can be directly related to the number of temporal frequency coefficients retained after the application of the temporal filter. The frequency spectrum of the stochastic image noise will have a magnitude that is bounded by a uniform frequency spectrum for all coefficient frequencies. An upper bound expression of the improvement in SNR can thus be derived from artificial stochastic image noise that has a frequency spectrum that is uniform in magnitude. This expression can be found through an examination of the effects of the temporal filter upon the standard deviation (Equation 4.4) of the temporal intensities of a particular image voxel:

$$\sigma_s = \left[\sum_{i=1}^N \frac{(S_i - \bar{S})^2}{N-1} \right]^{\frac{1}{2}} \quad (4.4)$$

In Equation 4.4 N is the number of temporal image voxels and σ_s signifies that this equation is a measure of the stochastic image noise only. The image intensity of the i th voxel in this series of temporal image frames, S_i , can be expressed as the sum of the tissue MR signal, m_i , and the stochastic image noise, n_i . To simplify matters it is assumed that the selected tissue is static and hence the MR signal has a constant value, M_0 . Since the stochastic image noise has a zero mean the mean image intensity, \bar{S} , will be equal to M_0 and Equation 4.4 becomes:

$$\sigma_s = \left[\sum_{i=1}^N \frac{n_i^2}{N-1} \right]^{\frac{1}{2}} \quad (4.5)$$

Using Parseval's equation [34] the standard deviation representation of the image noise (Equation 4.5) can be modified to include the effects of the temporal filter. A discrete version of Parseval's equation can be written as follows [37]:

$$\sum_{i=1}^N |x_i|^2 = \frac{1}{N} \sum_{k=1}^N |X_k|^2 \quad (4.6)$$

In Equation 4.6, x_i is the temporal function value over the N samples and X_k is the Fourier coefficient value over the N frequency steps. The assumed stochastic image noise can be expressed as: $|X_k| = A$, for all Fourier coefficients k and an arbitrary constant A . Using this expression Equation 4.6 can be combined with Equation 4.5 to yield the following expression which represents the upper bound of the stochastic image noise in an unfiltered image:

$$\sigma_{s_{\text{original}}} = \left[\frac{N A^2}{N(N-1)} \right]^{\frac{1}{2}} \quad (4.7)$$

In the temporal filtering process a specified number of the higher frequency Fourier coefficients will be eliminated from the Fourier transformed temporal voxel intensities. This filtering process can be expressed through a modification in Equation 4.7 where N in the

numerator is substituted with z where z is equal to the number of Fourier frequency coefficients retained after the application of the temporal filter. The effects of the temporal filter on the stochastic image noise can then be represented by relating the stochastic noise in the filtered images to the stochastic noise in the original image as shown in Equation 4.8:

$$\sigma_{\text{filtered}} = \left[\frac{z}{N} \right]^{\frac{1}{2}} \sigma_{\text{original}} \quad (4.8)$$

Equation 4.8 can be applied to Equation 4.3 to produce an upper bound expression of the effects of the temporal filter upon cardiac images that do have structured noise as follows:

$$R_{\text{SNR}} = \frac{\sigma_{\text{original}}}{\sigma_{\text{filtered}}} = \frac{\sqrt{\sigma_{\text{original}}^2 + \sigma_{\text{I}}^2}}{\sqrt{\left[\frac{z}{N} \right] \sigma_{\text{original}}^2 + \sigma_{\text{I}}^2}} \quad (4.9)$$

In the following section the structured noise and the unfiltered stochastic noise are found for a temporal image phantom. These values can then be applied in Equation 4.9 to show the theoretical upper bound of the reduction in noise which occurs from the application of the temporal filter to these images. Equation 4.9 can be extended to actual cardiac images. However, the value of σ_{I} will have to be recalculated for each selected tissue region where the improvement in SNR is to be studied. The above discussion focused upon static cardiac tissue. In the case of dynamic image voxels, Equation 4.9 can also be applied if the tissue MR signal's spectral power remains in the passband of the temporal filter and σ_{I} can be determined from the DC image.

Care must be taken when defining homogeneous tissue regions for the measurement of image noise as several difficulties may arise. First, if the selected region is not truly homogeneous then both the mean value and the standard deviation of the region's image intensity will be distorted by this inhomogeneity and the measured SNR will be incorrect. Definition of the noise measurement region to include only homogenous tissue will avoid this problem. If the noise measurement region is selected to utilize a tissue where the MR signal is not significantly larger than the noise, then it is possible that in this region the noise will become Rayleigh distributed. If this occurs the meaning of the measured SNR will again be disrupted. Hence it is best when measuring SNR to avoid using regions with small MR signal values.

Image reconstruction presents an additional issue as it may result in an artifact of intensity variation in areas near a sharp transition in image intensity [35]. In order to avoid this difficulty the noise measurement region's border should be defined well within a homogeneous region of tissue, away from transitions in signal intensity. MR image reconstruction often subjects the processed images to a variety of image filtering schemes. To insure that unexpected variations in SNR measurement do not occur it is thus required to take into account the effects of the image filtering operations when making SNR measurements. Another approach to solving this problem is to simply disable the reconstruction image filters. This will produce a base line image upon which the new image filtering scheme can be applied and evaluated.

4.4 PRACTICAL APPLICATION OF THE TEMPORAL FILTERING ALGORITHM

The temporal filter described in this chapter will now be applied to an actual set of images produced by a gated cardiac MR acquisition. The theoretical upper bound for the improvement in SNR due to the temporal filter is given by Equation 4.9 with σ_1 set to zero. This theoretical improvement is illustrated in Figure 4.6 below for $N = 14$. The temporal filter (Figure 4.5) is applied to the temporal image frames of the cardiac cine one voxel at a time by selecting the temporal image voxel values and transforming them into their frequency spectrum using the discrete Fourier transform (DFT) [37]. The slower DFT is used instead of the Fast Fourier transform (FFT) because only fourteen temporal data points are available. The frequency coefficients of the specified attenuation band are set to zero and the resulting frequency spectrum is then transformed back

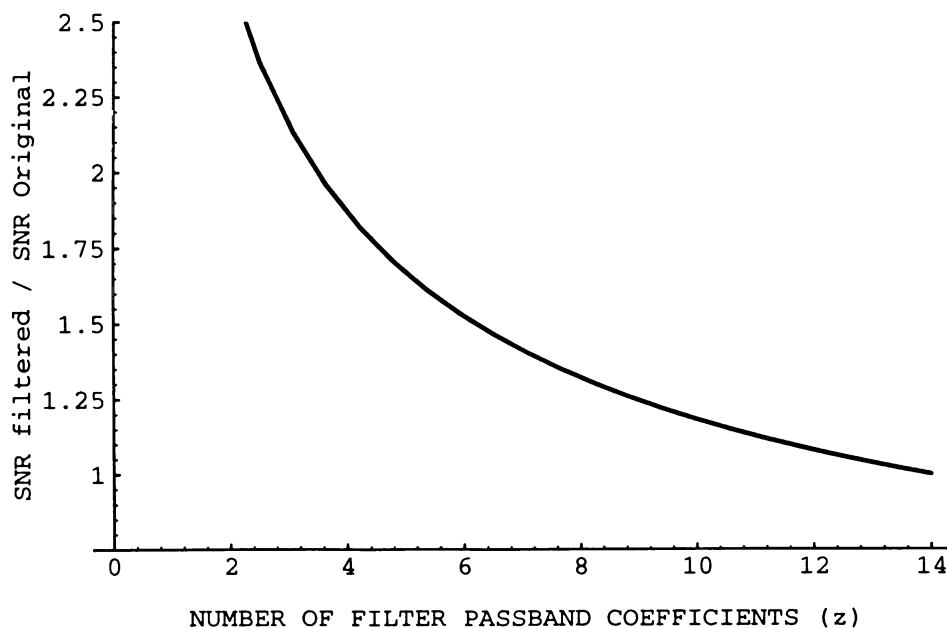


Figure 4.6 The theoretical R_{SNR} from Equation 4.9 for the ideal case of no structured noise present in the image ($\sigma_1 = 0$) and $N = 14$.

into the temporal domain using the inverse DFT. The magnitude of this complex result is then calculated and the resulting voxel values are stored in the corresponding filtered images. This process is repeated for each voxel in the image space.

An evaluation of the temporal filter's improvement in SNR can best be performed upon a homogeneous static phantom (i.e. a stationary baby oil filled cube, imaged with a body coil). This object is selected as the imaging subject because it will be free of any motion induced effects and will have a homogeneous MR signal over a relatively large volume. The static phantom images are produced on a Toshiba Access MR imager using the conventional spin echo gated cardiac protocol discussed in Section 3.2. The gated cardiac acquisition requires the use of an artificial ECG source to gate the imaging protocol. The standard image filtering algorithms are disabled during image reconstruction so that a base line image is produced where the image noise is unattenuated by post acquisition filtering. The gated cardiac protocol produces fourteen images per slice position. These images of the static phantom are identical except for noise and the TR effect shown in Figure 4.4.

The improvement in SNR from the application of the temporal filter can be measured using the procedure described for Equation 4.3. Following this procedure the improvement in SNR is found by taking the ratio of the noise from the unfiltered image to the noise from the filtered image over a homogeneous region in the phantom. The image noise is estimated by calculating the image intensity standard deviation in this region for each of the temporal image frames and averaging this value. This procedure is

JULY 1981

repeated for each possible filter passband as described by the parameter z , the number of Fourier coefficient values retained by the temporal filtering process. The measured improvement in SNR, R_{SNR} , for the temporally filtered static phantom is presented in the right hand column of Table 4.1 for the possible filter passbands.

z number of remaining frequency coefficients	Theoretical R_{SNR}	Measured R_{SNR}
3	1.5390	1.6361
5	1.3772	1.4103
7	1.2576	1.2743
9	1.1645	1.1758
11	1.0895	1.0958
13	1.0274	1.0303
14	1.0000	1.0000

Table 4.1 Theoretical R_{SNR} from Equation 4.9 for the measured values of $\sigma_{\text{original}} = 342$ and $\sigma_1 = 205$ from a static temporal phantom and the measured R_{SNR} from this same temporal phantom.

The measured improvement in SNR can be compared to the theoretical estimate of the improvement in SNR given by Equation 4.9. To apply Equation 4.9 it is necessary to estimate the structured noise, σ_1 , and the unfiltered stochastic noise, σ_{original} . As previously described the structured noise for a particular homogeneous region is estimated by the DC image noise of this region. The structured image noise for a selected homogeneous region in the temporal image phantom was estimated to be: $\sigma_1 = 205$. The stochastic noise can then be estimated from the region's structured noise and unfiltered image noise using Equation 4.2. In the temporal phantom the image noise was calculated from the average unfiltered image noise of each temporal frame. It is estimated to be: $\sigma_{\text{original}} = 398$. The middle column of Table 4.1 thus lists the theoretical

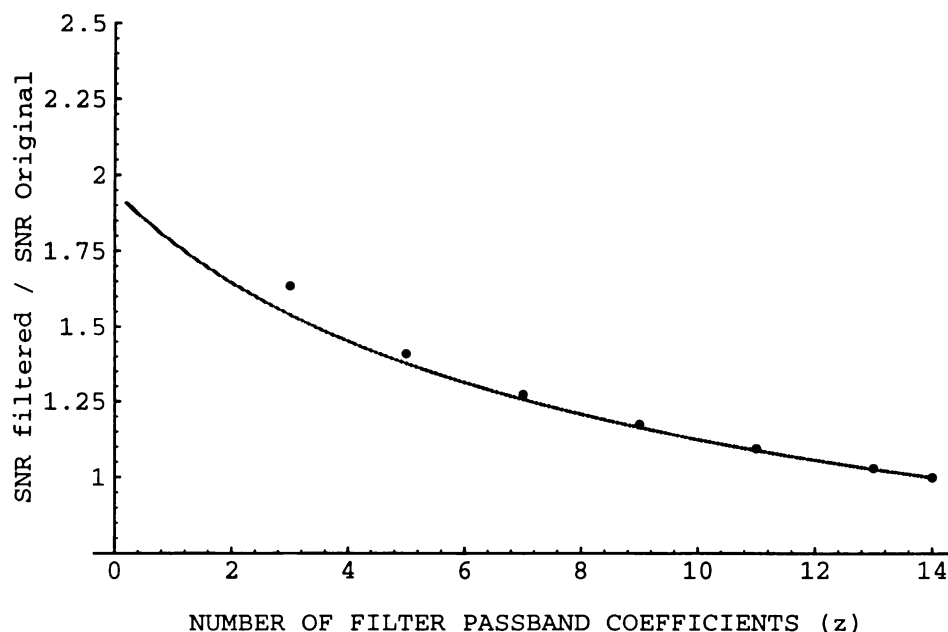


Figure 4.7 Theoretical R_{SNR} from Equation 4.9 for the measured values of $\sigma_{original} = 342$ and $\sigma_1 = 205$ is plotted as a solid line and the measured R_{SNR} from this same temporal phantom is indicated by the data points.

improvement in the SNR for the selected homogeneous region. A plot of the numeric values from Table 4.1 is presented in Figure 4.7 where the theoretical improvement in SNR is drawn with a curve and the measured improvement in SNR is indicated by the drawn points. The theoretical and the measured R_{SNR} correspond well with each other for most of the possible passbands of the temporal filter. It is likely that an even better match between the computed theoretical values and the measured values in Table 4.1 would occur if it were possible to produce a more accurate measure of σ_1 . Notice also that the curve from Figure 4.7 represents a significant reduction from the idealized improvement in SNR presented in Figure 4.6. This is a direct result of the effects of the structured noise which was assumed to be zero in Figure 4.6. The temporal filter does not address the structured noise and hence the measured improvement in SNR

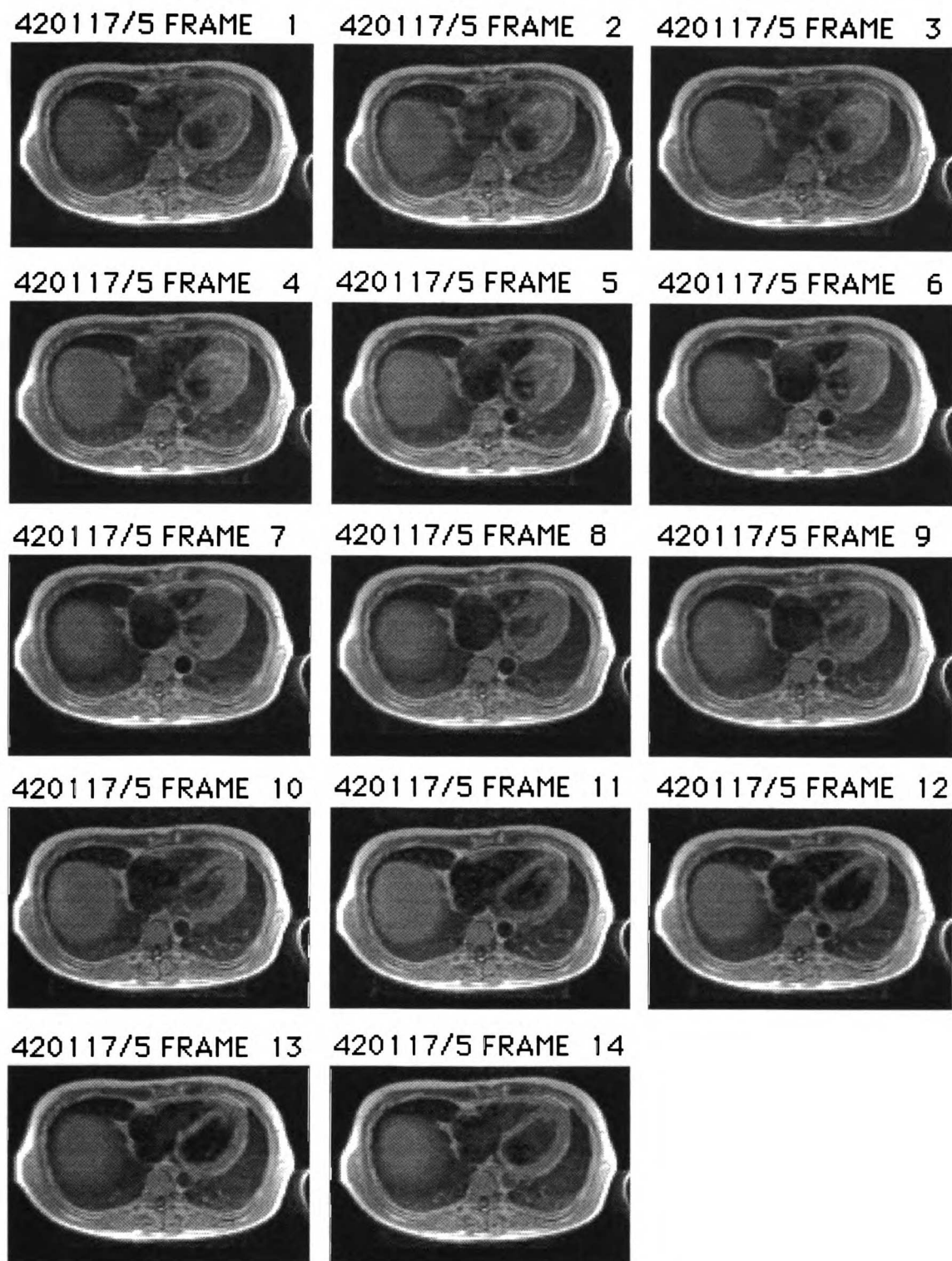
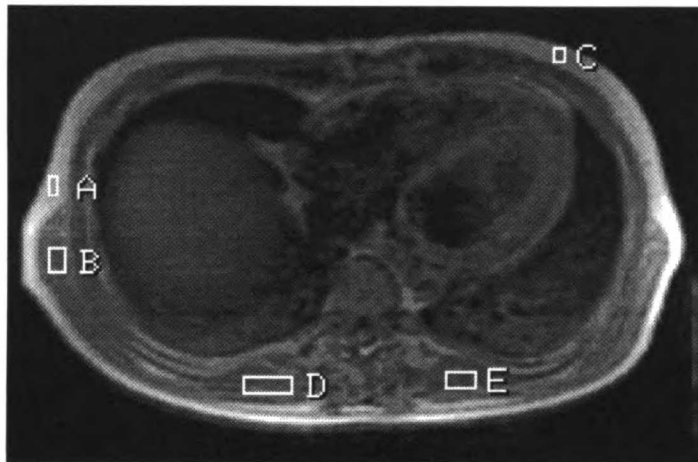


Figure 4.8 The result of a temporal filter with $z = 5$ applied to the cardiac images from Figure 4.1.

produced by the temporal filter will be limited by the structured noise present in the acquired images.

The next step in the evaluation of the temporal filter is to apply it to the cardiac acquisition presented in Figure 4.1. As discussed in Section 4.2 the optimum low pass cardiac temporal filter will retain the DC, \pm first, and \pm second Fourier coefficients represented by $z = 5$. The

420117/5 FRAME 1



ROI Identification Symbol	Number Of Voxels In ROI	Average Measured R_{SNR} In ROI For Cardiac Images in Fig 4.8	Standard Deviation Of The R_{SNR} Measurements
A	16	1.320	0.409
B	44	1.183	0.159
C	18	1.566	0.376
D	77	1.192	0.142
E	56	1.317	0.220

Figure 4.9 The table in this figure shows the average R_{SNR} measured for a static tissue and averaged over each of the images in the cardiac sequence. Care was taken to insure that the selected tissue voxels were static and represented the same tissue in each image. The standard deviation of the R_{SNR} measure is also provided to give an estimate of the variation of the improvement in SNR in the cardiac images. The location of these ROIs can be observed in the included cardiac image. The temporal filter applied to these images had $z = 5$ which implies a theoretical upper bound in $R_{SNR} = 1.673$.

resulting filtered images are shown in Figure 4.8. The measured R_{SNR} for a few static tissue regions is shown in Figure 4.9. These measured values are consistent with the ideal R_{SNR} for a temporal filter with $z = 5$ given by Figure 4.6. Examining the images of Figure 4.8 from a qualitative point of view it is observed that the temporal filter produces a noticeable smoothing of the cardiac images. It can also be observed that the phase encoding artifact discussed earlier is noticeably reduced. At the same time there does not appear to be any reduction in the clarity of the anatomic structure in the images or the delineation of the myocardial tissue borders. In fact when viewed as a cine loop there appears to be a reduction in the noise surrounding the myocardial tissue borders which enhances the ability to visualize these borders. Overall the temporal filter produces a noticeable improvement in the cardiac images resulting from the reduction in image noise.

The motivation for applying the temporal filter was to reduce the uncertainty with which MR signals are observed in the cardiac images and thus refine image appearance. This goal has been achieved along with an additional benefit of improving the temporal appearance of the cardiac images as viewed in a cine presentation. The temporal filtering analysis presented in this chapter has also provided insight into how the information present in the cardiac images is organized and how the SNR is measured. With this understanding and benefit in SNR improvement the quantitative analysis of cardiac function presented in Chapters 6, 7, and 8 will be enhanced. The temporal filtering approach presented in this chapter can also be applied to the other cardiac imaging modalities (Chapter 2) resulting in an overall benefit for cardiology in general.

CHAPTER 5

OBLIQUE REFORMATTING OF CARDIAC MAGNETIC RESONANCE IMAGES

5.1 INTRODUCTION

The cine cardiac MR imaging technique described in Chapter 3 produces a series of tomographic images with a common perpendicular slice axis. These sequential multi-slice images are spatially positioned with an incremental offset along the slice axis. MR imaging devices were originally restricted to acquiring tomographic images along slice axes that were parallel to the coordinate axes of the MR imager's gradient coil set. Patients were placed into these MR imagers in a manner which aligned their body's coordinate reference frame with that of the MR imager. The resulting acquired MR images were thus oriented along the familiar transaxial, sagittal, or coronal tomographic image planes. MR imaging devices are now available with enhanced slice selection technology that allows the acquired slice axis to be oriented in an arbitrary direction. These image slices, acquired along a coordinate reference frame independent of the MR imager's reference frame, are referred to as oblique image slices.

The acquisition of oblique image slices is advantageous because the body's internal organs are not always aligned along the external body's coordinate reference frame. Thus oblique imaging methods are used to generate tomographic image slices that are oriented along the selected anatomic structure's long or short axis. It is often the case that these oblique image orientations facilitate the measurement of linear dimensions

and the comparison of similar tissue from a selected anatomic structure. This is certainly the case for oblique cardiac images that are oriented along the long and the short axes of the heart. Long axis cardiac images enable the measurement of the cardiac chamber lengths from a single tomographic image. Cardiac images that are acquired along the body's coronal or sagittal image planes on the other hand may contain a foreshortened representation of the cardiac chambers. In order to measure the cardiac chamber lengths in these images an increased amount of effort is required. Short axis cardiac images are often utilized to examine the state of the myocardial tissue. This analysis is performed by comparing the myocardial tissue based upon symmetry and tissue similarity. When short axis cardiac images are used in this manner the tomographic cross-section will contain myocardial tissue that is largely from the same region of the heart as judged by the slice position along the cardiac long axis. This tissue, when healthy, should have relatively consistent wall thickness and wall motion characteristics. If this analysis were to be performed upon images acquired along the body's transaxial slice axis it is expected that the myocardial cross-section would no longer contain tissue from the same cardiac region with respect to the cardiac long axis. Hence the transaxial image would be unsuitable for relative comparison of the myocardial wall thickness or the myocardial wall motion.

Oblique imaging methods can also be used to establish a basis for the comparison of quantitative tissue parameters measured using different tomographic imaging modalities. In order to properly make this comparison, oblique imaging methods are used to acquire images along the same slice axis in both imaging modalities. This will prevent unequal

JULY LIBRARY

foreshortening of the linear dimensions measured for the quantitative analysis. Quantitative measurements may also require the definition of anatomic areas with boundaries that are identified by the presence of specific anatomic landmarks [12]. As long as the image slices are oriented along the same slice axis the physical cues provided by these anatomic landmarks will provide a consistent indication of the extent of the selected image area. In the next chapters oblique cardiac imaging methods will be utilized to align the acquired cardiac MR image slices along the long and short axes of the heart. This will insure a correct comparison of left ventricular volumetric parameters measured from cardiac MR images to those measured from echocardiographic images.

With the importance of oblique image slices revealed it should be noted that there are two methods from which oblique image slices can be produced. The first of these methods, which has already been introduced, is the actual acquisition of image slices along an oblique slice axis. It may not be possible to acquire images obliquely or the oblique images may require a refinement of the slice orientation. When this is the case the second oblique imaging method can be applied, the method of retrospectively reformatting the acquired image slices along an oblique slice axis. The process of retrospective oblique reformatting is the subject of the remaining portion of this chapter. This method will be used throughout Chapters 6, 7, and 8 to obliquely reformat the acquired cardiac MR images. This is required because the cardiac images produced for this dissertation by the Toshiba Access MR Imager could only be acquired along slice axes that were parallel to the standard tomographic image planes.

INDEX

5.2 THE METHOD OF RETROSPECTIVE OBLIQUE REFORMATTING OF TOMOGRAPHIC IMAGES

Retrospective oblique reformatting is a computational process where a set of multi-slice tomographic images are resliced along an arbitrary slice axis after the actual image acquisition has been completed. The oblique reformatting process can be succinctly described as a transformation of image coordinates from an oblique reference frame to a reference frame aligned along the original tomographic axis of the acquired images. This coordinate transformation maps voxel locations from the oblique image slice into voxel locations in the original tomographic image data thereby determining the oblique voxel image intensity. An oblique image is created by repeating this process for each oblique voxel contained in the selected image slice. This method can be expanded to include the production of multi-slice oblique images by iteratively calculating oblique slices with an incremental slice offset along the oblique axis. The shifted oblique slice's voxel intensities are computed with no extra effort since the coordinate transformation maps three dimensional voxel coordinates from the oblique reference frame to the original tomographic reference frame. The entire reformatting process is carried out using a digital computer to perform the described mathematical operations, data storage and image display.

The coordinate transformation discussed above is implemented by establishing separate reference frames for both the original tomographic axis and the arbitrary oblique slice axis. These reference frames are specified by a Cartesian coordinate system where the X and Y axes are directed along the horizontal and vertical slice dimensions respectively and

INC 100000

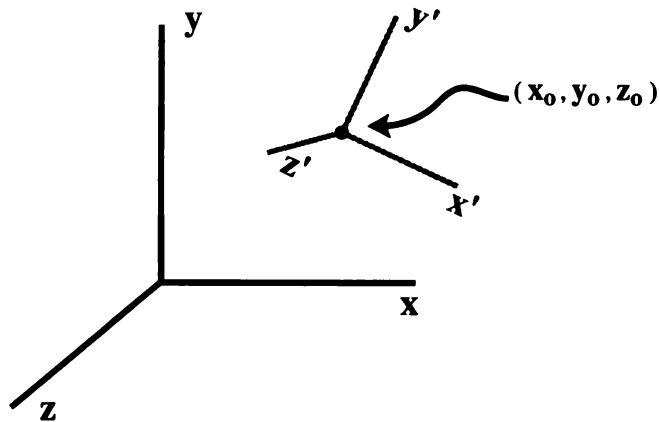


Figure 5.1 Original and oblique coordinate axes reference frames.

the Z axis is directed along the slice perpendicular. The Cartesian axes belonging to the original tomographic image slice's reference frame are labeled x, y, z and the oblique slice's Cartesian coordinate axes are labeled x', y', z' (Figure 5.1). Note that the Cartesian coordinate axes of the original tomographic images are generalized and do not necessarily correspond to the coordinate axes of the MR imaging device.

These two coordinate reference frames are related to each other by their direction cosines [40]. The direction cosines: l, m, n, are the numeric

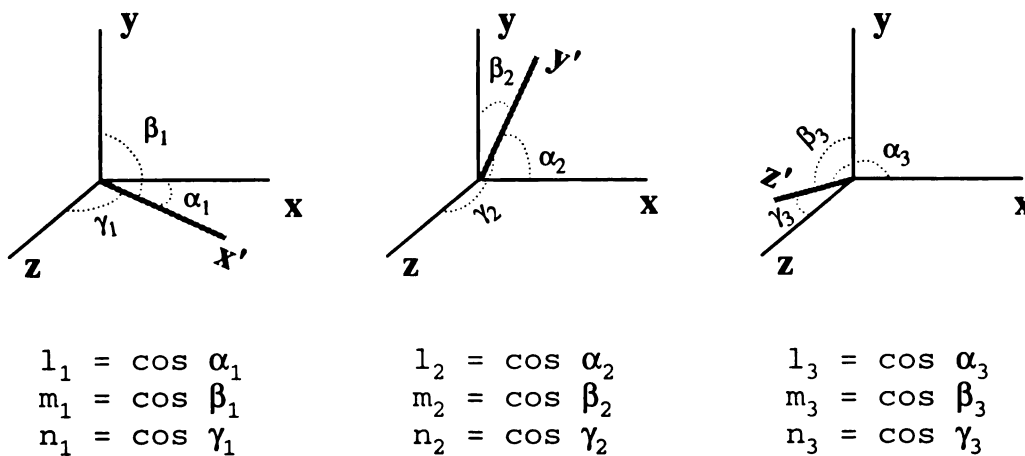


Figure 5.2 Direction cosines l, m, n for the three oblique coordinate axes with respect to the original tomographic coordinate reference frame.

INC 1000000

values found by calculating the cosines of the angles that a vector makes with respect to the three Cartesian coordinate axes: x , y , z . The coordinate transformation between the oblique and the original coordinate reference frames is calculated using the direction cosines of each of the oblique coordinate axes: x' , y' , z' . Figure 5.2 depicts how these direction cosines are defined and the notation used throughout this chapter to identify them.

The reference frame coordinate transformation that is utilized in the retrospective oblique reformatting method is written in vector notation as shown in Equation 5.1 [41]. Both the oblique coordinate axes' direction cosines and the oblique coordinate reference frame origin, x_0 , y_0 , z_0 , are used in this coordinate transformation. The location of this origin is defined to lie at the intersection of the center oblique slice and the oblique slice's normal vector after it has been spatially translated to also intersect the origin of the original coordinate reference frame. The x_0 , y_0 , and z_0 coordinate locations are determined with respect to the original coordinate reference frame. To apply Equation 5.1 the voxel indices of the oblique slice are converted into oblique spatial locations using the selected spatial dimensions of the oblique image voxels with reference to the oblique Cartesian coordinate origin. The coordinate transformation maps the oblique voxel's spatial location in the oblique reference frame to an

$$\begin{bmatrix} x \\ y \\ z \end{bmatrix} = \begin{bmatrix} l_1 & l_2 & l_3 \\ m_1 & m_2 & m_3 \\ n_1 & n_2 & n_3 \end{bmatrix} \begin{bmatrix} x' \\ y' \\ z' \end{bmatrix} + \begin{bmatrix} x_0 \\ y_0 \\ z_0 \end{bmatrix} \quad (5.1)$$

INDIAN

equivalent spatial location in the original tomographic reference frame. The spatial dimensions of the original tomographic image voxels are then utilized to determine the voxel indices in the original tomographic data of a set of voxels that are neighbors of the transformed oblique image voxel. The voxel intensities of these voxels are then interpolated, with appropriate weighting, to produce the transformed oblique voxel's intensity value.

The direction cosines of all three oblique Cartesian coordinate axes were utilized in Equation 5.1 to accomplish the coordinate transformation. The oblique slice plane though is specified by the oblique slice normal and the spatial offset along this normal of the oblique slice relative to the oblique reference frame origin. Hence it is desirable to simplify Equation 5.1 such that it is written in terms of only the direction cosines of the oblique slice normal, z' , and the coordinates of the oblique reference frame origin. To accomplish this task it is assumed that the x' axis lies in a plane parallel to the x - y slice plane of the original tomographic reference frame (i.e. z is equal to a constant value everywhere on the x' axis). The significance of this assumption is that the x' axis will be perpendicular to the z axis and thus n_1 (Figure 5.2) will equal zero. The three sets of direction cosines given in Figure 5.2 are actually the components of the normal vector for the respective oblique coordinate axes [40]. Thus, for the x' axis and z' axis, the following two equations can be written and then solved for l_1 and m_1 :

$$\begin{bmatrix} l_1 & m_1 & n_1 \end{bmatrix} \cdot \begin{bmatrix} l_3 & m_3 & n_3 \end{bmatrix} = 0 \quad (5.2a)$$

$$l_1^2 + m_1^2 + n_1^2 = 1 \quad (5.2b)$$

JULI LINDHALL

MEMPHIS
TENN
4/4/68

The direction cosines of the x' axis are thus given in terms of l_3 and m_3 .

The next step in the simplification of the coordinate transformation is to derive the direction cosines of the y' axis in terms of l_3 , m_3 , and n_3 . This is accomplished by taking the vector cross product of the z' normal vector and x' normal vector that has just been written in terms of the z' axis' direction cosines. Thus Equation 5.1 can be written in terms of the direction cosines of the z' oblique slice normal as follows:

$$\begin{bmatrix} x \\ y \\ z \end{bmatrix} = \begin{bmatrix} \frac{m_3}{\sqrt{m_3^2 + l_3^2}} & \frac{l_3 n_3}{\sqrt{m_3^2 + l_3^2}} & l_3 \\ \frac{-l_3}{\sqrt{m_3^2 + l_3^2}} & \frac{m_3 n_3}{\sqrt{m_3^2 + l_3^2}} & m_3 \\ 0 & -\sqrt{m_3^2 + l_3^2} & n_3 \end{bmatrix} \begin{bmatrix} x' \\ y' \\ z' \end{bmatrix} + \begin{bmatrix} x_0 \\ y_0 \\ z_0 \end{bmatrix} \quad (5.3)$$

Equation 5.3 expresses the generic form of the coordinate transformation utilized in the retrospective oblique reformatting method. To utilize this equation it is necessary to specify the direction cosines of the oblique slice axis and the spatial location of the oblique slice center. One method for accomplishing this task is to select three spatial points in the tomographic image data that are contained within the desired oblique image slice. The oblique slice axis, and hence the z' axis' direction cosines, can be easily determined from these points as well as the oblique slice center. This method of specifying the oblique slice axes works very well when there are specific spatial points that obviously fall within the desired

oblique image slice. In practice though there are situations, such as the definition of the cardiac long and short axes, where it is difficult to identify these spatial points.

In these cases the oblique slice orientation can be specified by the direct manipulation of the oblique slice axis' direction cosines and the slice offset which are selected by an operator with a four axis digital input device. In order to visualize the orientation and the location of the oblique slice defined by these slice selection parameters it is necessary to develop a three dimensional representation of the selected oblique slice. This can be accomplished by generating two oblique images that are orthogonal to the original tomographic slice axis and that are also orthogonal to each other. The oblique axes for these two orthogonal images are directed along the X and Y axes of the original tomographic reference frame respectively. The direction cosines of the z' axis for these two orthogonal images are therefore $(l_3, m_3, n_3) = (1, 0, 0)$ for the vertical orthogonal and $(l_3, m_3, n_3) = (0, 1, 0)$ for the horizontal orthogonal reformatted images. The slice offsets are selected so as to produce reformatted orthogonal images that span the projected oblique reference frame's origin. The retrospective oblique reformatting method discussed above can then be applied to produce the two reformatted orthogonal images. The complete set of orthogonal images also includes a third image oriented along the original tomographic image plane located at the oblique axis origin.

The three dimensional representation of the selected oblique slice can then be displayed by indicating the intersection of this oblique slice with the three orthogonal images. This is done by drawing a line in each orthogonal

1951

image at the intersection of the oblique slice and the particular orthogonal image. An example of this technique of oblique slice selection is depicted in Figure 5.3. Figure 5.3d is an original tomographic image acquired along

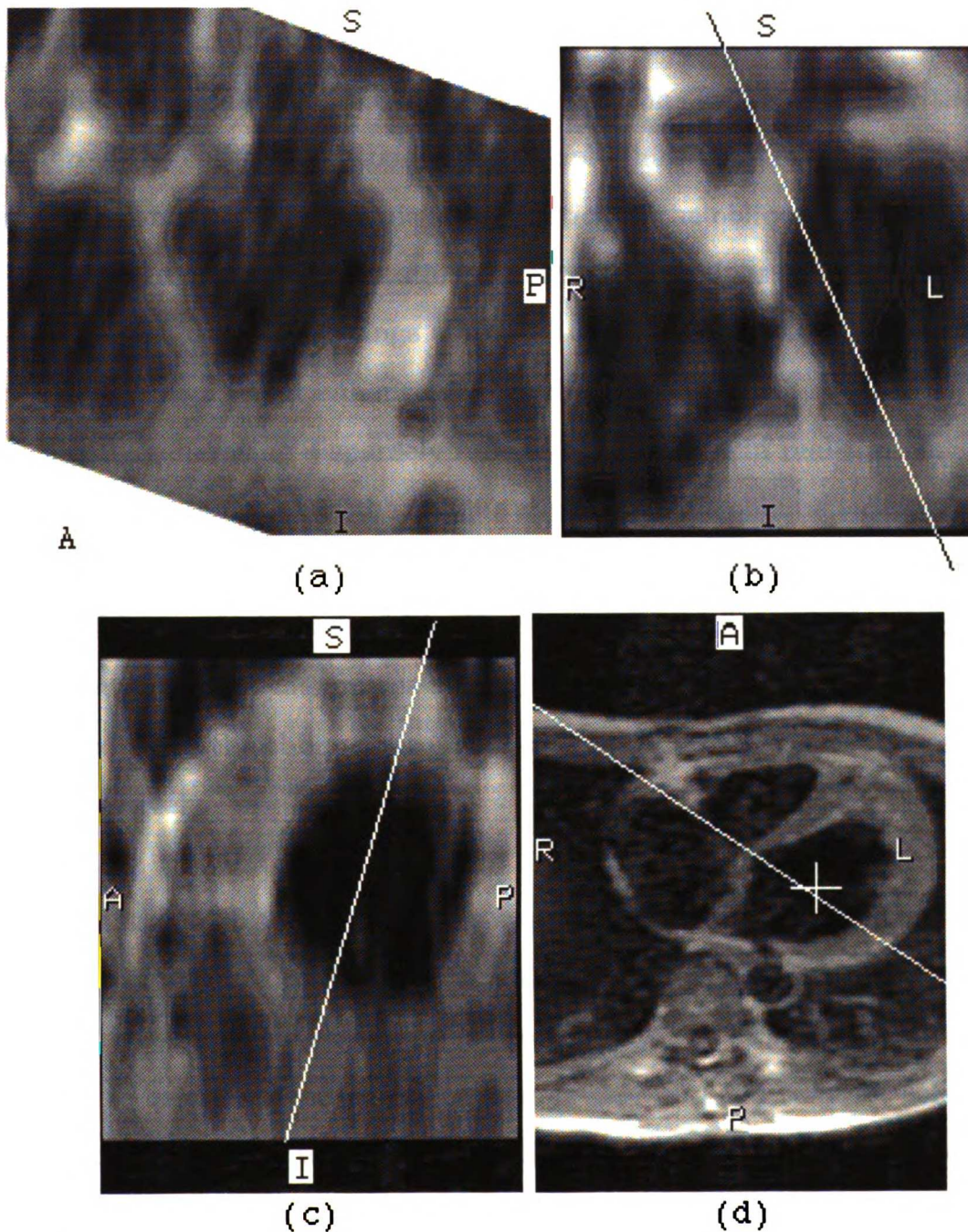


Figure 5.3 Example of a three dimensional oblique slice display. (a) obliquely reformatted image, (b) and (c) reformatted orthogonal oblique locator images, (d) original tomographic image.

1951

the standard transaxial slice axis. Figures 5.3b and 5.3c are orthogonal images constructed from the original transaxial images using the retrospective oblique reformatting methods presented in this chapter. The white lines in these images indicate the oblique slice intersection with the orthogonal images. The oblique image specified by these intersection lines has been calculated and is displayed in Figure 5.3a. The interface for the selection of the oblique slice axis should couple this visual oblique slice representation with the dynamic manipulation of the oblique slice selection parameters. In this implementation the intersection lines will shift in response to the dynamic settings of the oblique slice's direction cosines and slice offset. A significant enhancement of this method is achieved by dynamically generating a sparsely refined oblique slice in real-time in response to reorientation of the oblique slice axis. This oblique locator image provides a rough preview of the selected oblique slice. The oblique locator image will be particularly useful in Chapters 6, 7, and 8 to select the oblique slice orientation that maximizes or minimizes the cardiac chamber area as is required when the oblique slice is aligned along the cardiac long or short axes respectively.

Equation 5.2b shows that there are really only two independent direction cosines for a particular oblique axis orientation. However selecting the oblique slice orientation directly with the direction cosines turns out to be a rather unwieldy technique. Another approach for selecting the oblique slice axis is to redefine the direction cosines in terms of two intuitive angles: the angle of tilt that separates the z' axis from the z axis, and the angle of rotation of the z' axis about the z axis. Figure 5.4 illustrates how these two angles are used to define the direction cosines of the z' axis.

INDIAN

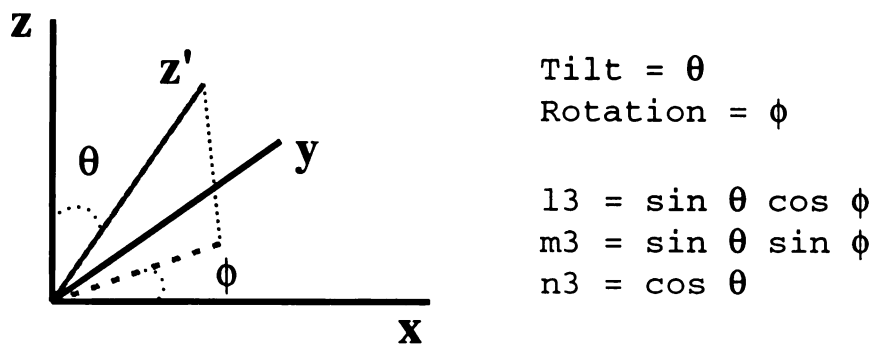


Figure 5.4 Simplified direction cosine definition based upon tilt and rotation angles of z' axis about the z axis.

This technique reduces the oblique slice specification parameters to only three separate values: two orientation angles and a slice offset. The oblique image is then produced by substituting the direction cosines equations from Figure 5.4 into Equation 5.3 along with the selected slice offset.

The oblique images produced by the coordinate transformation method described in this section are limited by the voxel resolution of the original tomographic images. The most common reason for this limitation is that tomographic image voxels are often not isotropic. In this case the largest voxel dimension is usually directed along the slice axis. Hence as the oblique slice axis is oriented away from the original tomographic slice axis the oblique voxel resolution becomes reduced as compared to the original tomographic image voxels. The coarsest oblique voxel resolution occurs when the oblique slice axis is aligned perpendicular to the original tomographic slice axis.

The reformatted oblique images are further limited by the extent of the original tomographic imaging volume. This is a function of the number

JUNI LUDWIG

of original tomographic image slices and the slice thickness. The oblique voxel resolution, as just indicated, is directly related to the original tomographic image slice thickness in that thinner slice thickness produces enhanced oblique voxel resolution. Thinner original tomographic image slices also result in a reduced field of view in the oblique images. Thus there is a tradeoff between oblique voxel resolution and oblique image field of view that occurs when the original tomographic images are acquired. In the case of the acquired MR images the field of view in the oblique images can be increased by increasing the slice thickness or by introducing slice gaps.

The retrospective oblique reformatting method discussed in this section provides a very useful tool for expanding the utility of acquired tomographic medical images. In the next section of this chapter two separate cardiac MR studies are obliquely reformatted to illustrate the appearance of the reformatted tomographic images. The method presented in this chapter applies equally well to other tomographic multi-slice imaging modalities. In the future it is expected that this form of image processing will continue to grow in importance and expand in availability. This is partly a result of the increasing capabilities of computer hardware and partly due to the needs of the medical imaging community.

5.3 EXAMPLES OF RETROSPECTIVELY REFORMATTED OBLIQUE CARDIAC IMAGES

The retrospective oblique reformatting method discussed in this chapter is useful for producing oblique cardiac MR images oriented along the long and short axes of the heart. As previously indicated, either because the MR imager was unable to acquire images obliquely or due to misalignment of the acquired image slices there is a need to be able to retrospectively reformat the cardiac images along the cardiac axes. Further, because of the significant length of time it takes to acquire a multi-slice cine cardiac MR image study along only a single slice axis it is not feasible to also acquire images along an second cardiac axis. Hence the retrospective oblique reformatting of cardiac MR images can satisfy this need as it arises in the analysis of cardiac functional performance. This topic will be further discussed in the following chapter. In the remainder of this chapter the results of an actual application of the oblique reformatting method will be presented.

In the first example a transaxial multi-slice cardiac MR image study was retrospectively obliquely reformatted along the long and short cardiac axes. The cardiac image acquisition procedure discussed in Chapter 3 was utilized to produce these images using a Toshiba Access MR Imager. The number of acquired image slices in this study was fourteen and the slice thickness was 10 mm. The in-plane resolution of the original tomographic images was 2.2 mm by 1.1 mm. The number of acquired slices serves to enhance the field of view of the obliquely reformatted images while not sacrificing oblique voxel resolution. The reformatting will be carried out at

MEMPHIS

the diastolic phase of the cardiac cycle because this temporal point usually has the best visualization of the left ventricular cardiac chamber. Figure 5.5a contains an original tomographic image that is acquired transaxial to the body's coordinate axis. Figure 5.5c is an obliquely reformatted short axis view constructed from the original transaxial tomographic data. Notice the improved symmetry of the left ventricular myocardium. Figure 5.5b contains an obliquely reformatted long axis view of the heart that slices the heart along the sagittal plane. This image shows the left ventricular chamber geometry including the over all shape and the chamber length. In addition this image also displays an excellent cross-section of the myocardial wall as it varies along the cardiac long axis. Notice that the apparent oblique voxel resolution in Figure 5.5c is significantly better than that in Figure 5.5b. This is due to the minimal tilt and rotation angles of this short axis oblique image with respect to the long axis oblique image.

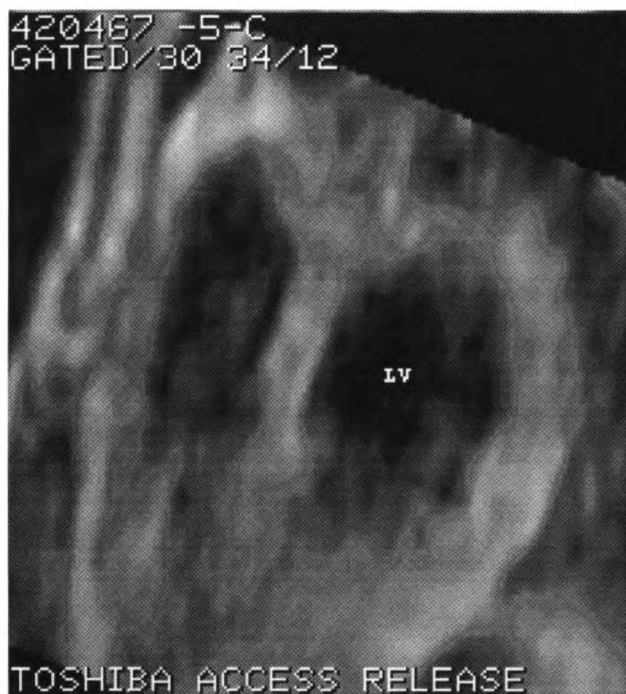
The apparent voxel resolution is what is actually observed in the oblique images. In order to compute the oblique image it is necessary to choose a set of actual oblique slice voxel dimensions. The actual voxel dimensions of the oblique images are listed in the caption of Figure 5.5. They are usually selected to be similar to the original tomographic voxel dimensions as this will be the optimal potential apparent voxel dimension. Overall the quality and field of view of these oblique cardiac images is very good and provides an useful representation of the state of the cardiac myocardium and the chamber volume.

JUNI LIBRARY

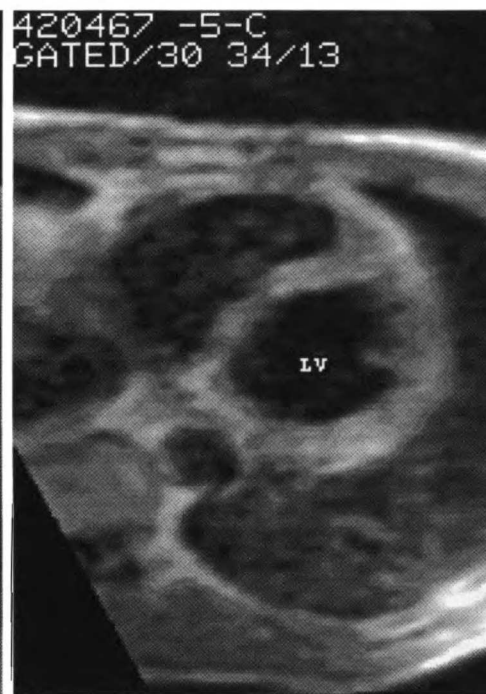
1971



(a)



(b)

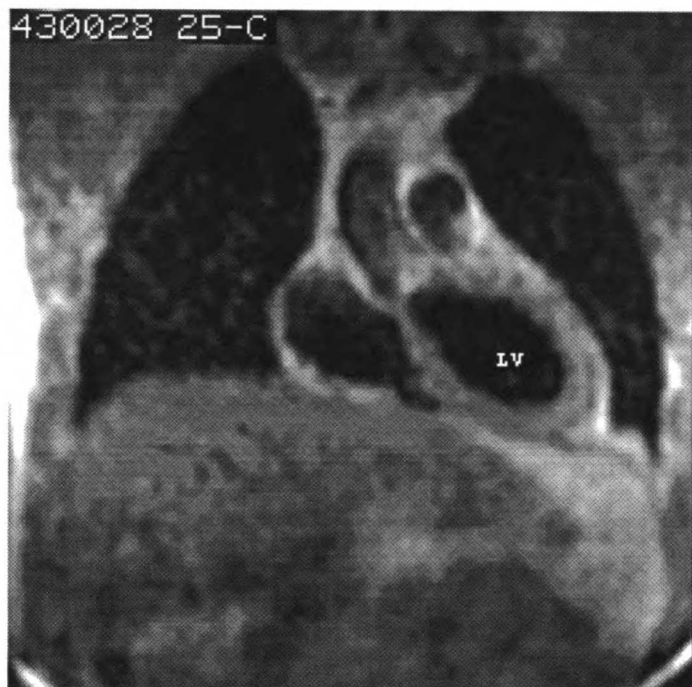


(c)

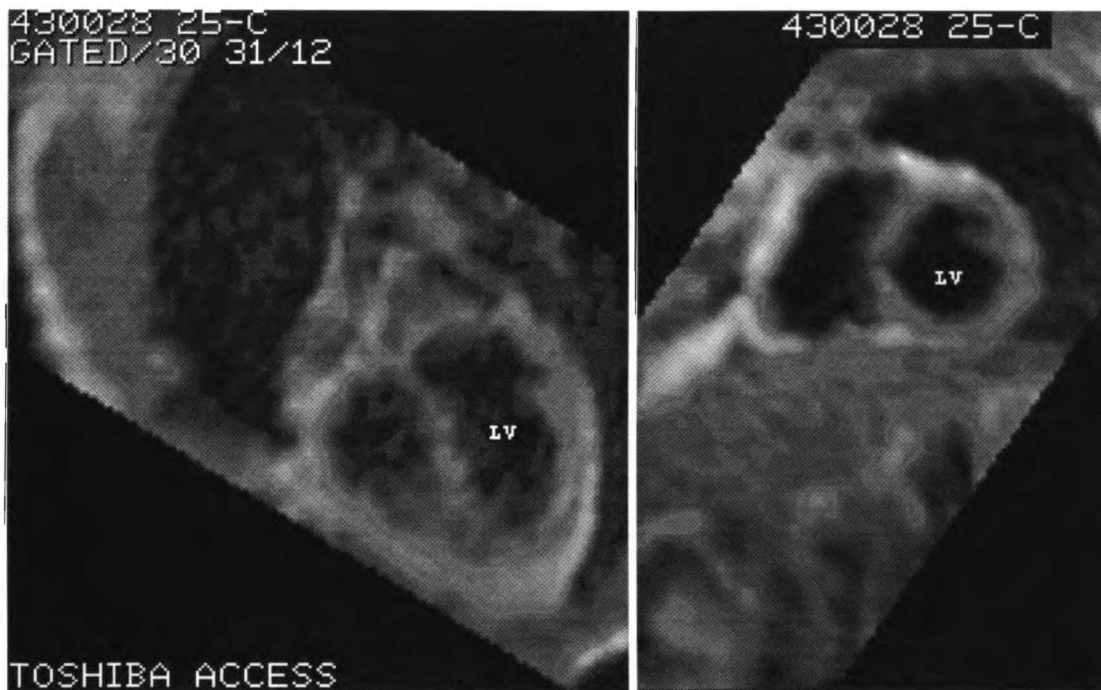
Figure 5.5 Retrospective oblique reformatting of a set of transaxial cardiac MR images acquired on a Toshiba Access MR Imager. (a) Original transaxial image (1 of 14 tomographic slices). Voxel dimensions and resolution: 2.2 mm, 1.1 mm, 10 mm. (b) Oblique long axis view. Voxel dimensions 1.1 mm, 1.1 mm, 7 mm. (c) Oblique short axis view. Voxel dimensions 1.1 mm, 1.1 mm, 7 mm.

MEMORANDUM

2



(a)



(b)

(c)

Figure 5.6 Retrospective oblique reformatting of a set of coronal cardiac MR images acquired on a Toshiba Access MR Imager. (a) Original coronal image (1 of 14 tomographic slices). Voxel dimensions and resolution: 2.0 mm, 2.2 mm, 10 mm. (b) Oblique long axis view. Voxel dimensions 2.0 mm, 2.0 mm, 10 mm. (c) Oblique short axis view. Voxel dimensions 2.0 mm, 2.0 mm, 10 mm.

1951

The next oblique reformatting example is very similar except that the original tomographic axis is oriented along the body's coronal plane. This example is illustrated in Figure 5.6. Figure 5.6a contains an original coronal tomographic cardiac image. As in the previous example the original cardiac images were acquired using a Toshiba Access MR Imager. Fourteen multi-slice images were acquired with 10 mm slice thickness. The in-plane resolution of the cardiac images were 2.0 mm by 2.2 mm. Figure 5.6b contains a cardiac long axis oblique view of the heart while Figure 5.6c contains a cardiac short axis oblique view. The apparent voxel resolutions of these two oblique images are more similar than in the previous example due to the relative similarity in the tilt and rotation angles required to produce these oblique images. These oblique long and short axis images again show the left ventricular cardiac chamber and the left ventricular myocardium rather well. In the case of the short axis view, the myocardium again appears symmetrical. Figures 5.5 and 5.6 are representative of the cardiac studies that will be used in the following chapters to study the ability of cardiac MR to evaluate left ventricular function.

JUNI LIBRARY

MEMORANDUM

CHAPTER 6

FUNCTIONAL ANALYSIS OF THE LEFT VENTRICULAR CHAMBER VOLUME

6.1 INTRODUCTION

Cardiac functional parameters are acquired from tomographic cardiac medical images using the methods described in Section 2.5. In this chapter these methods are applied to cardiac magnetic resonance (MR) images in order to determine functional parameters of the left ventricular (LV) chamber volume. This approach is continued in Chapter 7 where the left ventricular myocardial mass is determined and in Chapter 8 where the left ventricular myocardial wall thickening and motion are determined. The measured MR functional parameters presented in this and the following chapters are examined by comparing parameters that are measured using different methods. An additional comparison is made in this chapter and Chapter 7 between the measured MR functional parameters and the corresponding parameters measured by echocardiography.

The cardiac MR images that were utilized for this functional analysis were acquired from a Toshiba Access 0.064 Tesla MR Imager using the gated cardiac spin echo imaging method described in Chapter 3. The echo time, TE, for these images was 30 msec and the repetition rate, TR, fluctuated as discussed in Section 3.3. The spatial resolution of the image voxels in the acquisition plane was typically 2 mm by 2 mm with a slice thickness of 10 mm. Signal averaging was not used in order to

INDEX

minimize the overall acquisition time of the imaging procedure. The gated cardiac MR imaging procedure results in seven spatially adjacent tomographic image slices each with fourteen temporally sequential cine image frames. These cardiac MR images will be obliquely reformatted and it is desirable to extend the field of view in the resulting oblique images. This can be accomplished by repeating the acquisition procedure with an appropriate spatial offset resulting in a total of fourteen spatially adjacent image slices. The temporal resolution of the cine image frames is 50 msec. The temporal filter discussed in Chapter 4 was applied to these cine cardiac MR images in order to reduce the stochastic noise.

Twelve cardiac MR image studies were acquired for the purpose of making the comparisons in this and the following chapters. These cardiac image studies were acquired from nine volunteers who gave informed consent. The individuals in this patient sample were all healthy males with no diagnosed cardiovascular abnormalities. Their ages ranged from 25 through 45. As is indicated by Table 2.5 and Table 2.6 this patient sample can be expected to produce a set of measured cardiac functional parameters that is narrowly distributed. The cardiac functional parameters which are measured from these MR image studies contain uncertainties. To estimate these uncertainties three individuals from the patient sample were imaged again a short time later expanding the study size to twelve. The measurement uncertainty for each cardiac functional parameter is then determined by calculating the average of the standard deviations in each of these three individuals of each of the measured cardiac functional parameters.

JUN 19 1988

1971

An echocardiographic image acquisition of each patient from the cardiac MR image studies was also performed on the same day as the respective MR image acquisitions. The echocardiographic images were acquired so that each patient's cardiac functional parameters could be measured and then be compared to the corresponding MR parameters. This was desired because the echocardiographic functional parameters are an accepted standard [12]. The echocardiographic functional parameters were provided for use in this dissertation by the staff of an University of California, San Francisco echocardiographic laboratory. The measurement uncertainty in each of these parameters is determined through the method described above. These measurement uncertainties, for both the MR and the echocardiographic functional parameters, are indicated throughout this and the following chapters by the error bars on the data plots. In addition, the sources of these uncertainties will be identified and their value estimated in the next section.

Cardiac functional parameters are measured from end diastolic and end systolic images. These temporal image frames are identified by applying the guidelines presented in Section 2.5 as the sequential images are displayed in a cine format. The cardiac functional parameters which are measured from these images include: the end diastolic volume (EDV), the end systolic volume (ESV), the ejection fraction (EF), the myocardial mass, the ventricular chamber length, the myocardial wall thickening and the myocardial wall motion. Each of these functional parameters were introduced and discussed previously in Chapter 2. This discussion included the various methods which can be utilized to determine these functional parameters. In this and the following chapters these methods are utilized

REQUIRERE

to measure the described cardiac functional parameters from the cardiac MR patient studies. The results of these measurements are presented in Appendix Table A.1 along with the provided echocardiographic parameter measurements. In this chapter and the following chapters these results are compared, but first a discussion of the functional parameter uncertainties is presented.

UNIVERSITY OF MICHIGAN

MEMPHIS

6.2 MAGNETIC RESONANCE CARDIAC FUNCTIONAL PARAMETER UNCERTAINTIES

6.2.1 CARDIAC FUNCTIONAL PARAMETER MEASUREMENT

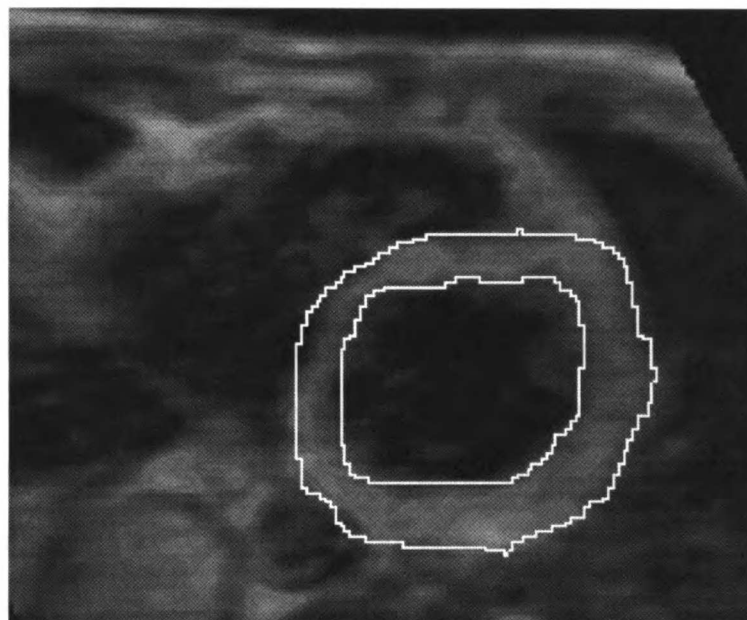
Uncertainties in the measured MR cardiac functional parameters arise from two potential sources: uncertainties in the location of a defined image boundary, or inaccuracies in the parameter approximation model. In this section the effects of these uncertainties will be examined.

The cardiac functional parameter measurements presented in this dissertation all rely on the same basic measurement, a defined boundary. This boundary is used to indicate either the total number of voxels within a chosen region of interest (ROI) or the endpoints of a linear dimension (Figure 6.1). Recall from Section 2.5 that the functional parameter methods fall into two groups: summed multi-slice parameter methods and approximated parameter methods. Left ventricular endocardial boundaries and left ventricular epicardial boundaries are defined on both end-diastolic and end-systolic MR images in order to apply these methods. This results in the volumetric functional parameters and linear functional parameters listed in Section 6.1. Note that approximation methods currently are only used for the volumetric functional parameters.

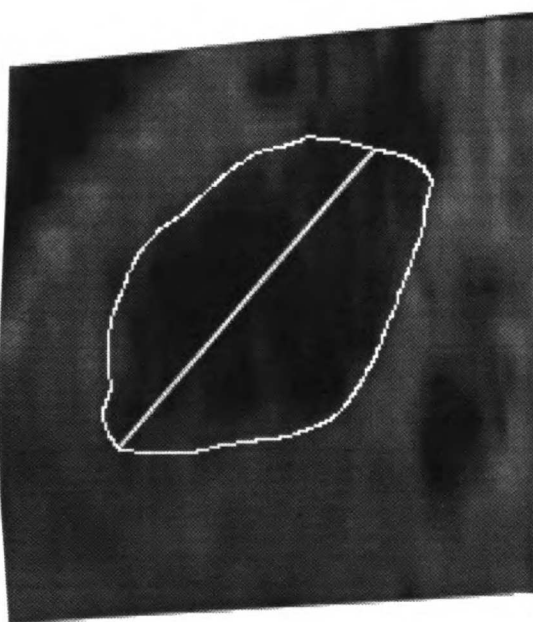
The summed multi-slice volumetric functional parameters are measured by defining boundaries around the desired left ventricular volume in a series of adjacent image slices. These images completely encompass the extent of the left ventricle. The number of voxels within each

UNIVERSITY OF MICHIGAN

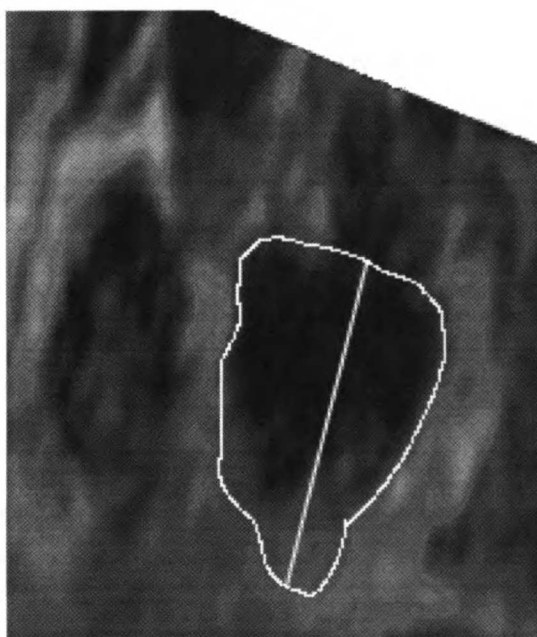
11211



(a)



(b)



(c)

Figure 6.1 Examples of LV volumetric and linear dimension MR functional parameter components.

(a) Short axis endocardial and epicardial boundary definition. The endo. boundary determines chamber volume and when combined with the epi. boundary determines the myocardial mass and thickness.

(b) 2 chamber and (c) 4 chamber long axis cardiac images. The endo. boundaries in (b) and (c) are used in the biplane volume approximation method and individually in the area length method (Section 2.5).

MEMPHIS

boundary is determined and summed together to yield the total number of voxels contained by the selected volume. The volumetric functional parameter is then calculated by multiplying the total number of voxels within the boundaries by the voxel volume.

Unlike the summed multi-slice parameters, the approximated volumetric parameters are measured from either a single or a pair of cardiac images. This is accomplished through the use of left ventricular shape models that utilize ventricular chamber and myocardial boundaries to determine the functional parameters. There are four volumetric approximation methods that will be discussed in this section. The first two are utilized to determine the left ventricular chamber volume. They are the biplane method of discs (Figure 2.8) and the area length method (Figure 2.7). The final two are utilized to determine the left ventricular myocardial mass. They are the truncated ellipsoid method (Figure 2.9) and the area length method (Figure 2.9).

The volumetric approximation methods presented above were each developed for use with cardiac images that are oriented along both the cardiac long axis and the cardiac short axis. The images produced by the Toshiba Access MR imager for the previously described patient study are restricted to the standard tomographic image planes of the human body. Therefore the retrospective oblique reformatting methods presented in the previous chapter are applied in order to produce the desired cardiac long and short axes images. At a minimum, only three centered left ventricular images are required in order to apply the approximation methods. These three images are required from both the end diastolic and the end systolic

11
12
13
14
15
16
17
18
19
20
21
22
23
24
25
26
27
28
29
30
31
32
33
34
35
36
37
38
39
40
41
42
43
44
45
46
47
48
49
50
51
52
53
54
55
56
57
58
59
60
61
62
63
64
65
66
67
68
69
70
71
72
73
74
75
76
77
78
79
80
81
82
83
84
85
86
87
88
89
90
91
92
93
94
95
96
97
98
99
100

temporal phases of the cardiac contraction cycle. The orientations of these images are directed along the apical two chamber, the apical four chamber, and the short axis cardiac image planes.

The boundaries which are defined for the functional parameter measurements are as follows. The endocardial boundary is utilized in the definition of the summed multi-slice ventricular volume. The endocardial and the epicardial boundary are both used to define the summed multi-slice myocardial mass. In the case of the biplane chamber volume the endocardial boundary is defined in two orthogonal long axis images. These boundaries determine the linear dimensions of the short axis cross-sectional diameters and the long axis chamber length. The area length chamber volume is defined from the endocardial boundary of a single cardiac long axis image. From this boundary the long axis chamber length and chamber area are determined. The myocardial mass approximation methods differ in that they utilize the endocardial and the epicardial boundaries that are defined on both long and short axis cardiac images. These boundaries specify the short axis cross-sectional thickness of the myocardium in addition to the long and short axis chamber lengths. Myocardial wall thickening and myocardial wall motion are the final two parameter measurements. These measurements are not approximated. They are determined by the radial distance between either the endocardial and the epicardial boundaries or the endocardial boundary and a selected center point. For further discussion of these boundaries please refer to Section 2.5.

MINI 2011

Consistent cardiac functional parameter measurements are facilitated by the consistent definition of the boundaries described above. In order to achieve this result the described methods are applied to images that have been obliquely reformatted along the cardiac long and short axes. In addition, the ventricular boundaries are defined according to the criteria described in Section 2.5.

6.2.2 TYPES OF PARAMETER UNCERTAINTIES

Cardiac functional parameter measurements contain uncertainties that are divided into two categories: systematic uncertainties and random uncertainties. Systematic uncertainties refer to consistent variations in the measured functional parameters. These systematic uncertainties include variations that are unique to a particular individual over repeated parameter measurements. Random uncertainties are those variations that occur over repeated parameter acquisitions of the same individual. The sources of these parameter uncertainties are described in Subsection 6.2.3 through Subsection 6.2.9. The discussion presented in these subsections is summarized below in Table 6.1 through Table 6.5.

U
N
I
V
E
R
S
I
T
Y
O
F
M
I
C
H
I
G
A
N

RECEIVED
JUN 15 1964

UNCERTAINTY ABBREVIATION KEY		
UNCERTAINTY ABBREVIATION	SECTION REFERENCE	REASON FOR UNCERTAINTY
CALIB	6.2.3	SYSTEMATIC CALIBRATION
BOUND	6.2.4	SYSTEMATIC BOUNDARY DETERMINATION
FORSHRT	6.2.5	SYSTEMATIC FORESHORTENING
MODEL	6.2.6	SYSTEMATIC MODEL INACCURACIES
SYSBLD	6.2.7	SYSTEMATIC INCREASED IMAGE INTENSITY OF SYSTOLIC BLOOD
ATKICK	6.2.8	SYSTEMATIC ATRIAL KICK
PVOL	6.2.9	RANDOM PARTIAL VOLUME EFFECTS
COMB	6.2.10	COMBINED UNCERTAINTIES

Table 6.1 Summary of abbreviations used to identify the various uncertainties.

VENTRICULAR CHAMBER LENGTH UNCERTAINTIES								
MEASUREMENT METHOD AND FUNCTIONAL PARAMETER	CALIB	BOUND	FORSHRT	MODEL	SYSBLD	ATKICK	PVOL	COMB
MR DIASTOLIC LONG AXIS LENGTH	$\pm 5\%$		$\pm \sim 0\%$			-17%	$\pm 1.9\%$	-17 $\pm 5.3\%$
MR SYSTOLIC LONG AXIS LENGTH	$\pm 5\%$		$\pm \sim 0\%$		-25%		$\pm 2.6\%$	-25 $\pm 5.6\%$

Table 6.2 Summary of ventricular chamber length uncertainties. The combined percentage uncertainties in the last column are given in terms of the systematic uncertainty \pm the random uncertainty.

MEMPHIS

VENTRICULAR CHAMBER FUNCTIONAL PARAMETER UNCERTAINTIES								
MEASUREMENT METHOD AND FUNCTIONAL PARAMETER	CALIB	BOUND	FORSHRT	MODEL	SYSBLD	ATKICK	PVOL	COMB
MR SUMMED MULTI-SLICE LONG AXIS EDV	±6.5%					-17%	± 14%	-17 ± 15%
MR SUMMED MULTI-SLICE SHORT AXIS EDV	±6.5%	-3.7%				-17%	± 8 %	-17 ± 10%
MR SUMMED MULTI-SLICE LONG AXIS ESV	±6.5%				-25%		±18%	-25 ± 19%
MR SUMMED MULTI-SLICE SHORT AXIS ESV	±6.5%	8.6%			-25%		± 10%	-16 ± 12%
MR SUMMED MULTI-SLICE LONG AXIS EF					~ 0%	~ 0%	±~ 0%	0%
MR SUMMED MULTI-SLICE SHORT AXIS EF		-6 %			~ 0%	~ 0%	±~ 0%	-6%
MR BIPLANE EDV	±6.5%		± ~ 0%	-21%		-17%	± 14%	-27 ±15%
MR BIPLANE ESV	±6.5%		± ~ 0%	-6%	-25%		±18%	-26 ±19%
MR BIPLANE EF			± ~ 0%	-14%	~ 0%	~ 0%	±~ 0%	-14%
MR AREA LENGTH EDV	±6.5%		± ~ 0%	-16%		-17%	± 14%	-23 ±15%
MR AREA LENGTH ESV	±6.5%		± ~ 0%	-10%	-25%		±18%	-27 ±19%
MR AREA LENGTH EF			± ~ 0%	-13%	~ 0%	~ 0%	±~ 0%	-13%

Table 6.3 Summary of ventricular chamber functional parameter uncertainties. The combined percentage uncertainties in the last column are given in terms of the systematic uncertainty ± the random uncertainty.

INDEX

MYOCARDIAL MASS FUNCTIONAL PARAMETER UNCERTAINTIES								
MEASUREMENT METHOD AND FUNCTIONAL PARAMETER	CALIB	BOUND	FORSHRT	MODEL	SYSBLD	ATKICK	PVOL	COMB
MR SUMMED MULTI-SLICE LONG AXIS MYOCARDIAL MASS	±6.5%					17%	±18%	17 ± 19%
MR SUMMED MULTI-SLICE SHORT AXIS MYOCARDIAL MASS	±6.5%	-12 %				17%	±11%	5 ± 13%
MR TRUNCATED ELLIPSOID MYOCARDIAL MASS	±6.5%		± ~ 0%	27%		17%	±18%	32 ± 19%
MR AREA LENGTH MYOCARDIAL MASS	±6.5%		± ~ 0%	34%		17%	±18%	38 ± 19%

Table 6.4 Summary of myocardial mass functional parameter uncertainties. The combined percentage uncertainties in the last column are given in terms of the systematic uncertainty ± the random uncertainty.

CONTRACTILITY FUNCTIONAL PARAMETER UNCERTAINTIES								
MEASUREMENT METHOD AND FUNCTIONAL PARAMETER	CALIB	BOUND	FORSHRT	MODEL	SYSBLD	ATKICK	PVOL	COMB
MR MYOCARDIAL WALL THICKENING			± ~ 0%		25%	-17%	±9.4%	8 ± 9.4%
MR MYOCARDIAL WALL MOTION			± ~ 0%		25%	-17%	±9.4%	8 ± 9.4%

Table 6.5 Summary of contractility functional parameter uncertainties. The combined percentage uncertainties in the last column are given in terms of the systematic uncertainty ± the random uncertainty.

MEMBER

6.2.3 SYSTEMATIC CALIBRATION UNCERTAINTIES (CALIB)

There are two sources of systematic calibration uncertainties: voxel resolution and gray scale windowing. These calibration uncertainties are present in both the cardiac MR images and the echocardiographic images. It is assumed that the calibration uncertainties in the echocardiographic images are similar in magnitude to those found in the MR images.

The first source of calibration uncertainty arises from the accuracy of the image voxel resolutions. These resolutions determine the linear dimension, area, or volume values specified by the boundaries described in Subsection 6.2.1. The Toshiba Access MR Imager's specifications limit the voxel resolution uncertainties to 3.0 % within the image plane and 5.0 % along the slice axis. This applies to the voxel resolutions of the cardiac MR images which were presented previously to be 2 mm by 2 mm within the image plane and 10 mm along the slice axis.

Recall that the MR images are obliquely reformatted before the cardiac functional parameter boundaries are defined. Therefore, measured ventricular linear dimensions have a resolution calibration uncertainty that ranges between 3.0 % and 5.0 %. Measured areas have a resolution calibration uncertainty that ranges between 4.2 % and 5.8 %. The resolution calibration uncertainty of all volumes measured from these images is 6.5 %.

MINI 20

The second source of calibration uncertainty arises from the gray scale window settings of the image display. As the window is adjusted the apparent endocardial and epicardial boundaries vary. In order to define these boundaries in a consistent fashion the window of each displayed MR image must be set consistently. This is accomplished by setting the gray scale window to run from zero to the maximum voxel intensity of the particular image. This produces a consistent result because the maximum image intensity arises from subcutaneous fat and the image intensity ratio of these fat voxels to the myocardial voxels remains consistent for a particular individual. It is assumed that this gray scale results in defined ventricular boundaries with negligible gray scale calibration uncertainties.

The two calibration uncertainties listed above occur in the measured long axis chamber length, the end diastolic chamber volume, the end systolic chamber volume, and the myocardial mass. These uncertainties are not present in the functional parameters that are determined from a ratio of measured parameters. These parameters include the ejection fraction, the wall thickening, and the wall motion.

6.2.4 SYSTEMATIC BOUNDARY UNCERTAINTIES (BOUND)

Anatomic landmarks in the cardiac images are utilized to identify the endocardial and the epicardial boundaries. The appearance of these landmarks in long and short axis cardiac images is not the same. This results in a systematic uncertainty in the boundaries that are defined in these images. The most significant of these uncertainties occurs in the superior region of the left ventricle. This region includes the aortic outflow

INSTRUMENT

track and the confluence with the atrium. In both of these structures there is an absence of myocardial tissue which complicates the definition of the endocardial and the epicardial boundaries. In order to provide a consistent solution to this complication the superior margin of these boundaries is defined to occur along the mitral valve plane.

In long axis cardiac images the mitral valve plane is usually identified with minimal uncertainty. This is the case in cardiac MR images even though the valve leaflets are often not visible. In instances where the valve leaflets are not visible the mitral valve plane is identified by the characteristic notched shape of the myocardium at the roots of the mitral valve.

In short axis cardiac images the identification of the mitral valve plane contains an increased uncertainty. This is because short axis images are oriented almost parallel to the mitral valve plane. Hence the mitral valve will occur in cross-section in a single short axis image slice and there is uncertainty in the identification of this slice. This uncertainty arises because the short axis cross-sections of the superior ventricular chamber, the mitral valve, and the inferior atrial chamber all have a similar diameter and appearance. In Chapter 2 it was stated that the myocardial wall dramatically thins in the left atrium as compared to the left ventricle. The mitral valve plane in the short axis images can therefore be selected by identifying the thinning myocardial wall which occurs at the transition to atrial myocardial tissue. Therefore, the short axis superior endocardial and epicardial boundaries are defined to occur at the image slice directly inferior to the first short axis slice that displays this atrial wall thinning.

INDEX

The systematic uncertainties that are introduced by defining the short axis ventricular volume in this manner can be estimated by comparing the long and short axes summed multi-slice functional parameters. Using the patient data presented in Appendix Table A.1, the average percent difference between the short axis and the long axis summed multi-slice end-diastolic volumes is -3.7 ± 12.0 . Likewise, the average percent difference between the short axis and the long axis summed multi-slice end-systolic volumes is 8.6 ± 19.0 . The summed multi-slice ejection fractions also contain this uncertainty and the average percent difference between the short axis and the long axis summed multi-slice ejection fractions is -6 ± 13.6 . From the patient data in Appendix Table A.1 the average percent difference between the short axis and the long axis summed multi-slice myocardial mass measurements is 11.7 ± 20.2 .

The described boundary systematic uncertainty occurs only in the functional parameters measured from short axis image slices. Only the functional parameters listed above are affected by this uncertainty. The approximated myocardial mass measurements are not affected because the short axis image that is utilized in these measurements is centered with respect to the ventricular long axis. The myocardial wall thickening and wall motion measurements are also unaffected by the systematic boundary uncertainty because they utilize short axis images that do not include the superior region of the left ventricle.

1951

6.2.5 SYSTEMATIC FORESHORTENING UNCERTAINTIES (FORSHRT)

Systematic foreshortening uncertainties occur in the measured functional parameters when the cardiac images are not properly aligned along their respective long or short axes. Image foreshortening results in an expansion or contraction of the measured ventricular chamber or myocardial linear dimensions. Image foreshortening also results in an expansion or contraction of the measured ventricular chamber or myocardial cross-sectional areas.

The cardiac MR images utilized in this dissertation are aligned along the long and the short cardiac axes using the retrospective oblique reformatting method described in Chapter 5. On the other hand, the orientation of acquired echocardiographic images is limited by the acquisition windows available to the image probe. The position of the heart in some patients may result in acquisition windows that prevent the echocardiographic image probe from aligning properly along the long or the short cardiac axes. Functional parameters measured from these images will contain systematic foreshortening uncertainties.

Systematic foreshortening uncertainties may also occur as a result of contractile motion of the heart. During contraction there is a spatial shift in the position of the heart as discussed in Chapter 2. This spatial shift may cause the systolic long and short cardiac axes to shift with respect to the corresponding diastolic axes. Current practice, and the convention used in this dissertation, is to utilize the same fixed image projection of the heart for both the diastolic and the systolic cardiac images [12]. This fixed image

MEMBER

projection is aligned along the respective cardiac long and short axes of the diastolic images. Systolic cardiac images may therefore be mis-aligned which may result in systolic functional parameters that contain foreshortening uncertainties. These uncertainties are systematic because the ventricle appears to follow a periodic pattern of motion during cardiac contraction.

The functional parameters that may be affected by foreshortening uncertainties are the ventricular chamber length, the biplane ventricular volume and ejection fraction, the area length ventricular volume and ejection fraction, the truncated ellipsoid and area length myocardial mass, the myocardial wall thickness, and the myocardial wall motion. Summed multi-slice functional parameters are not affected by ventricular image foreshortening. There is no evidence that the diastolic images from the patient studies presented in this dissertation contain any foreshortening uncertainties. There may be foreshortening uncertainties in the systolic cardiac images due to cardiac motion. It is assumed that these uncertainties are negligible.

6.2.6 SYSTEMATIC APPROXIMATION UNCERTAINTIES (MODEL)

Cardiac volumetric functional parameters are measured using the previously described summed multi-slice volume methods or approximated volume methods. The difference between these two methods is that the approximated volumes are based upon assumptions regarding the shape of the left ventricle. The actual shape of a particular individual's heart may not correspond to these assumptions and therefore results in the

introduction of systematic uncertainties in the approximated functional parameters. These uncertainties are discussed below.

Two ventricular chamber volume approximation methods were presented previously: the biplane and the area length methods. The preferred of these methods is the biplane approximation because it is considered to be more accurate [12]. The ventricular chamber model that the biplane approximation method utilizes assumes that the short axis endocardial boundaries have an elliptical shape. In this model the major and the minor axes of a series of adjacent short axis elliptical cross-sections are measured from the two chamber and the four chamber long axis images respectively. The major and the minor elliptical axes from each of the short axis cross-sections are then combined together to calculate an elliptical volume disc which approximates the corresponding short axis cross-sectional volume (Figure 2.8). These approximated volumes are then summed together to produce the net ventricular chamber volume. The net volume accurately represents the left ventricular volume only if each of the ventricular short axis cross-sections has an elliptical shape. In addition it is required that the two orthogonal long axis images intersect the ellipse's major and minor axes.

An example of a typical cardiac MR short axis cross-section of the left ventricle is presented in Figure 6.2. In this figure both the end diastolic and the end systolic images are presented along with their defined endocardial and epicardial boundaries. The diastolic image from this figure shows that the short axis cross-sectional shape follows the assumed elliptical model used in the biplane algorithm fairly well. The systolic image

MEMPHIS

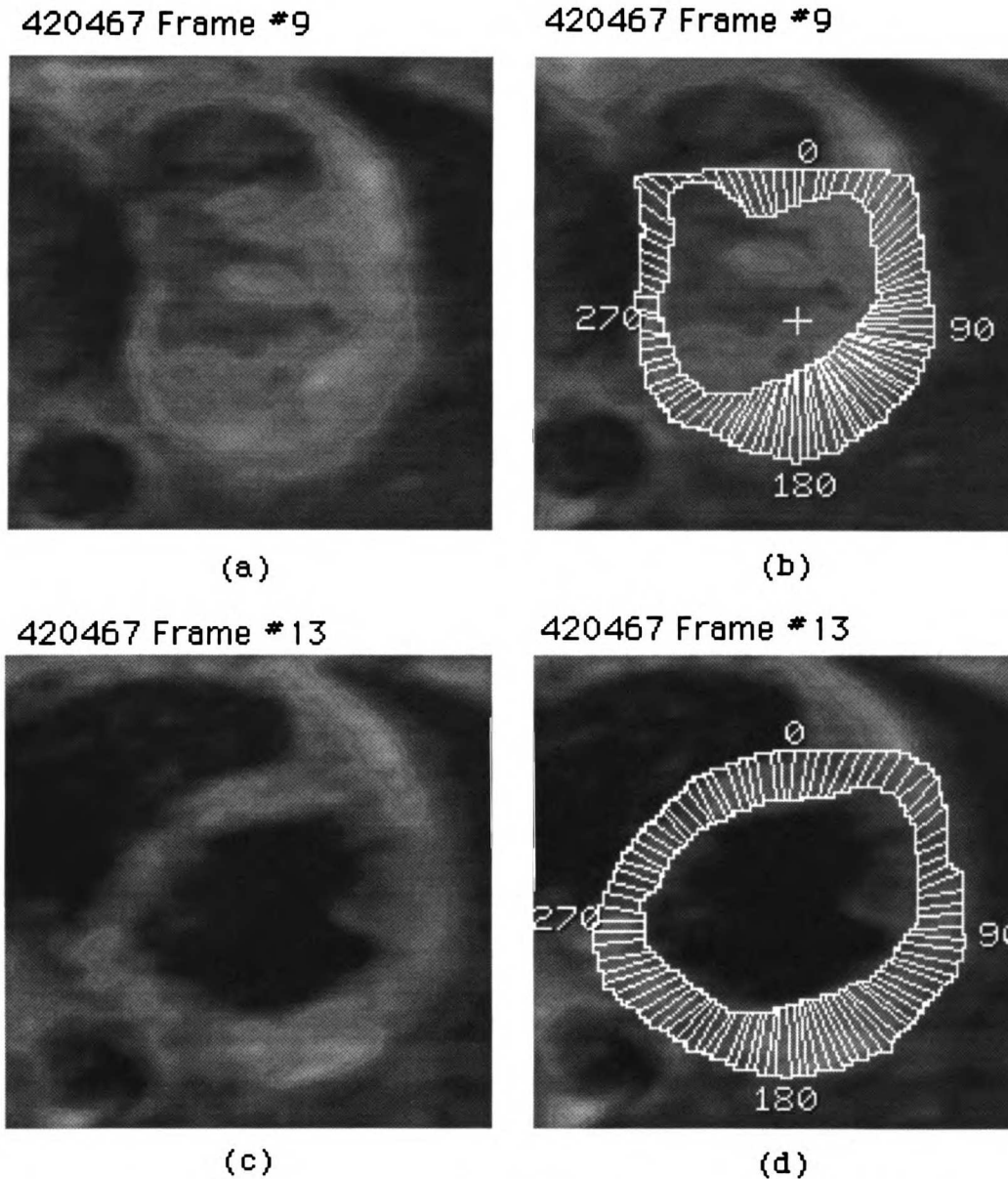


Figure 6.2 Short axis left ventricular cross sections and their inner endocardial and outer epicardial boundaries. (a) and (b) are the systolic temporal image frames and (c) and (d) are the diastolic temporal image frames. Additional temporal frames of this short axis slice level are presented in Figure 8.1.

from Figure 6.2 shows that the short axis ventricular cross-section can deviate to a large extent from the assumed elliptical cross-section.

Deviations from the model's assumed elliptical shape result in systematic

MINI

uncertainties in the approximated biplane chamber volumes and their corresponding biplane ejection fractions.

An estimate of the biplane approximation uncertainties can be made from the previously described patient study. This can be accomplished by calculating the average percent difference between the biplane functional parameters and their corresponding summed multi-slice long axis functional parameters. The measured parameters presented in Appendix Table A.1 are utilized for this purpose. The average percent difference between the biplane end diastolic volumes and the summed multi-slice long axis end diastolic volumes is -21 ± 21 . The average percent difference between the biplane end systolic volumes and the summed multi-slice long axis end systolic volumes is -6 ± 29 . The average percent difference between the biplane ejection fractions and the summed multi-slice long axis ejection fractions is -14 ± 28 . Long axis summed multi-slice parameters are utilized in this comparison because the approximated parameter boundaries are defined on these same images. This removes the effect of the boundary uncertainties (Subsection 6.2.5) from the parameter comparison.

The model which is used for the area length approximated volume has a more empirical nature than the previous case. It takes the square of the centered slice long axis ventricular area, divides this by the long axis length, and then multiplies the resulting volume by an experimentally developed scaling factor (Figure 2.7). This fixed scaling factor produces systematic uncertainties in the approximated volumes. Systematic uncertainties also occur in the area length volumes depending upon the rotation of the utilized image slice about the cardiac long axis. This is a

result of the fact that the short axis cross-sections do not have a uniform diameter, as can be seen in Figure 6.2. Typically, two chamber long axis orientations produce the largest area length volumes. This is because the two chamber orientation is usually parallel to the major axis of the elliptical short axis cross-section.

Using the data in Appendix Table A.1 the average percent difference between the area length end diastolic volumes and the summed multi-slice long axis end diastolic volumes is -16 ± 32 . The average percent difference between the area length end systolic volumes and the summed multi-slice long axis end systolic volumes is -10 ± 45 . The average percent difference between the area length ejection fractions and the summed multi-slice long axis ejection fractions is -13 ± 29 .

There are two myocardial mass approximation methods. They are similar except that the more common approach, the truncated ellipsoid method (Figure 2.9), utilizes a more complicated model for the myocardial shape in the superior region of the left ventricle. The other approximation approach is the area length method (Figure 2.9). These approximation methods utilize the same diastolic ventricular measurements in their respective approximation algorithms including: the average myocardial thickness, the short axis diameter, and the long axis chamber length. The myocardial thickness and the short axis diameter estimates are affected by the non-uniform shape of the short axis myocardial cross-section. This results in systematic uncertainties in the approximated myocardial mass measurements.

1951

Using the data in Appendix Table A.1 the average percent difference between the truncated ellipsoid myocardial mass approximation and the summed multi-slice long axis myocardial mass is -27 ± 12 . The average percent difference between the area length myocardial mass approximation and the summed multi-slice long axis myocardial mass is -34 ± 10 .

In this dissertation each of the parameter approximation methods are applied to the cardiac MR images. In the case of the echocardiographic images only the biplane chamber volume and the truncated ellipsoid myocardial mass methods are applied.

6.2.7 SYSTEMATIC SYSTOLIC BLOOD UNCERTAINTIES (SYSBLD)

Gated cardiac spin echo MR images contain an undesired MR signal from ventricular blood. This signal increases in intensity in systolic temporal images and results in a corresponding increase in the image intensity of the ventricular chamber contents. This reduces the contrast between the chamber blood pool and the myocardial tissue. As a result it becomes difficult to differentiate these tissues in the systolic cardiac MR images. This effect is worse in the ventricular region near the cardiac apex and subsides in the superior regions of the ventricle.

An example of the increased systolic blood signal can be observed in the systolic image in Figure 6.2 (a). The endocardial boundary for this image is indicated by the inner myocardial boundary in Figure 6.2 (b). This example shows that the increased image intensity of systolic blood can interfere with the definition of the endocardial boundary. In order to

overcome this difficulty the endocardial boundary is defined with visual assistance from a cine display of the temporal cardiac MR images. This allows for the observation of the systolic motion of the endocardium and the increasing blood signal. Tracking these tissues from frame to frame helps to differentiate the endocardial and the blood image intensities.

Overestimation of the endocardial boundaries occur when there is poor differentiation of the systolic blood from the endocardium resulting in systematic parameter uncertainties. These uncertainties manifest as an underestimation of the systolic summed multi-slice long axis and short axis volumes along with an overestimation of the corresponding summed multi-slice ejection fractions. These uncertainties also result in an underestimation of linear chamber dimensions and chamber areas. Hence a systematic reduction occurs in the systolic approximated chamber volumes along with a corresponding increase in the approximated ejection fractions. Myocardial mass measurements are not affected by these uncertainties because they utilize only diastolic images. Myocardial wall thickness and wall motion measurements are affected by the overestimation of the endocardial boundaries. Specifically, these uncertainties result in the systematic overestimation of the myocardial wall thickening and the myocardial wall motion.

In echocardiographic images the contrast at the endocardial boundary remains relatively consistent during cardiac contraction. An upper bound of the MR systolic blood functional parameter uncertainties can therefore be determined by comparing the systolic ventricular long axis chamber length in the cardiac MR images and the echocardiographic

1951

images. From the Appendix Table A.1 the average percent difference between the cardiac MR and the echocardiographic systolic long axis chamber lengths is -25 ± 10 . Ejection fraction uncertainties are determined through a combination of the EDV and ESV uncertainties utilizing typical EDV and ESV values of 110 ml and of 40 ml respectively.

6.2.8 SYSTEMATIC ATRIAL KICK UNCERTAINTIES (ATKICK)

The atrial kick phase of the cardiac functional cycle was described previously in Chapter 2. During this phase the left ventricular volume increases due to the contraction of the left atrium. If diastolic functional parameters are measured before the atrial kick occurs then the end diastolic linear dimensions and the end diastolic endocardial boundaries are underestimated. This results in systematic uncertainties in the diastolic functional parameters. This is not an issue in the end diastolic echocardiographic images as they are acquired after the atrial kick occurs. Unfortunately, end diastolic cardiac MR images are often acquired before the atrial kick occurs, as is the case in the images produced by the Toshiba Access MR imager.

Cardiac MR images are affected by the atrial kick uncertainties due to the fact that the cardiac MR imaging procedure is a gated technique. Cardiac gating requires that the imaging process be synchronized to the R wave of the ECG. In order to implement this gating technique it is required that the multi-slice MR signal acquisitions from each successive phase encode step be completed before the subsequent R wave occurs. As a result of this restriction the MR imaging procedure often misses the last portion of

U.S. LIBRARY

the diastolic cardiac phase where the atrial kick contraction ejects a small amount of blood into the left ventricle.

Missing the atrial kick results in the underestimation of the summed multi-slice end diastolic long and short axis volumes and the corresponding summed multi-slice ejection fractions. In addition the summed multi-slice long and short axis myocardial mass measurements may be overestimated. This is because the myocardial mass measurements are defined for a left ventricle that is fully expanded. Without the atrial kick the myocardium may appear to be thicker resulting in the overestimation.

The approximated MR cardiac functional parameters are also affected by the missed atrial kick. In the case of the end diastolic biplane and area length measurements the result is an underestimation of the approximated ventricular volume and the corresponding ejection fractions. This uncertainty may also cause an overestimation of the approximated myocardial mass measurements. This occurs as a result of the underestimated ventricular chamber area that is used to calculate the inner margin of the myocardial mass volume.

Finally, myocardial wall thickness and wall motion are affected by the atrial kick uncertainty. In both of these cases the end diastolic wall thickening and wall motion may be underestimated. This is because the end diastolic image is utilized as a base in these relative measurements.

An estimation of the atrial kick uncertainty can be produced from a comparison of the measured long axis chamber length from the end

ICF LBRN

diastolic echocardiographic images and the apparent end diastolic cardiac MR images. Utilizing the patient data presented in Appendix Table A.1 the average percent difference between the cardiac MR and the echocardiographic diastolic long axis chamber lengths is -17 ± 11 . Ejection fraction uncertainties are calculated as described in Subsection 6.2.7.

6.2.9 RANDOM PARTIAL VOLUME UNCERTAINTIES (PVOL)

Random partial volume uncertainties occur when an image voxel is only partially spanned by an imaged object. These uncertainties occur because it is not possible to determine how much of the image voxel actually contains the object. Therefore the voxel's entire linear dimensions are either counted in or excluded from the measure of the object's dimensions.

Partial volume voxel uncertainties appear in the measured functional parameters at the end points of linear dimension measurements, at the boundaries of cross-sectional areas, and in the end slices of summed multi-slice volumes. On average, voxels with partial volume effects are assumed to have uncertainties that are equal to $\pm 1/2$ the voxel resolution along each of the image axes. The cardiac MR images utilized in this dissertation therefore have partial volume uncertainties of ± 1 mm within the acquisition image plane and ± 5 mm along the acquisition slice axis. Oblique reformatting of the cardiac MR images potentially increases the apparent in-plane voxel dimensions which results in a increase in the corresponding voxel partial volume uncertainties.

JOSE LIBRARI

Partial volume uncertainties are evaluated by comparing the estimated partial volume in a particular measurement to the value of the measured parameter. Typical cardiac linear dimension partial volume uncertainties for the MR images utilized in this dissertation are listed in Table 6.6:

Parameter	Typical Linear Dimensions	Partial Volume Uncertainty
Diastolic Ventricular Long Axis Length	75 mm	1.9 %
Systolic Ventricular Long Axis Length	55 mm	2.6 %
Diastolic Ventricular Short Axis Length	40 mm	3.5 %
Systolic Ventricular Short Axis Length	30 mm	4.7 %
Myocardial Wall Thickness	15 mm	9.4 %

Table 6.6 This table contains the typical linear dimension partial volume uncertainties. These uncertainties are for the cardiac MR images utilized in this dissertation.

Cross-sectional area boundaries are defined along a specific anatomic structure. As a result of random partial volume effects there is an equal probability that boundary pixels will either contain or exclude portions of this anatomic structure. The number of excess or absent pixels in successive definitions of the area boundary is described by a binomial distribution. Typical end diastolic chamber volumes have a cross-sectional area containing 1250 pixels and a circumference of 126 pixels. The number of partial volume pixels is then determined by the standard deviation of a binomial distribution with 126 trials. This is found to be ± 6 pixels. The resulting partial volume uncertainty in this typical cross-sectional diastolic chamber area is 0.5 %. In a similar fashion, typical partial volume uncertainties for end systolic cross-sectional areas (area = 706 pixels, circumference = 94 pixels) and myocardial cross-sections (area = 515 pixels, circumference = 274 pixels) are 0.7 % and 1.5 % respectively. These

uncertainties are small and do not appreciably effect the measured parameters in which they are utilized.

Summed multi-slice parameter volumes contain partial volume uncertainties within the defined cross-sectional volumes of the opposing end slices. These uncertainties occur along the image slice axis and are assumed to equal 1/2 of the defined cross-sectional volume in each of these slices. It is assumed that the defined cross-sectional areas in the summed image slices are approximately equal. The summed multi-slice partial volume uncertainties are then estimated in terms of cross-sectional slices. In Table 6.7 the typical number of summed multi-slice cross-sectional

Summed Multi-Slice Ventricular Parameter	Typical Number of 10 mm Thick Slice Boundaries Utilized in Multi-Slice Parameter	Slice Axis Partial Volume Uncertainty
Long Axis End Diastolic Endocardial Volume	5	$\pm 14 \%$
Long Axis End Systolic Endocardial Volume	4	$\pm 18 \%$
Long Axis End Diastolic Epicardial Volume	6	$\pm 12 \%$
Short Axis End Diastolic Endocardial Volume	9	$\pm 8 \%$
Short Axis End Systolic Endocardial Volume	7	$\pm 10 \%$
Short Axis End Diastolic Epicardial Volume	10	$\pm 7 \%$

Table 6.7 This table contains the summed multi-slice parameter slice axis partial volume uncertainties. These uncertainties are for the cardiac MR images utilized in this dissertation.

JOSE L. BERNARDINI

slices is presented along with the estimated partial volume uncertainties of these parameters. Ejection fraction uncertainties are calculated as described in Subsection 6.2.7. Summed myocardial mass partial volume uncertainties are determined by the quadrature combination of the endocardial boundary uncertainty and the epicardial boundary uncertainty. Partial volume uncertainties in the approximated functional parameters are assumed to be similar to the uncertainties in the summed multi-slice parameters.

In the case of the long axis summed multi-slice myocardial mass the partial volume uncertainty may increase as the cardiac images become parallel to the major axis of the elliptical short axis cross-section. Figure 6.3 shows that such images are more likely to violate the assumption that the summed cross-sectional slices have equal volumes. In this situation the bulk of the myocardial volume occurs in the end slices

420467 Frame #13

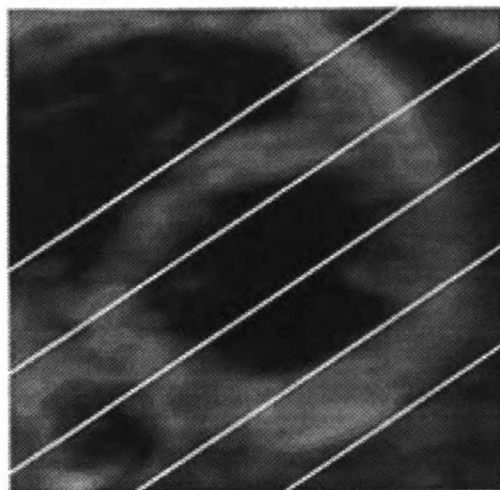


Figure 6.3 Intersection of a sequence of long axis images with the short axis cross-section. These long axis images are oriented such that they are parallel to the major axis of the elliptical cross-section.

102
103
104
105
106

causing the increase in the partial volume uncertainty. Therefore the short axis summed multi-slice parameter measurement is preferred for the myocardial mass.

6.2.10 CONCLUSION

The uncertainties presented in the previous subsections are assumed to be independent of each other. Therefore the negative systematic uncertainties, the positive systematic uncertainties, and the random uncertainties are combined separately in quadrature and then summed together to produce the estimated net parameter uncertainties. These combined uncertainties are presented in the final columns of Table 6.2 through Table 6.5. The results in these tables show that the random uncertainty component is dominated by the partial volume uncertainties. The systematic uncertainty component in diastolic parameters is dominated by the atrial kick uncertainty. Systolic parameters are dominated by the systolic blood uncertainty. Approximated parameters, as shown in Table 6.3 and Table 6.4, are also dominated by the systematic model uncertainties.

The uncertainties which affect the myocardial wall thickening and motion vary depending upon the cardiac phase of the measurement. The combined uncertainties listed in Table 6.5 therefore represent an upper bound on the uncertainty for individual linear dimension measurements over the cardiac contraction cycle. These parameters are evaluated over a region containing many line segments. This effectively averages these linear measurements which in turn reduces the apparent random

1951
MAY 1951

parameter uncertainties by the square root of the number of unique line segments in the region. Typical myocardial regions contain ten line segments. Therefore the myocardial wall thickening and motion random uncertainties appear to be reduced to a value of 3.0 % from 9.4 %.

The combined parameter uncertainties presented here are consistent with the expected clinical use of the cardiac functional parameters. This can be shown by a comparison of the corresponding cardiac MR and echocardiographic functional parameters measured from the previously described patient study. The results of this study are recorded in Appendix Table A.1. Table 6.8 presents the mean values of these functional parameters along with their population variations. The fact that the population variations are consistent in the corresponding MR and echocardiographic parameters shows that the random uncertainties in these parameters are of the same magnitude. This variation is acceptable as it also corresponds with the normal variation for a similar population as presented in the literature [12]. In the case of the end systolic volumes this correspondence is reduced. This appears to be the result of statistical variations in the patient sample as both the MR and echocardiographic parameters remain consistent. The relevant parameter values from the literature reference [12] are listed in the final column of Table 6.8. These literature parameter measurements were acquired using an echocardiographic imaging technique.

Cardiac Functional Parameter	Measured MR Parameter	Measured Echocardiographic Parameter	Literature values of the Echocardiographic Parameters [12]
Biplane End Diastolic Volume	102 ± 22 ml (± 22 %)	110 ± 22 ml (± 20 %)	111 ± 22 ml (± 20 %)
Biplane End Systolic Volume	41 ± 11 ml (± 27 %)	40 ± 11 ml (± 28 %)	55 ± 10 ml (± 18 %)
Truncated Ellipsoid Myocardial Mass	194 ± 31 gm (± 16 %)	159 ± 19 gm (± 12 %)	148 ± 26 gm (± 18 %)

Table 6.8 In this table the average value and variation of the measured cardiac functional parameters from the discussed patient study are listed. These results are given fully in the Appendix Table A.1. This table also lists the accepted normal values for these parameters and their variation in a population which corresponds to this patient study [12]. In parenthesis the variations are also given as a percentage of the measured parameters.

The combined parameter uncertainties presented in Table 6.2 through Table 6.5 further justify that the MR images can be used to measure cardiac functional parameters. The relevant combined uncertainties from these tables are reproduced below in Table 6.9. This shows that the random uncertainties in the biplane end diastolic volume, the end systolic volume, and the truncated ellipsoid measurements are reasonably within the range of the normal population variation

Cardiac Functional Parameter	Percentage Combined Uncertainty (systematic uncertainty ± random uncertainty)
Biplane End Diastolic Volume	-27 ± 15 %
Biplane End Systolic Volume	-26 ± 19 %
Truncated Ellipsoid Myocardial Mass	10 ± 19 %

Table 6.9 This table reproduces the combined systematic and random uncertainties from Table 6.3 and Table 6.4 that correspond to the parameters listed in Table 6.8.

1021221

presented in Table 6.8. These random uncertainties confirm that the MR cardiac functional parameters are able to resolve the measured cardiac functional parameters within the normal population variation.

Table 6.9 also presents the combined systematic uncertainties that are expected to occur in these MR parameters. These uncertainties reflect in part the systematic offset of the cardiac MR parameters with respect to the actual ventricular parameters. Echocardiographic parameters contain systematic uncertainties that are likely to differ from those of the MR parameters. Hence the systematic uncertainties listed in Table 6.9 are not likely to produce a correspondence in the mean values between the MR and echocardiographic measured parameters. The mean population value of the literature parameters listed in Table 6.8 do fall within the population range of the MR parameters though, taking into account both the random and the systematic uncertainties.

102121

6.3 LEFT VENTRICULAR CHAMBER LENGTH MEASUREMENTS

The first of the left ventricular chamber parameters to be presented in this chapter are the long axis chamber lengths. These measurements are made from long axis images beginning at the mitral valve plane and extending inferiorly to the ventricular chamber apex. The end diastolic and the end systolic chamber lengths were measured from the patient study described in Section 6.1. Thus the chamber lengths were measured from both the cardiac MR images and the echocardiographic images. These results are recorded in Appendix Table A.1. Comparisons of the cardiac MR measurements to the corresponding echocardiographic measurements are presented in plot form in Figure 6.4 and Figure 6.5.

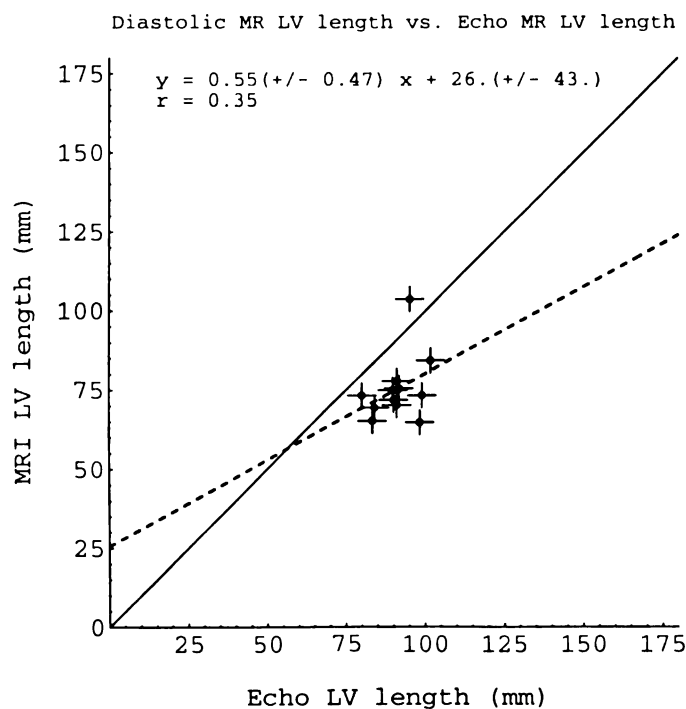


Figure 6.4 A comparison of the measured LV diastolic chamber lengths (as listed in Appendix Table A.1) from the cardiac MR images and the echocardiographic images. The dashed line is a least squares fit of the data to a straight line. The slope, intercept, and correlation coefficient of this line are listed at the top of the figure. The solid line represents an exact correlation between these two modalities.

102
103
104
105
106

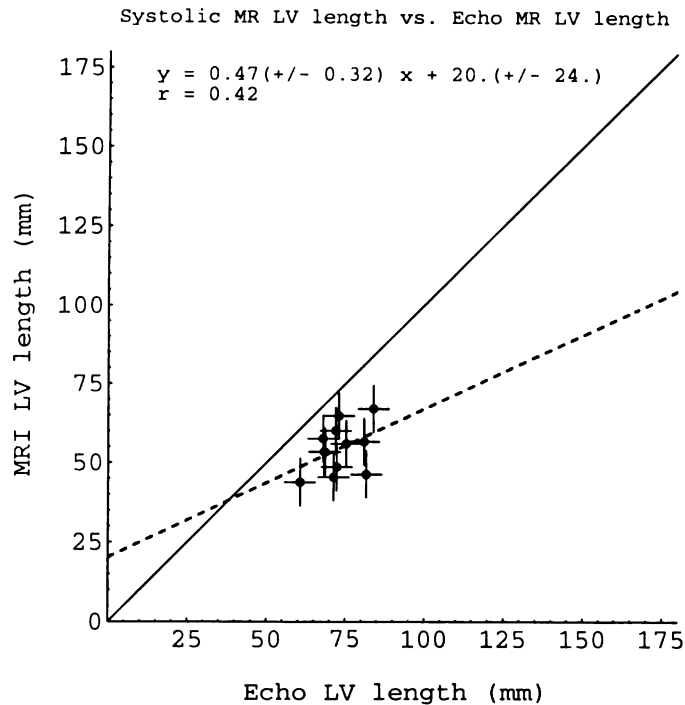


Figure 6.5 A comparison of the measured LV systolic chamber lengths from the cardiac MR images and the echocardiographic images.

The error bars in the data plots in this chapter and Chapter 7 are derived from patients A, B, C as described in Section 6.1. Also drawn in these plots are two lines. The first of these lines is solid and has a slope of one and intercept of zero. This is what would be expected from an exact correlation between the compared measurements. The second line is dashed and has a slope and intercept given by the least squares fit to a straight line of the data points in the plots. The equation of this line is presented at the top of each plot along with the correlation coefficient of this fit.

In Figure 6.4 the diastolic ventricular chamber lengths are systematically underestimated in the MR images relative to the echocardiographic images. This is expected due to the missed atrial kick in

102
LIBRARY

the MR images as discussed in Section 6.2.8. The systolic chamber lengths in Figure 6.5 are also systematically underestimated in the MR images. This underestimation is largely due to the poor contrast between the systolic chamber blood and the myocardium as described in Section 6.2.7.

USF LIBRARY

6.4 END DIASTOLIC LEFT VENTRICULAR CHAMBER VOLUME MEASUREMENTS

In this section the cardiac MR and the echocardiographic images from the previously described patient study are utilized to measure end diastolic chamber volumes. This parameter is measured using the summed multi-slice, the approximated biplane, and the approximated area length methods that were described in Section 6.2.1. Two separate summed multi-slice end diastolic volumes are measured from the cardiac MR images of each individual in the patient study. One comes from the long axis oblique images and the other comes from the short axis oblique images. The echocardiographic end diastolic volumes were measured using only the approximated biplane method. The results of all these end diastolic volume measurements are recorded in Appendix Table A.1. In the following figures the biplane MR volumes are compared to the echocardiographic biplane volumes, the long axis summed multi-slice volumes, and the short axis summed multi-slice volumes. In addition, the area length MR volumes are compared to the summed multi-slice volumes. The error bars and drawn lines in the following data plots were described in the previous section.

JOSE LIBRARY

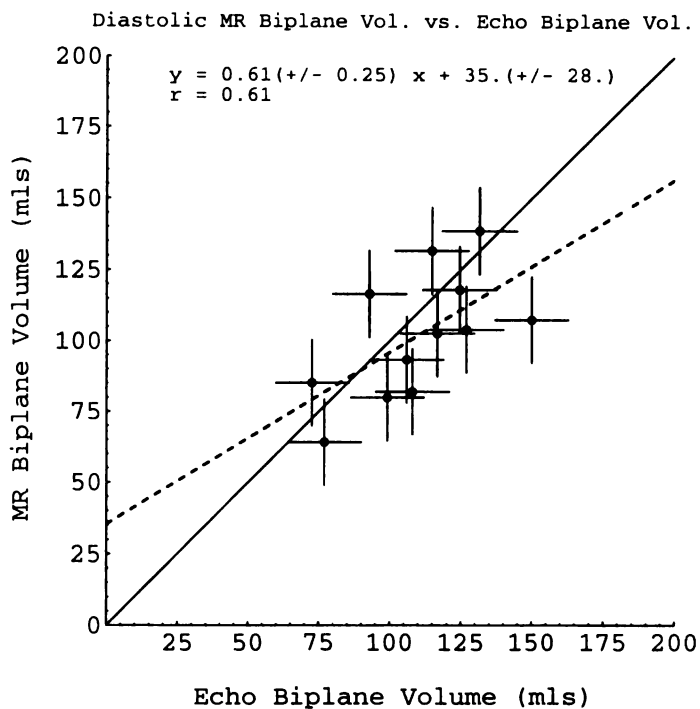


Figure 6.6 Comparison of the patient study (Section 6.1) end diastolic volumes as measured from long axis images by the MR biplane and the echocardiographic biplane methods.

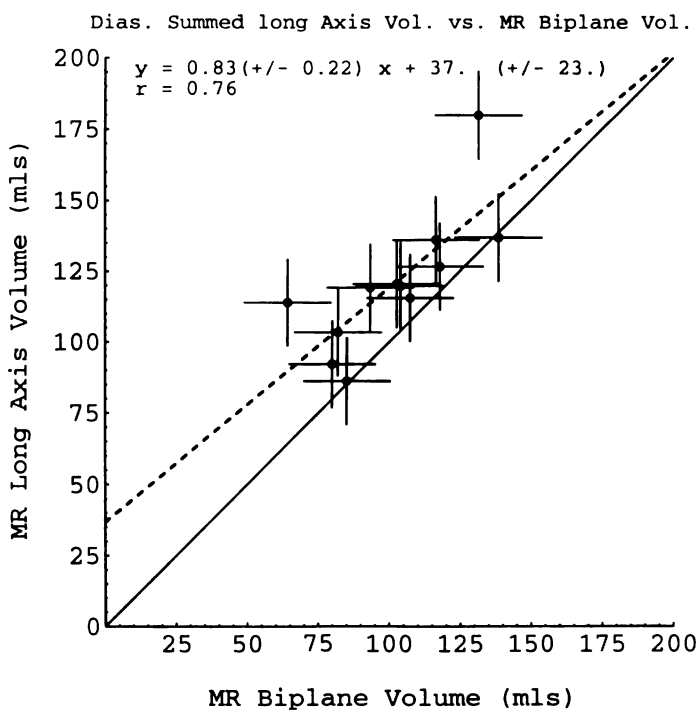


Figure 6.7 Comparison of the patient study end diastolic volumes as measured from the long axis MR images by the summed multi-slice and the biplane methods.

105 LBRM

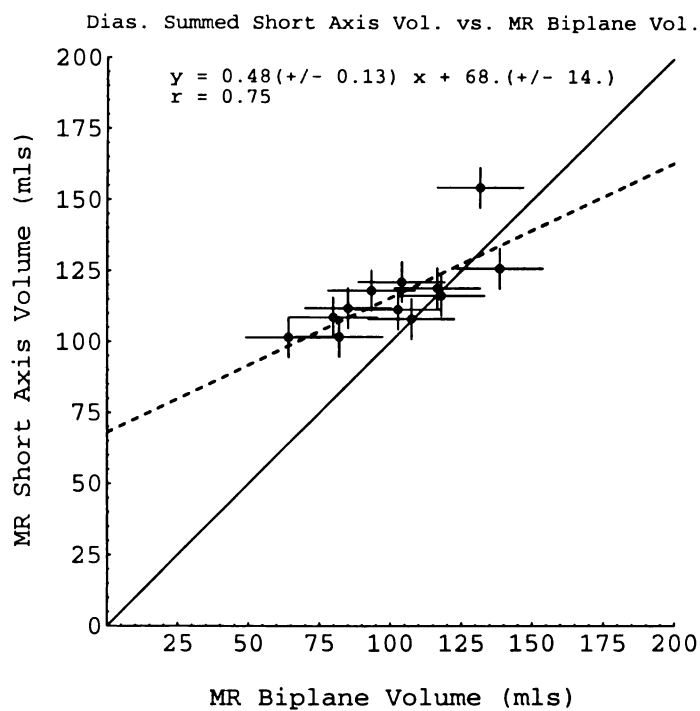


Figure 6.8 Comparison of the patient study end diastolic volumes as measured from the short axis MR images by the summed multi-slice method and from the long axis MR images by the biplane method.

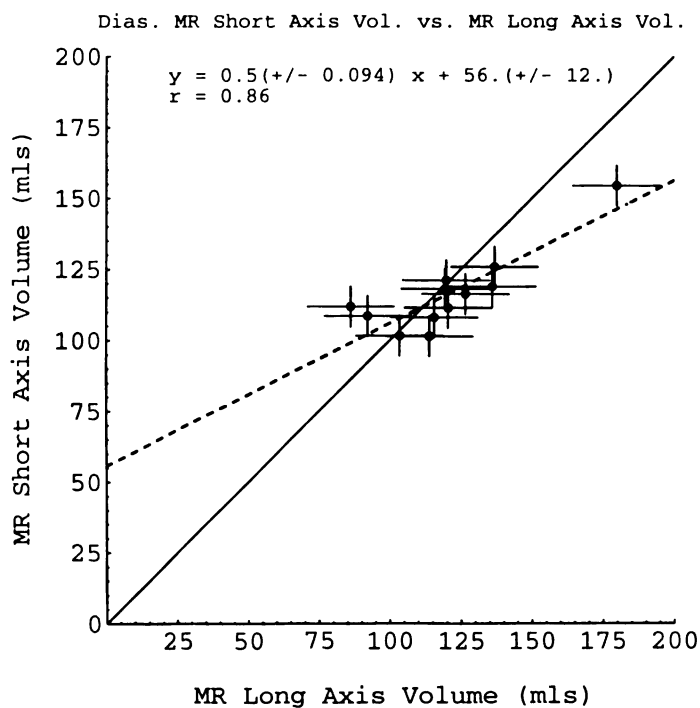


Figure 6.9 Comparison of the patient study end diastolic volumes as measured from the short axis MR images by the summed multi-slice method and from the long axis MR images by the summed multi-slice method.

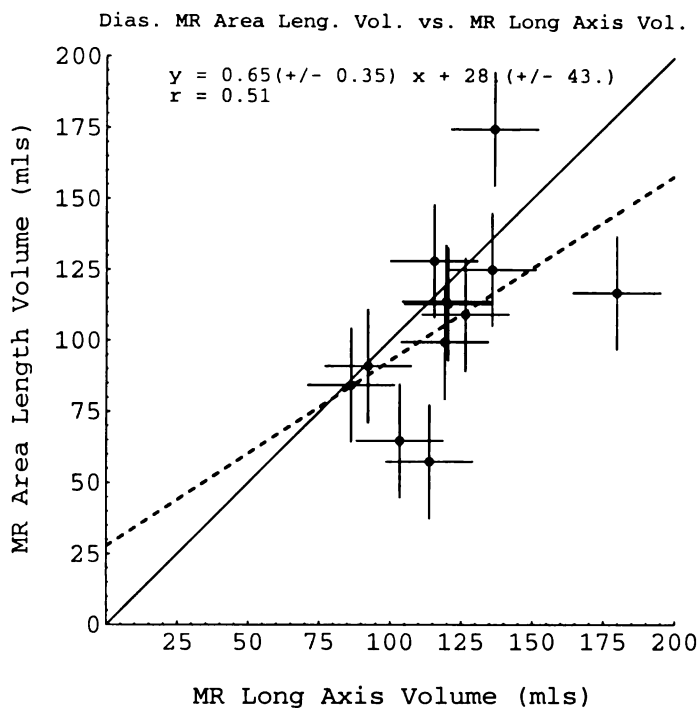


Figure 6.10 Comparison of the patient study end diastolic volumes as measured from the long axis MR images by the summed multi-slice method and from the two chamber long axis MR images by the area length method.

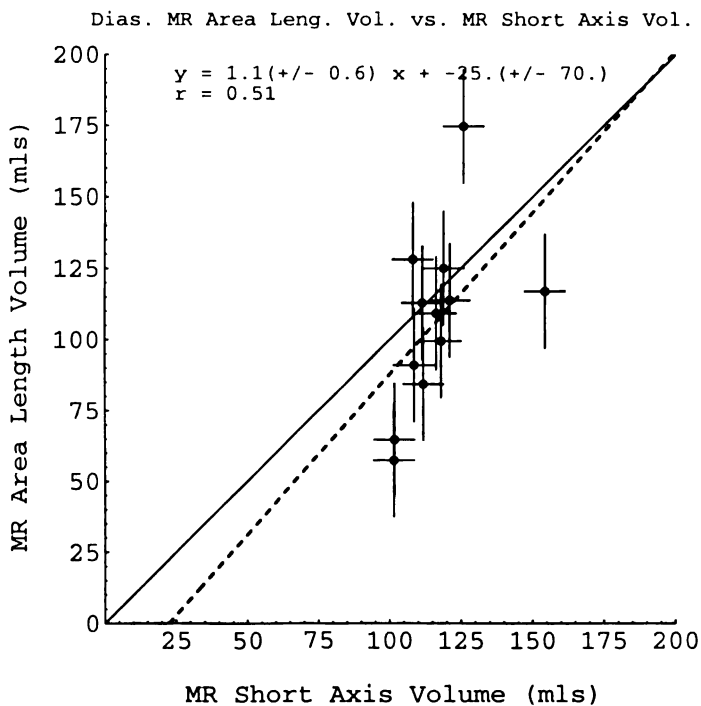


Figure 6.11 Comparison of the patient study end diastolic volumes as measured from the short axis MR images by the summed multi-slice method and from the two chamber long axis MR images by the area length method.

JOSE LIBRARY

The end diastolic volumes presented in Figure 6.6 through Figure 6.11 tend to be clustered within a narrow range. This is a result of the fact that the individuals included in the patient study are all young, healthy males. In Figure 6.6 the echocardiographic biplane volume measurements are presented. They are considered an accepted standard for this measured parameter [12]. The comparison in this figure shows a relatively close correspondence in the echocardiographic biplane measurements to the corresponding cardiac MR biplane measurements. Several of these measurements show an underestimated MR volume with respect to the echocardiographic volume. This result is likely due to the missed atrial kick in the MR images, as discussed in Section 6.2.8.

In Figure 6.7 and Figure 6.8 the MR summed multi-slice end diastolic ventricular volumes are compared to the corresponding approximated MR biplane volumes. These figures show that there is a systematic overestimation of both the long axis and the short axis summed volumes with respect to the MR biplane volumes. This is consistent with the model uncertainties of the MR biplane method that were described in Section 6.2.6. Comparing the long axis summed volumes to the short axis summed volumes in Figure 6.9 shows that on average the short axis volumes are systematically underestimated. This result is due to the boundary uncertainties described in Section 6.2.4. Since the long axis summed volumes do not contain this uncertainty they tend to correspond more closely to the MR biplane volumes, as is evident in Figure 6.7. Finally, note that the error bars in Figure 6.9 are larger for the long axis measured volumes than they are in the short axis volumes. This is consistent with

1021
1022
1023
1024
1025

larger random partial volume uncertainties in the long axis summed volumes as was described in Section 6.2.9.

Finally Figure 6.10 and Figure 6.11 compare the summed multi-slice MR diastolic volumes to the approximated MR area length volumes. These figures show that there is a systematic underestimation of the MR area length volumes relative to the summed multi-slice volumes. This is due to the model uncertainties that were described in Section 6.2.6. These figures also show that the area length measurements have a larger random variation than the corresponding biplane measurements. Therefore, of the two approximation methods the biplane method is preferred. This result agrees with the view presented in the literature that the biplane method is more accurate than the area length method [12].

6.5 END SYSTOLIC LEFT VENTRICULAR CHAMBER VOLUME MEASUREMENTS

In this section the systolic chamber volumes are measured in the same manner as was described in the previous section. The results of these end systolic volume measurements are recorded in Appendix Table A.1. In the following figures the biplane MR volumes are compared to the echocardiographic biplane volumes, the long axis summed multi-slice volumes, and the short axis summed multi-slice volumes. In addition, the area length MR volumes are compared to the summed multi-slice volumes. The error bars and drawn lines in the following data plots were described previously in Section 6.3.

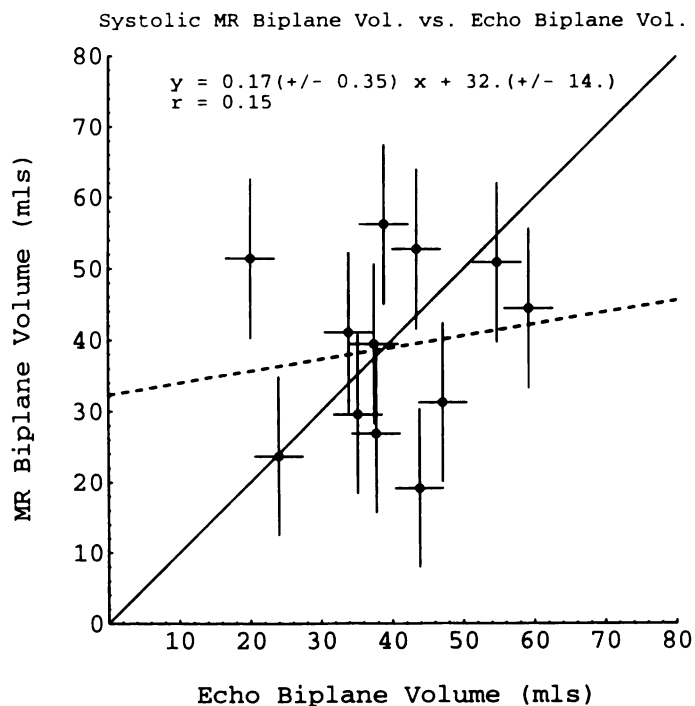


Figure 6.12 Comparison of the patient study (Section 6.1) end systolic volumes as measured from long axis images by the MR biplane and the echocardiographic biplane methods.

1951

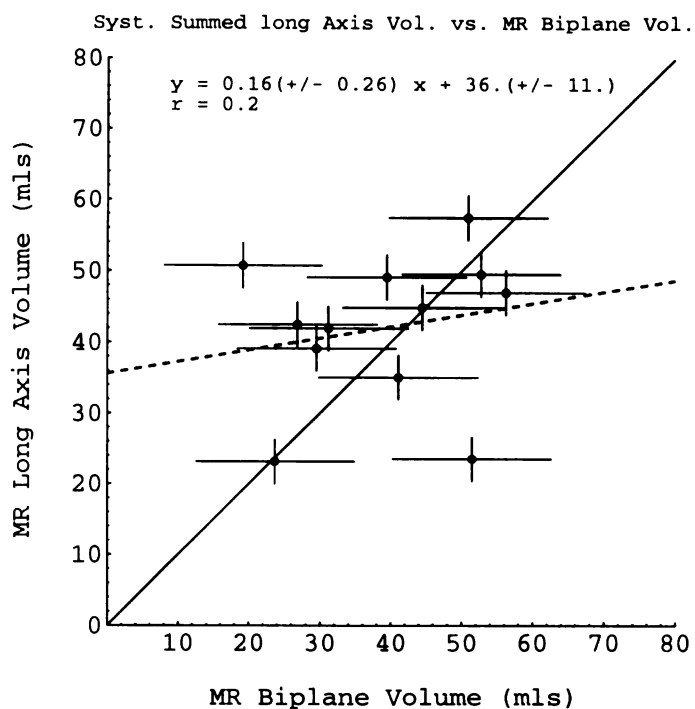


Figure 6.13 Comparison of the patient study end systolic volumes as measured from the long axis MR images by the summed multi-slice and the biplane methods.

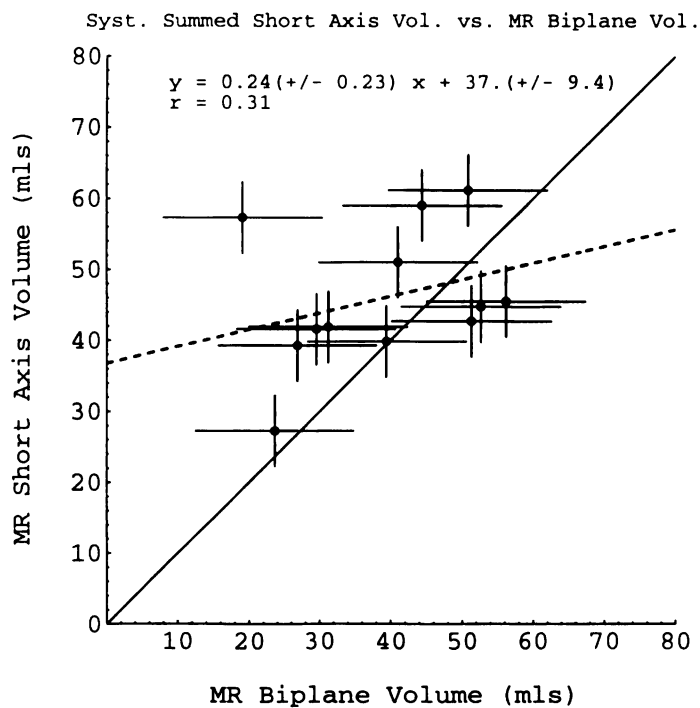


Figure 6.14 Comparison of the patient study end systolic volumes as measured from the short axis MR images by the summed multi-slice method and from the long axis MR images by the biplane method.

105131

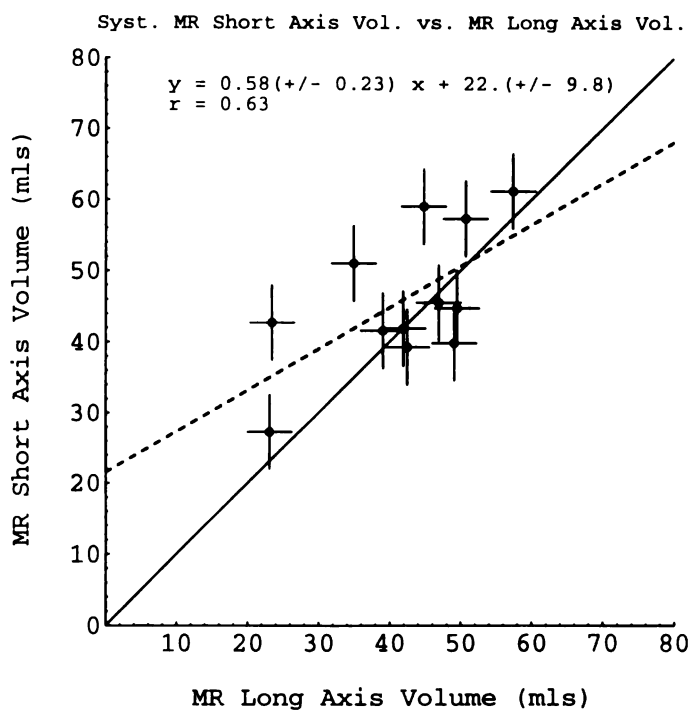


Figure 6.15 Comparison of the patient study end systolic volumes as measured from the short axis MR images by the summed multi-slice method and from the long axis MR images by the summed multi-slice method.

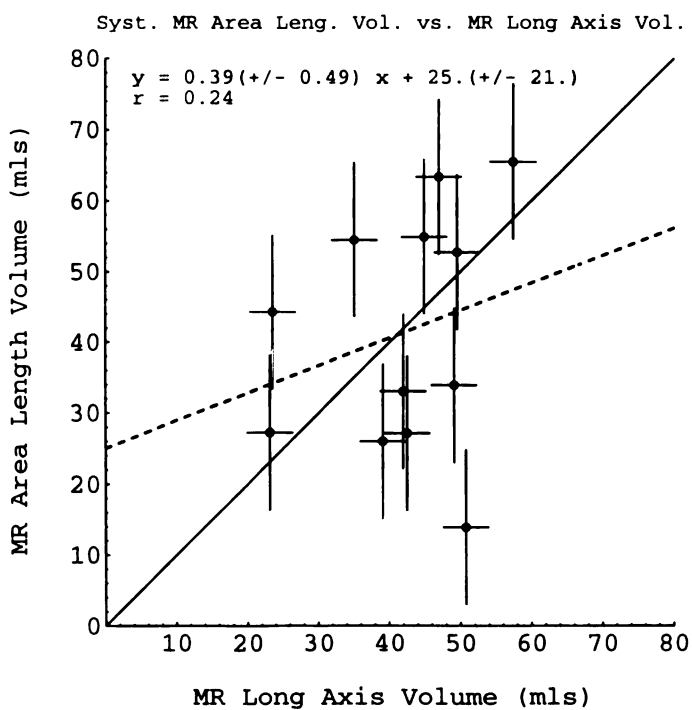


Figure 6.16 Comparison of the patient study end systolic volumes as measured from the long axis MR images by the summed multi-slice method and from the two chamber long axis MR images by the area length method.

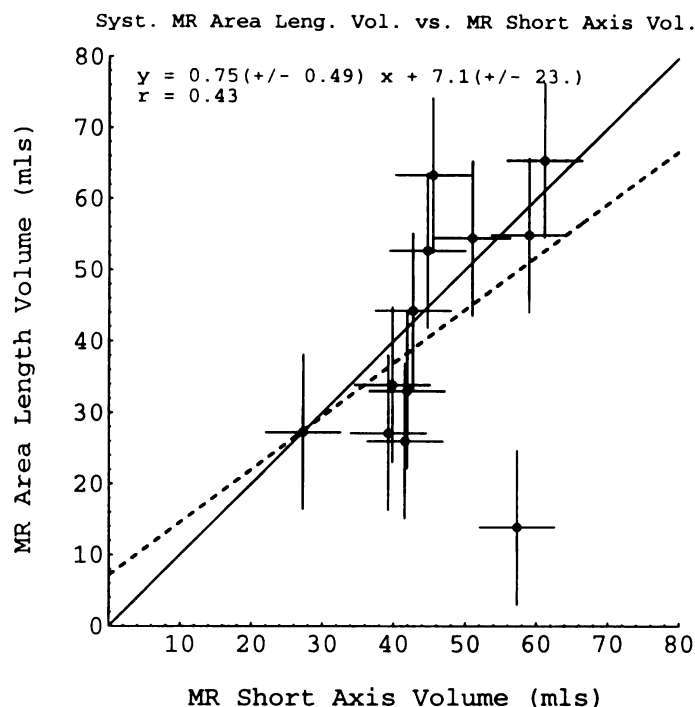


Figure 6.17 Comparison of the patient study end systolic volumes as measured from the short axis MR images by the summed multi-slice method and from the two chamber long axis MR images by the area length method.

In Figure 6.12 the comparison of the systolic cardiac MR biplane volume measurements to the systolic biplane echocardiographic measurements shows a relatively poor correspondence in these measured volumes. Judging by the error bars in this figure the random variations that cause this poor correspondence appear to arise mostly in the MR biplane volumes. This result is believed to be due to reduced contrast between the systolic blood and the myocardium in the MR images, as described in Section 6.2.7.

Figure 6.13 and Figure 6.14 show that the random variation in the MR biplane volumes is also larger than the random variation in the summed multi-slice volumes, as judged by the error bars in these plots.

102 12111

Since each of the systolic volumes represented in these two plots contain the systolic blood uncertainties, the disparity in these uncertainties is likely the result of the biplane model uncertainties described in Section 6.2.6.

In Figure 6.15 a comparison of the two summed multi-slice volumes shows that there is a relatively small amount of randomness in these measurements. Based upon the figure error bars this randomness appears to be balanced evenly between the two measurements, especially with respect to the diastolic summed volumes of Figure 6.9. Additional systematic variation is present in the summed short axis volumes as is evident in Figure 6.14 and Figure 6.15. This relative overestimation in the chamber volume occurs due to the boundary uncertainties described in Section 6.2.4.

Figure 6.16 and Figure 6.17 present a comparison of the summed multi-slice MR systolic volumes to the approximated MR area length volumes. The area length measurements in these figures differ from the summed volumes due to the previously described model uncertainties and, in the case of the short axis summed volumes, the boundary uncertainties. Despite the boundary uncertainties, the short axis summed systolic volumes corresponds fairly well to the area length volumes as is evident in Figure 6.17. This may be a chance result as the error bars in these figures indicate that the systolic area length measurements contain relatively large random uncertainties, similar to those found in the corresponding MR biplane measurements (Figure 6.13 and Figure 6.14).

JOSE LIBRARY

6.6 LEFT VENTRICULAR EJECTION FRACTION MEASUREMENTS

Ejection fraction (EF) measurements from the previously described patient study are presented in this section. Specifically, the biplane MR ejection fractions are compared to the echocardiographic biplane ejection fractions, the long axis summed multi-slice ejection fractions, and the short axis summed multi-slice ejection fractions. In addition, the area length MR ejection fractions are compared to the summed multi-slice ejection fractions. The error bars and drawn lines in the following data plots were described in Section 6.3. The healthy individuals that make up the patient study tend to have ejection fractions that fall within a relatively narrow range. This sometimes leads to inconsistent least squares fit lines as can be seen in Figure 6.18.

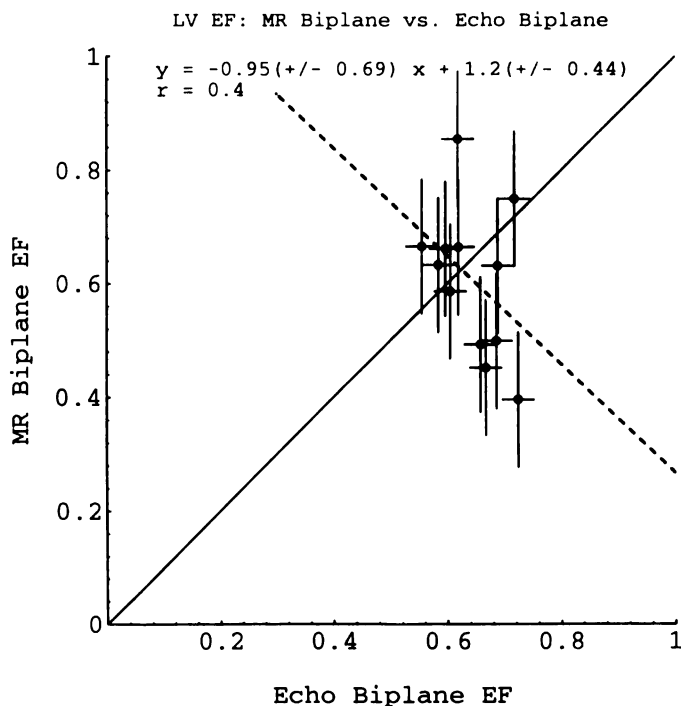


Figure 6.18 Comparison of the patient study (Section 6.1) ejection fractions as measured from long axis images by the MR biplane and the echocardiographic biplane methods.

1021 1021 1021

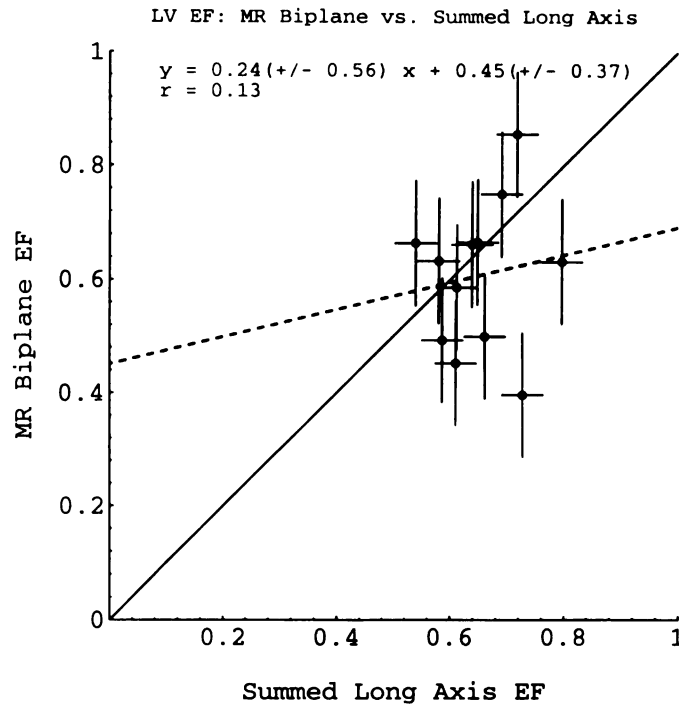


Figure 6.19 Comparison of the patient study ejection fractions as measured from the long axis MR images by the summed multi-slice and the biplane methods.

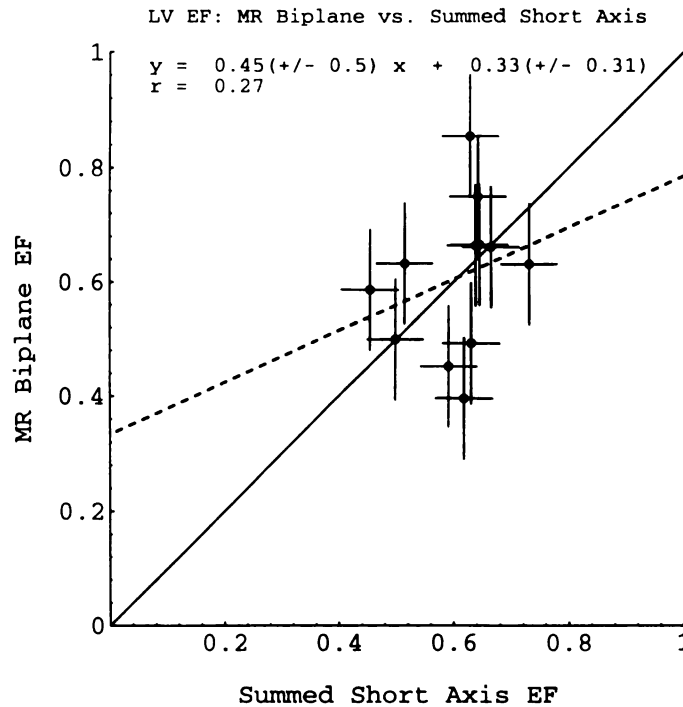


Figure 6.20 Comparison of the patient study ejection fractions as measured from the short axis MR images by the summed multi-slice method and from the long axis MR images by the biplane method.

1051241

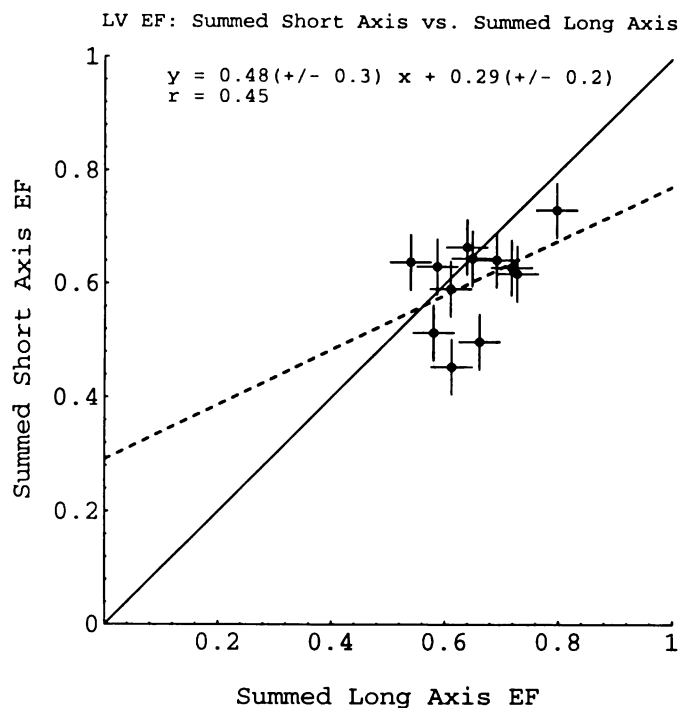


Figure 6.21 Comparison of the patient study ejection fractions as measured from the short axis MR images by the summed multi-slice method and from the long axis MR images by the summed multi-slice method.

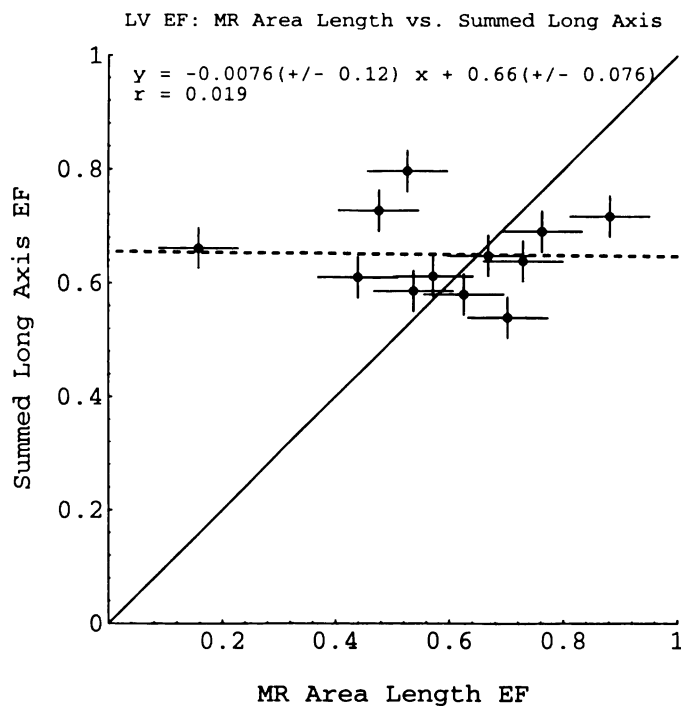


Figure 6.22 Comparison of the patient study ejection fractions as measured from the long axis MR images by the summed multi-slice method and from the two chamber long axis MR images by the area length method.

105 LDRN

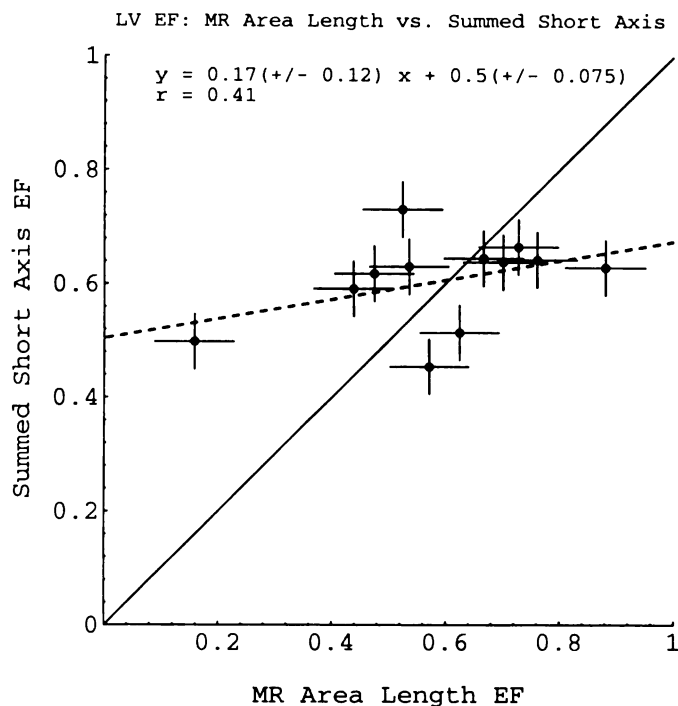


Figure 6.23 Comparison of the patient study ejection fractions as measured from the short axis MR images by the summed multi-slice method and from the two chamber long axis MR images by the area length method.

The ejection fraction measurements in the figures in this section carry with them the atrial kick, systolic blood, boundary, and partial volume uncertainties of their component end diastolic and end systolic volumes. This is apparent in the approximated parameters where the large random variation of the MR biplane and the MR area length chamber volumes result in similar random variation in the corresponding approximated ejection fractions. Relatively speaking, the summed multi-slice volumes were found to have small random variations. This results in summed multi-slice ejection fractions with similarly small random variations (Figure 6.21). Finally, the boundary uncertainties in the diastolic and systolic summed short axis volumes result in a systematic underestimation of the summed short axis ejection fractions relative to the long axis ejection fractions, as described in Section 6.2.4.

JOSE LIBRARY

6.7 CONCLUSION

The cardiac MR volumetric parameters presented in this chapter indicate that the summed multi-slice measurement methods are preferred over the approximated measurement methods. This is because the biplane and the area length approximated parameters contain significant random uncertainties relative to the summed multi-slice parameters. Choosing the multi-slice parameters over the approximated parameters is a tradeoff between improved accuracy versus expediency where accuracy is preferred. In these multi-slice measurements there is a slight preference for the short axis image orientations over the long axis image orientations. This is due to the increased partial volume uncertainties in the diastolic long axis summed multi-slice volumes as is evident in Figure 6.9 and described in Section 6.2.9.

1057 LIBRARY

CHAPTER 7

MEASUREMENT OF THE LEFT VENTRICULAR MYOCARDIAL MASS

In this chapter the cardiac MR and the echocardiographic images from the previously described patient study are used to measure the myocardial mass. This parameter is measured using the summed multi-slice, the truncated ellipsoid, and the area length methods that were described in Section 6.2.1. As in the previous chapter, the summed multi-slice myocardial mass is measured in both the long axis oblique images and the short axis oblique images. The echocardiographic myocardial mass was measured using only the truncated ellipsoid method. The results of these measurements are recorded in Appendix Table A.1 and compared in the following figures. The error bars and drawn lines in the following data plots were described previously in Section 6.3.

USF LIBRARY

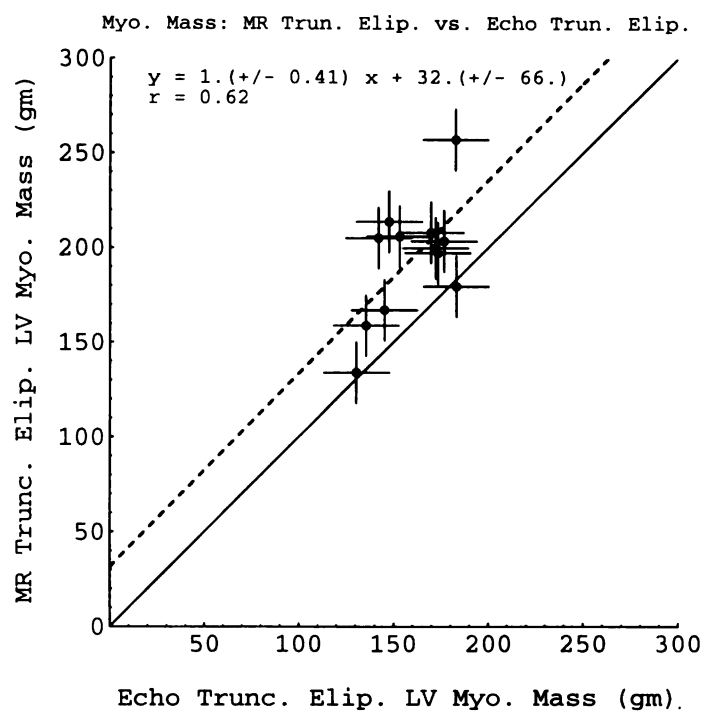


Figure 7.1 Comparison of the patient study (Section 6.1) myocardial mass as measured from long axis images by the MR truncated ellipsoid and the echocardiographic truncated ellipsoid methods.

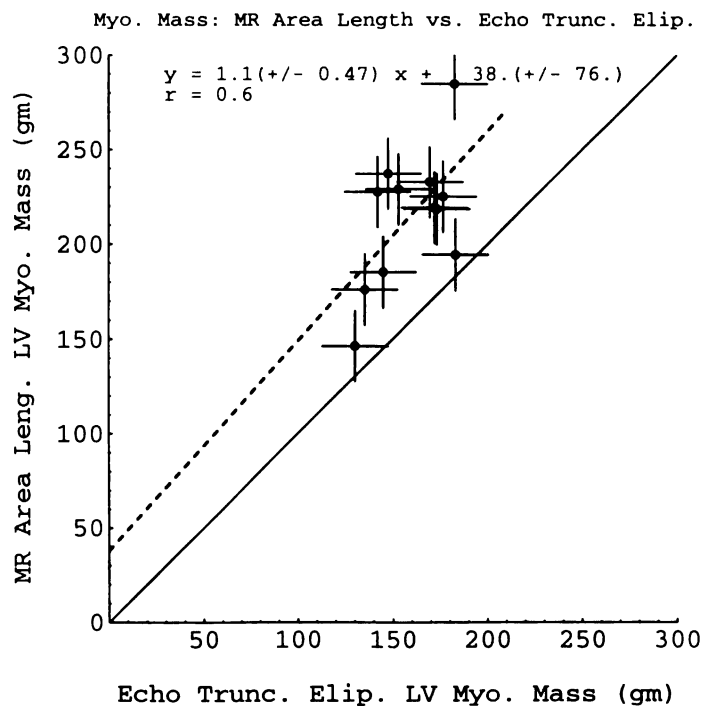


Figure 7.2 Comparison of the patient study myocardial mass as measured from long axis images by the MR area length and the echocardiographic truncated ellipsoid methods.

1057 LIBRARY

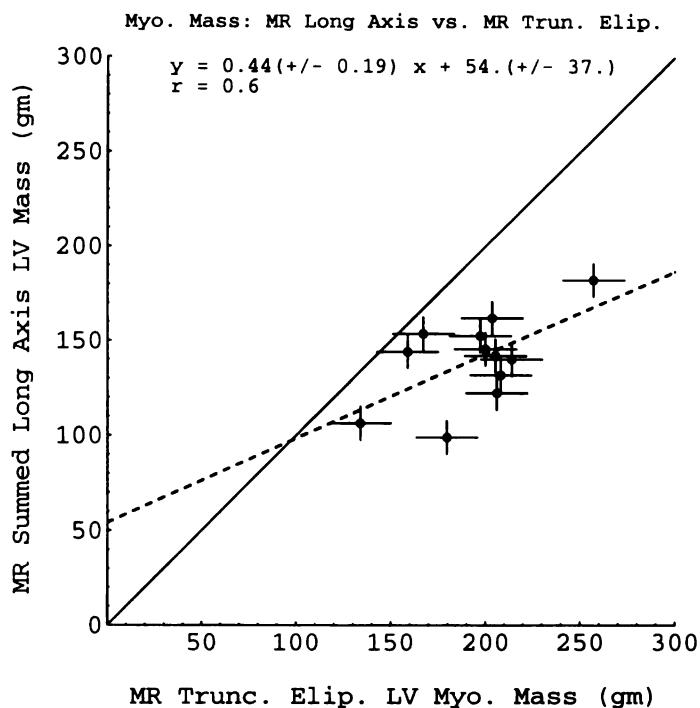


Figure 7.3 Comparison of the patient study myocardial mass as measured from long axis MR images by the summed multi-slice and the truncated ellipsoid methods.

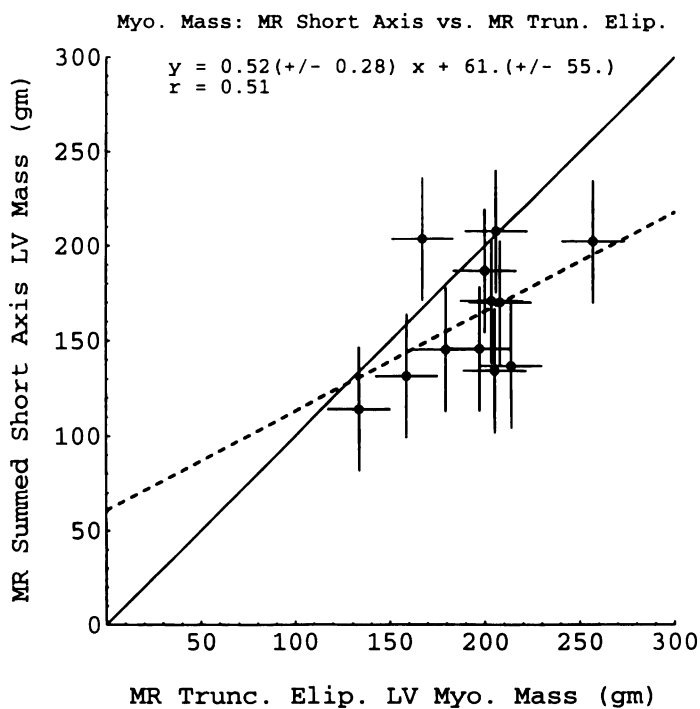


Figure 7.4 Comparison of the patient study myocardial mass as measured from short axis MR images by the summed multi-slice method and from long axis MR images by the truncated ellipsoid method.

JOSE LIBRY

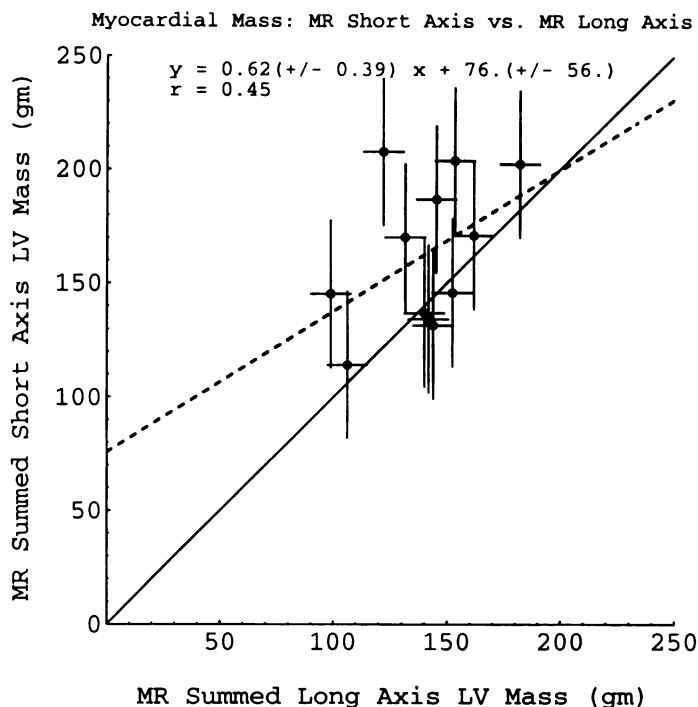


Figure 7.5 Comparison of the patient study myocardial mass as measured from short axis and long axis MR images by the summed multi-slice method.

The first two figures in this chapter compare the approximated MR myocardial mass measurements to the echocardiographic truncated ellipsoid measurements. This comparison shows that the approximated MR parameters overestimate the myocardial mass relative to the echocardiographic measurements. Since these approximated measurements are based upon similar models this is largely the result of the atrial kick uncertainties described in Section 6.2.8. The error bars in these figures indicated that the random variation in the approximated MR measurements is similar in magnitude to the random variation of the echocardiographic truncated ellipsoid measurements.

The remaining figures compare the summed multi-slice long axis and short axis myocardial mass measurements to each other and to the

JOSE LIBRARI

measured MR truncated ellipsoid mass. These figures show a substantial systematic and random variation between the summed multi-slice mass and the truncated ellipsoid mass. Since the atrial kick uncertainty is consistent in both measurement methods the likely source for the systematic uncertainties is the model uncertainties described in Section 6.2.6. The random variation in the long axis summed multi-slice mass is relatively small compared to the corresponding short axis multi slice mass as is evident in the direct comparison of Figure 7.5. The only significant difference in these two measurements is the boundary uncertainty described in Section 6.2.4. Hence this is the likely source for the additional random variation in the short axis multi-slice mass measurements.

The above discussion suggests that the approximation methods are preferred for measuring the myocardial mass from MR images due to their small random variation relative to the summed multi-slice measurements. Of the approximated mass measurements the truncated ellipsoid mass is preferred because it is commonly utilized in echocardiographic cardiac functional analysis [12].

JOSE LIBRARY

CHAPTER 8

ANALYSIS OF THE LEFT VENTRICULAR MYOCARDIAL WALL THICKENING AND MOTION

Quantifying myocardial contractility is an important goal of cardiac functional analysis as related in Section 2.5. In comparison to the volumetric functional parameters, myocardial contractility is a regionally specific functional parameter where each measurement is associated with a particular portion of the myocardium. The advantage that regional functional measurements have is that they can often identify a myocardial disease state before any outward physical symptoms are evident. Unfortunately it is not possible to acquire a measurement of myocardial contractility directly. Instead it is common to acquire functional parameters which indirectly are related to the myocardial tissue contractility. Two such functional measurements are: the myocardial wall thickening and the myocardial wall motion. These cardiac functional measurements were discussed in detail in Section 2.5.

In order to demonstrate how these functional parameters are implemented in cardiac MR images a single cardiac MR acquisition was selected from the previously described cardiac patient study. From this study a centered cine oblique short axis slice of the left ventricle was selected. The myocardial wall thickening and the myocardial wall motion were measured for an abbreviated set of this slice's cine images. By abbreviated it is meant that every other image slice from the cardiac cine was selected for presentation here. These images are presented in Figure 8.1. The end diastolic image is Frame #13 and the end systolic

JOSE LIBRARY

image is Frame #9. Notice that in the systolic image frames (#5 - #9) there is an increased MR signal from the ventricular blood. This signal blends in with the MR signal from the myocardium making the definition of the endocardial boundary rather difficult. In order to overcome this problem the endocardial boundary is defined with reference to a cine loop of the temporal images taken over the cardiac contraction cycle at this slice position. The endocardial boundary is determined by following the motion of the endocardium and the increasing signal from blood from slice to slice in order to differentiate these two tissues in the systolic image frames. The resultant endocardial boundaries are illustrated in Figure 8.2.

Extra-cardiac motion can be present in the cardiac images as a result of either patient motion or magnetic field drift in the case of low field MR images. This causes registration inconsistencies in sequential temporal image frames. To deal with these inconsistencies a floating reference frame is used that bases the myocardial measurements on the myocardial center of mass for the wall thickening measurements and the endocardial boundary center of mass for the wall motion measurements.

The myocardial wall thickness in each image frame can be determined by measuring the radial distance from the endocardial boundary to the epicardial boundary. Figure 8.2 displays both of these boundaries for each of the cine image frames from Figure 8.1. The first step in the measurement of wall thickness is to calculate the location of the myocardial center of mass in each image. Radial lines are then drawn from the center of mass out to the epicardial boundary throughout the entire short axis cross-section. The wall thickness is defined to be the radial

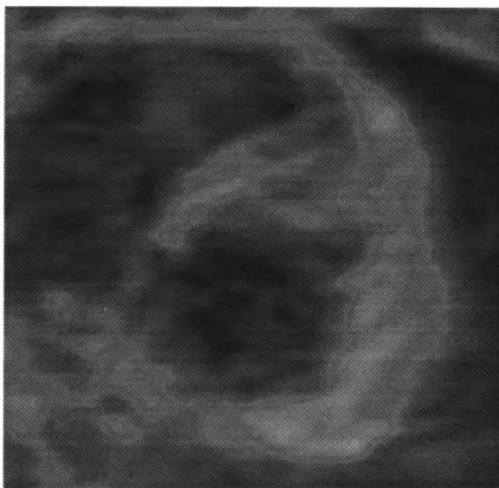
JOSE LIBRARY

distance along these lines from the intersection of the endocardial boundary to the intersection of the epicardial boundary. These radial lines are drawn into Figure 8.2 and the radial distances were determined and then plotted versus rotation angle in Figure 8.4 (a). These plots of wall thickness can be compared to each other in order to assess the myocardial wall thickening that occurs during cardiac contraction. Such a comparison is presented in Figure 8.5 (a) where the end diastolic image, Frame #13, is selected and the difference between this frame's wall thickness and each of the remaining cine image frames' wall thickness is calculated and plotted.

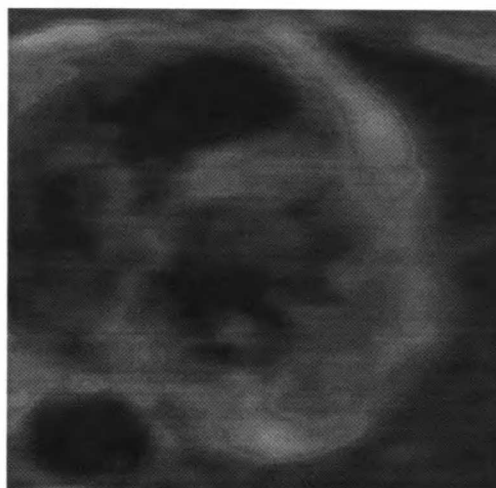
In many cardiac imaging modalities, such as echocardiography, the epicardial boundary is not always distinguishable. In these cases it is not possible to acquire a measurement of the myocardial wall thickening. Instead it is common to measure the myocardial motion that occurs during the cardiac contraction cycle. This measurement is performed by tracking the relative change in the position of the endocardial boundary as it moves during cardiac contraction. In order to quantify this motion the center of mass of the endocardial boundary is determined and the distance from this center of mass to the endocardial boundary is measured throughout the entire short axis cross-section. An example of these radial distance measurements for the selected cardiac cine images is presented in Figure 8.3 along with plots of this radial distance in Figure 8.4 (b). The myocardial wall motion, with respect to the endocardium, can then be determined by a relative comparison of the radial distance from a selected cine frame to the radial distance of the remaining cine image frames. In Figure 8.5 (b) this comparison of myocardial wall motion is presented relative to the radial distance of the end diastolic cine image in Frame #13.

Comparing the plots in Figure 8.5 of the myocardial wall thickening and the myocardial wall motion it is apparent that the wall thickening plots contain information that is not included in the myocardial mass measurements. This can be seen in Figure 8.5 where there are myocardial regions that show a change in the wall thickness but that do not show a corresponding change in the myocardial motion through the temporal sequence of figures. This is a logical result of the increased information provided by the inclusion of the epicardial boundary in the wall thickening plots. This is the reason why the wall thickening plots are the preferred method for assessing myocardial contractility. In this regard it is advantageous to utilize cardiac MR imaging as compared to echocardiography. This is because it is often time very difficult to define the epicardial boundary in echocardiographic images and therefore only the myocardial wall motion is available from this imaging modality.

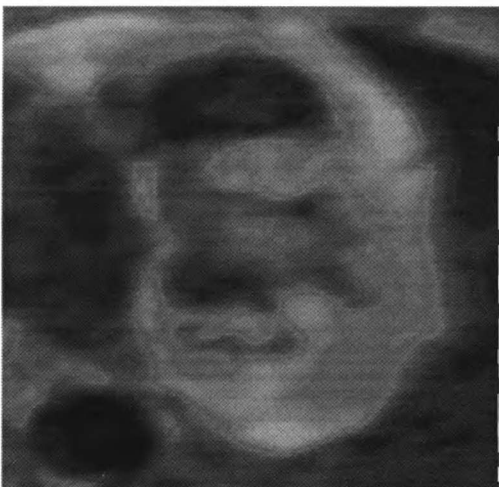
420467 Frame #3



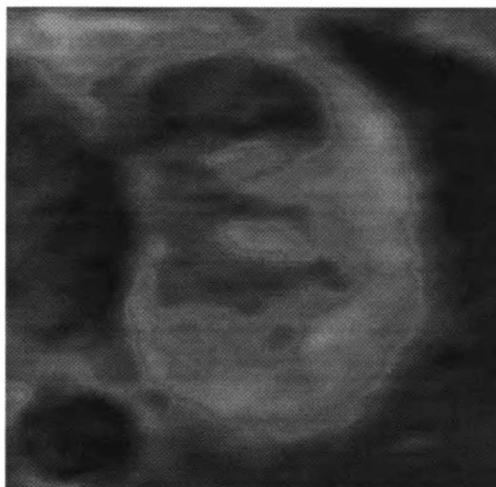
420467 Frame #5



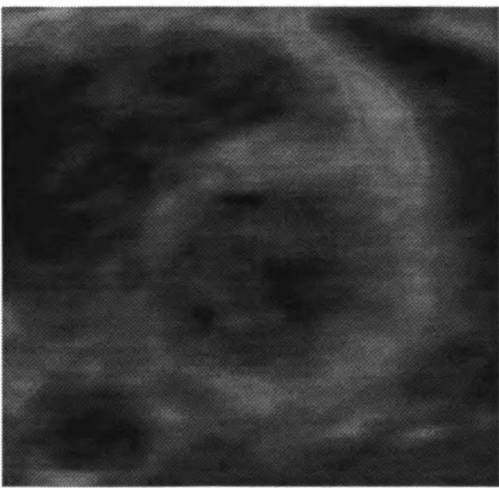
420467 Frame #7



420467 Frame #9



420467 Frame #11



420467 Frame #13

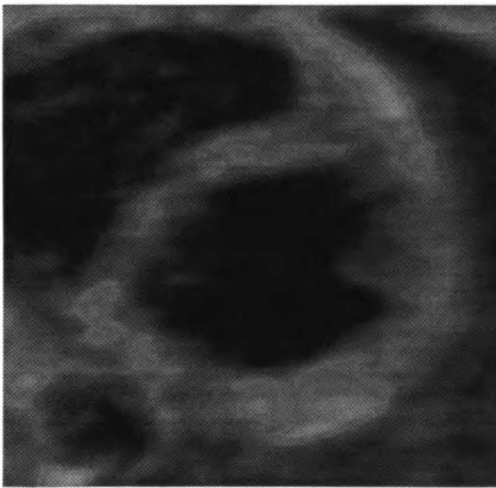
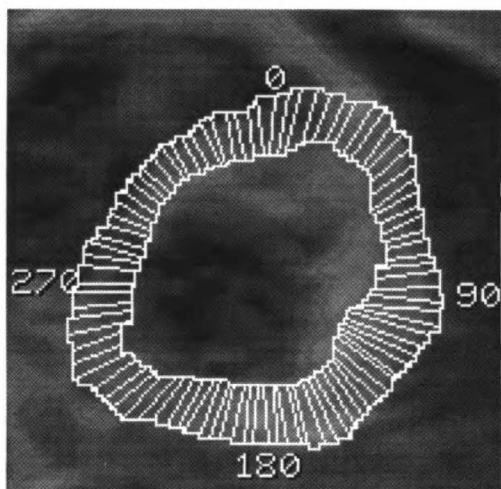
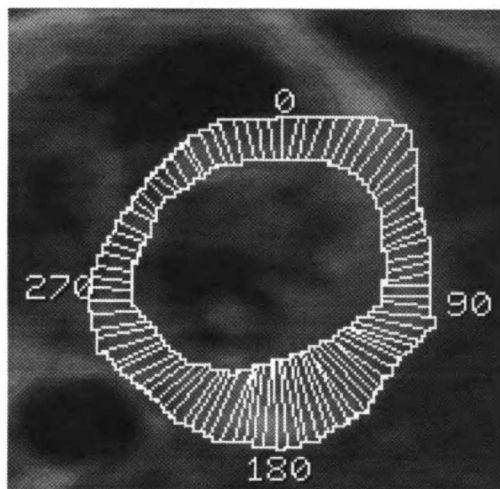


Figure 8.1 Abbreviated single slice short axis cardiac cine. (diastolic = #13, systolic = #9)

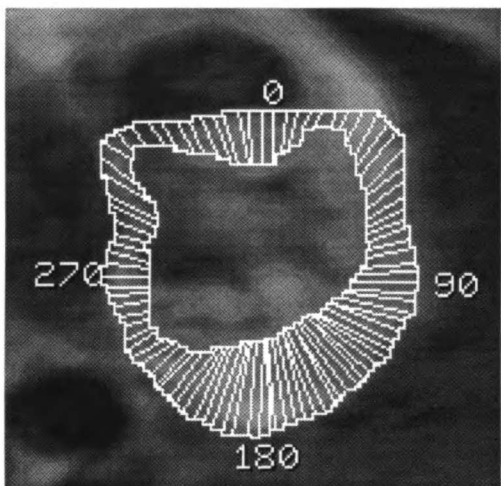
420467 Frame #3



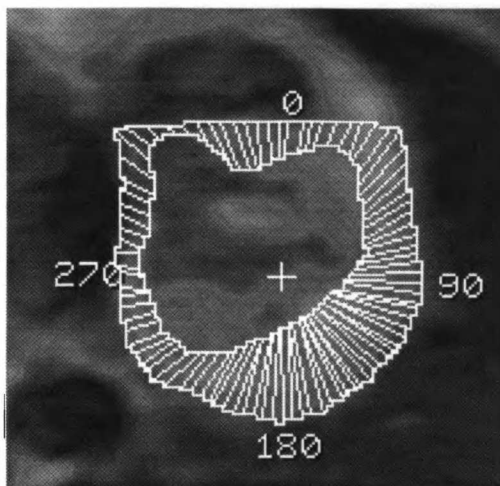
420467 Frame #5



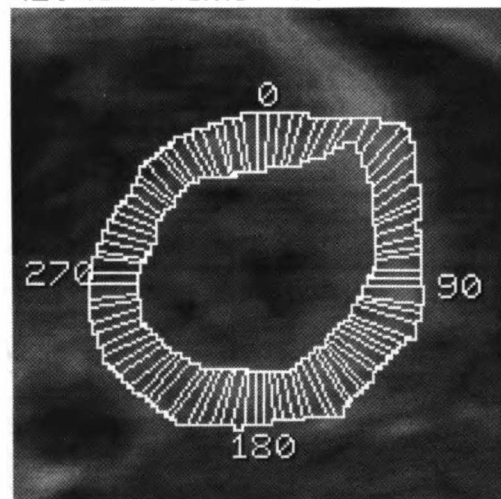
420467 Frame #7



420467 Frame #9



420467 Frame #11



420467 Frame #13

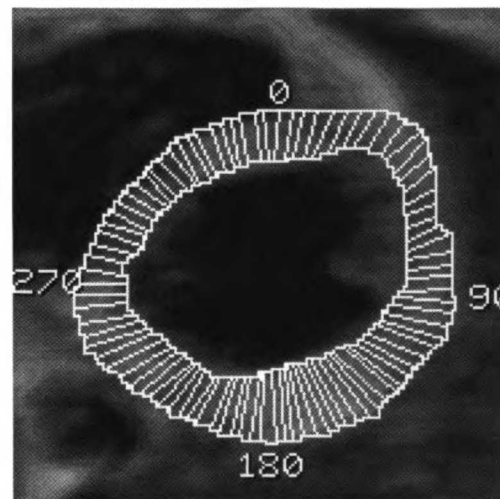
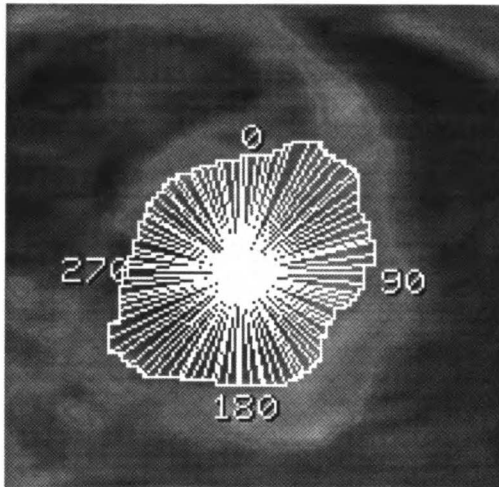
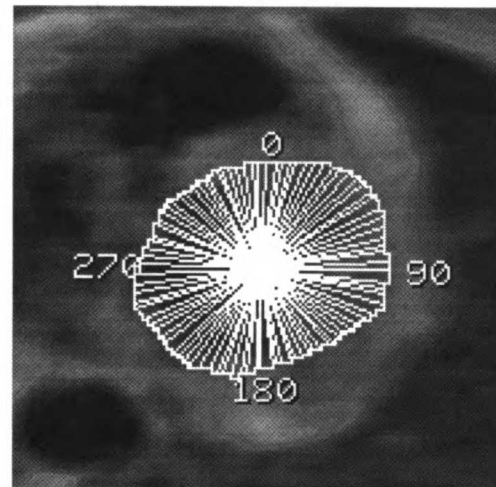


Figure 8.2 Wall thickness measurement on the abbreviated single slice short axis cardiac cine.

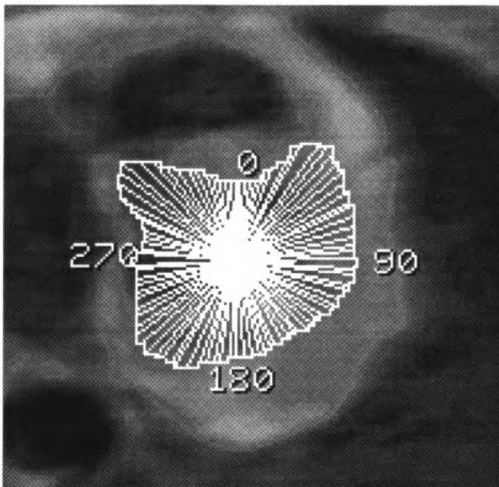
420467 Frame #3



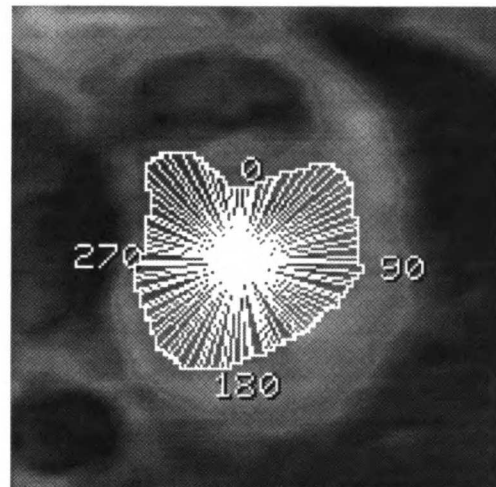
420467 Frame #5



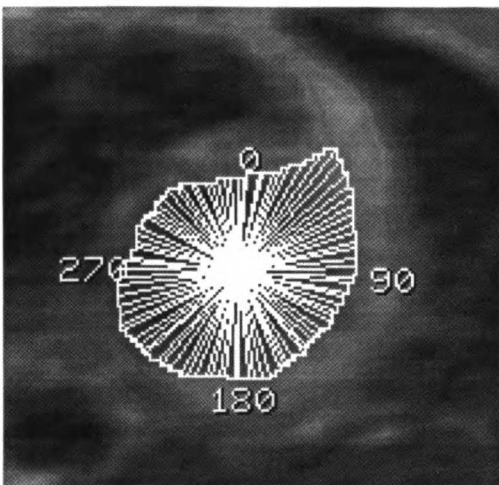
420467 Frame #7



420467 Frame #9



420467 Frame #11



420467 Frame #13

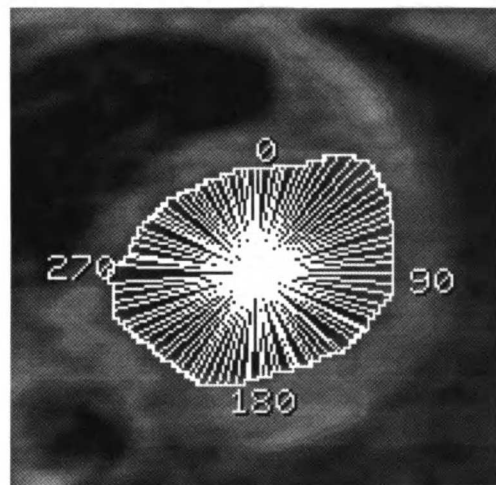


Figure 8.3 Example of endocardial radial distance measurement on the Figure 8.1 cine images.

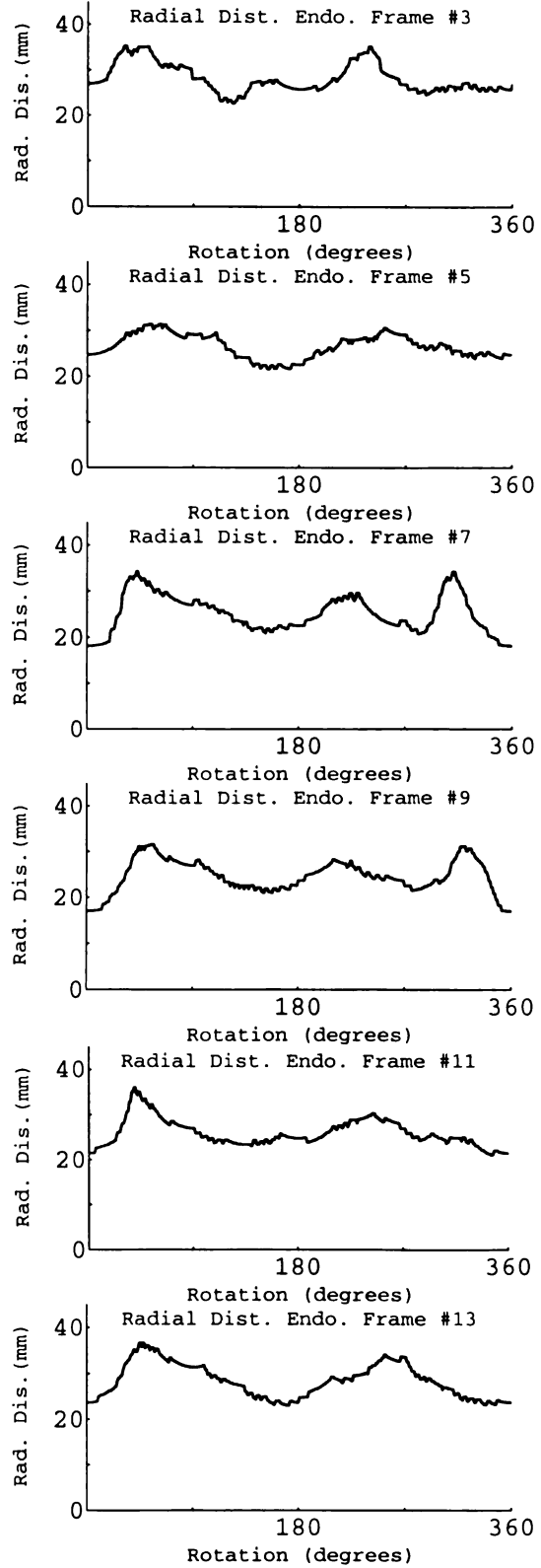
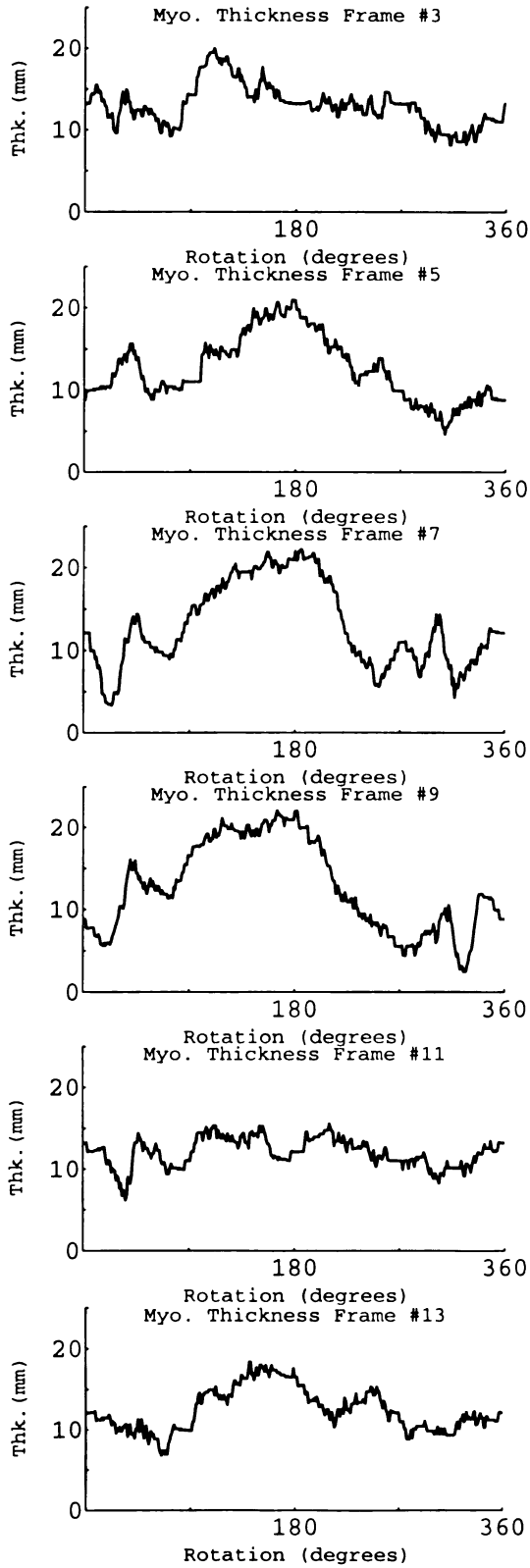


Figure 8.4 (a) Myocardial wall thickness.

Figure 8.4 (b) Radial distance: center mass - endoc.

These plots present the linear measurements from Figure 8.2 and Figure 8.3. Radial distance in Figure 8.4(b) is measured from the myocardial center of mass to the endocardial boundary.

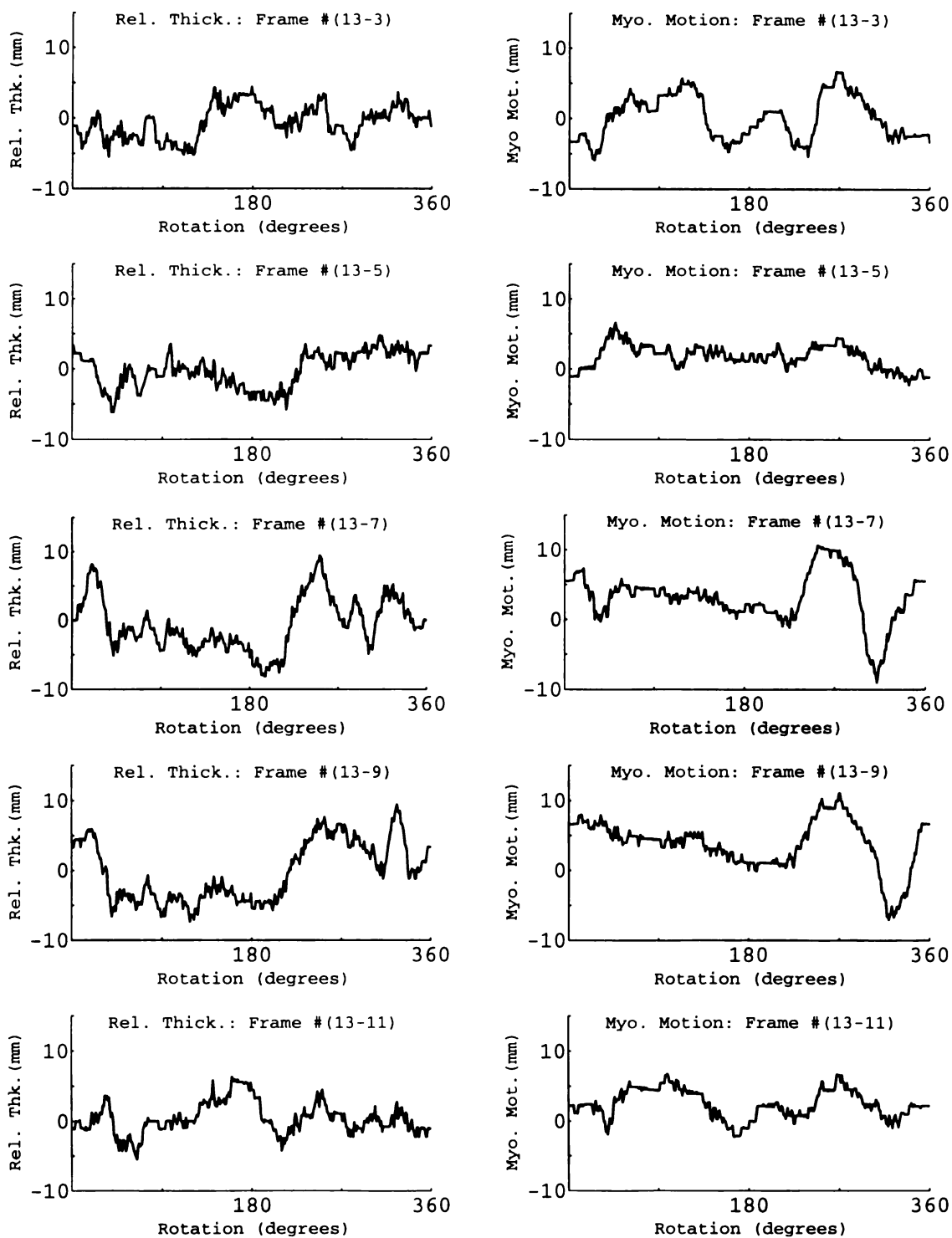


Figure 8.5 (a) Myocardial wall thickening.

Figure 8.5 (b) Myocardial wall motion.

These two sets of plots represent the relative change in wall thickness and endocardial radial distance from the center of mass for the cine images in Figure 8.2 and Figure 8.3. In both cases a relative measurement is created by subtracting the indicated image frame's wall thickness or radial distance from that of Frame # 13.

CHAPTER 9

CONCLUSION

The goal of this dissertation has been to investigate low field magnetic resonance imaging as a technique for assessing cardiac function. Low field cardiac images are of interest because they are known to have an increased immunity, relative to higher field cardiac MR images, from phase encode artifacts that are caused by inconsistencies in the gated MR acquisition time TR. Another advantage of low field MR imaging devices is that their manufacturing and operating costs are significantly lower than those of the higher field MR imaging devices. Low field magnetic resonance images have a lower signal to noise ratio as compared to higher field magnetic resonance images. This difference is partially compensated by changes in relaxation parameters and other imaging strategies. Additional compensation is provided by the temporal filtering methods discussed in this dissertation. This filter significantly reduces the stochastic noise present in these low field cardiac MR images giving a noticeable improvement in their image quality.

In this dissertation several methods were presented for measuring the cardiac functional parameters. Of these methods the approximated cardiac functional parameters require that the cardiac images be aligned along the cardiac long and short axes. In order to satisfy this requirement it is necessary to retrospectively reorient the cardiac MR images using the method presented in Chapter 5.

All of the parameter measurement methods discussed in this dissertation contain both systematic and random uncertainties. The systematic uncertainties are undesired but overall do not impact the utility of the cardiac functional parameter assessments as long as these assessments are performed in a consistent manner. Chapter 6 shows that the random parameter uncertainties are within the range of the population variation in healthy individuals. Therefore it is possible to utilize the low field cardiac MR images to make clinically relevant assessments of cardiac function.

Improvement in the cardiac MR parameter measurements may be achieved by reducing both the systematic uncertainties and the random uncertainties. Random partial volume uncertainties can be reduced by reducing the acquisition voxel dimensions, particularly along the slice axis. This will require an increase in the number of acquired image slices resulting in an increase in the acquisition time of the imaging procedure. Systematic uncertainties can be reduced by first enhancing the contrast between the systolic blood and the myocardium. Next, the gated imaging procedure can be expanded to capture the end diastolic images after the atrial kick. This can be accomplished through a retrospective gating method discussed in reference [42]. Finally, summed multi-slice parameters should be utilized as much as possible as they contain no systematic model uncertainties.

Many of the results presented in this dissertation have implications that go beyond the current focus on low field magnetic resonance imaging. Echocardiographic techniques for example are rapidly evolving to the point

where it will soon be possible to acquire multi-slice tomographic images from specialized trans-esophageal echocardiographic probes. These tomographic cine echocardiographic images will have several characteristics in common with the low field cine cardiac MR images which were discussed in this dissertation. First, they both have a need for image enhancement filters such as the temporal filter presented here. Second, they both require that the acquired images be retrospectively reoriented so as to produce images that are oriented along the cardiac long axis and the cardiac short axis. Finally, cardiac functional parameters can be acquired from these tomographic cardiac images by either measured methods or approximated methods. Therefore it is hoped that the work presented in this dissertation contributes to the advancement of not only the cardiac magnetic resonance imaging devices but also to the advancement of other imaging devices as well.

BIBLIOGRAPHY

- [1] Hurst, J. W., *The Heart, Arteries and Veins*, McGraw-Hill Information Services Company, New York, 1990.
- [2] *Proceedings of the Society of Magnetic Resonance in Medicine, 1991, 10th Annual Scientific Meeting and Exhibition*, Society of Magnetic Resonance in Medicine, Berkeley, CA, 1991.
- [3] *Proceedings of the Society of Magnetic Resonance in Medicine, 1992, 11th Annual Scientific Meeting and Exhibition*, Society of Magnetic Resonance in Medicine, Berkeley, CA, 1992.
- [4] *Proceedings of the Society of Magnetic Resonance in Medicine, 1993, 12th Annual Scientific Meeting and Exhibition*, Society of Magnetic Resonance in Medicine, Berkeley, CA, 1993.
- [5] Morganroth, J., Parisi, A., Pohost, G., *Noninvasive Cardiac Imaging*, Year Book Medical Publishers, Chicago, 1983.
- [6] Moore, Keith L., *Clinically Oriented Anatomy*, Williams & Wilkins, Baltimore, MD, 1985.
- [7] Jacob, Stanley W., *Structure and Function in Man*, W.B. Saunders Company, Philadelphia, 1982.
- [8] Cheitlin, Melvin D., et al., *Clinical Cardiology*, Appleton & Lange, Norwalk, Connecticut, 1993.
- [9] Marcus, Melvin L. ed., *Cardiac Imaging: A Companion To Braunwald's Heart Disease*, W.B. Saunders Company, Philadelphia, 1991.
- [10] Come, Patricia, *Diagnostic Cardiology, Noninvasive Imaging Techniques*, J.B. Lippincott Company, Philadelphia, 1985.

- [11] Peshock, Ronald M, "Magnetic Resonance Imaging of the Heart: Quantitation", published in: *Cardiac Imaging: A Companion To Braunwald's Heart Disease*, ed Marcus, Melvin,L., W.B. Saunders Company, Philadelphia, 1991.
- [12] Schiller, Nelson B., et al, "Recommendations for Quantitation of the Left Ventricle by Two-Dimensional Echocardiography", *Journal of the American Society of Echocardiography*, vol 2:5, pp. 358-367, 1989.
- [13] Force, Thomas L., et al, "Echocardiographic Assessment of Ventricular Function", published in: *Cardiac Imaging: A Companion To Braunwald's Heart Disease*, ed Marcus, Melvin, L., W.B. Saunders Company, Philadelphia, 1991.
- [14] Maier, SE, et al, "Acquisition and evaluation of tagged magnetic resonance images of the human left ventricle", *Computerized Medical Imaging and Graphics*, vol 16:21, pp. 73-80, 1992.
- [15] Clayman, Charles ed., *The American Medical Association Encyclopedia of Medicine*, Random House, New York, 1989.
- [16] Kaufman, Leon, et al., *Nuclear Magnetic Resonance Imaging in Medicine*, Igaku-Shoin, New York, 1981.
- [17] Budinger, Thomas F., et al., *Medical Magnetic Resonance, A Primer-1988*, Society of Magnetic Resonance in Medicine, Berkeley, CA, 1988.
- [18] Farrar, T., Becker, E., *Pulse and Fourier Transform NMR*, Academic Press, New York, 1971.
- [19] Mansfield, P., Morris, P., *NMR Imaging in Biomedicine*, Academic Press, Orando, Florida, 1982.

- [20] Fukushima, R., *Experimental Pulse NMR - A Nuts and Bolts Approach*. Addison-Wesley, Reading, MA, 1981.
- [21] Morris, P., *Nuclear Magnetic Resonance Imaging in Medicine and Biology*, Clarendon Press, Oxford, 1986.
- [22] Partain, C. Leon, et al., *Magnetic Resonance Imaging*, W.B. Saunders Company, Philadelphia, 1988.
- [23] Feynman, Richard P., *The Feynman Lectures on Physics*, Addison-Wesley Publishing Company, Reading, MA, 1963.
- [24] Halliday, David, et al., *Fundamentals of Physics*, John Wiley & Sons, Inc., New York, 1981.
- [25] Hylton, Nola, "Computational Techniques for the Simulation and Evaluation of Hydrogen NMR Imaging Methods", Ph.D. dissertation Stanford University, 1985.
- [26] Shah, Ajit, "Investigation of Optimal Radio Frequency Pulse Modulation Techniques for Variable Flip Angle Magnetic Resonance Imaging", Ph.D. dissertation, University of California, Berkeley, 1988.
- [27] Chen, Jyh-Horng, "In-vivo Measurements of MRI Tissue Parameters at Various Magnetic Field Strengths", Ph.D. dissertation, University of California, Berkeley, 1991.
- [28] Chen, Jyh-Horng, et al, "In Vivo Relaxation Times and Hydrogen Density at 0.063-4.85 T in Rats with Implanted Mammary Adenocarcinomas", *Radiology*, vol 184, pp. 427-434, 1992.
- [29] Kaufman, Leon, et al, "Accessible Magnetic Resonance Imaging", *Magnetic Resonance Quarterly*, vol 5:4, pp. 283-297
- [30] Ortendahl, Douglas, et al, "Analytical Tools for Magnetic Resonance Imaging", *Radiology*, vol 153, pp. 479-488, 1984.

- [31] Schamroth, Leo, *The Disorders of Cardiac Rhythm*, Blackwell Scientific Publications, Oxford, 1980.
- [32] Phillips, R. E., *The Cardiac Rhythms, A Systematic Approach To Interpretation*, W.B. Saunders Company, Philadelphia, 1973.
- [33] Ziemer, R. E., *Principles of Communications*, Houghton Mifflin Company, Boston, 1985.
- [34] Oppenheim, Alan V., et al., *Signals and Systems*, Prentice-Hall, New Jersey, 1983.
- [35] Kaufman, Leon, et al, "Measuring Signal-to-Noise Ratios in MR Imaging", *Radiology*, vol 173, pp. 265-267, 1989.
- [36] Bevington, Philip R., *Data Reduction and Error Analysis for the Physical Sciences*, McGraw-Hill Book Company, New York, 1969.
- [37] Oppenheim, Alan V., *Discrete-Time Signal Processing*, Prentice-Hall, Inc., New Jersey, 1989.
- [38] Shosa, Dale, Kaufman, Leon, "Methods for Evaluation of Diagnostic Imaging Instrumentation", *Phys. Med. Biol.*, vol 26:1, pp. 101-112, 1981.
- [39] Hanson, Kenneth M., Boyd, Douglas P., "The Characteristics of Computed Tomographic Reconstruction Noise and Their Effect on Detectability", *IEEE Transactions on Nuclear Science*, vol NS25:1, pp. 160-163, 1978.
- [40] Protter, Murray H., *Modern Mathematical Analysis*, Addison-Wesley Publishing Company, Reading, MA, 1964.
- [41] Foley, James D., Van Dam, Andries, *Fundamentals of Interactive Computer Graphics*, Addison-Wesley Publishing Company, Reading, MA, 1982.

- [42] Bohning, DE, et al, "PC-Based System for Retrospective Cardiac and Respiratory Gating of NMR Data", *Magnetic Resonance in Medicine*, vol 16:2, pp. 303-316, 1990.

APPENDIX

PATIENT STUDY CARDIAC PARAMETER MEASUREMENTS

Patient ID #		a	a	b	b	c	c
MR DIA LA LV LENGTH	(mm)	75.65	73.45	73.38	70.36	69.51	65.35
MR SYS LA LV LENGTH	(mm)	45.45	56.69	53.45	60.16	57.62	43.83
ECHO DIAS LA LV LENGTH	(mm)	91.67	99.00	80.00	91.00	84.00	83.33
ECHO SYS LA LV LENGTH	(mm)	71.33	81.00	68.33	72.00	68.00	60.67
MR DIA SA LV BPAVWI	(mm)	46.98	42.79	42.55	42.54	38.59	34.24
MR SYS SA LV BPAVWI	(mm)	34.86	30.20	30.05	31.34	31.77	25.90
MR SM LA EDV	(ml)	136.83	115.62	135.99	119.81	86.27	113.94
MR SM LA ESV	(ml)	57.45	44.86	49.12	49.54	23.49	23.13
MR SM SA EDV	(ml)	125.89	108.08	118.91	121.09	111.80	101.45
MR SM SA ESV	(ml)	61.18	59.03	39.85	44.77	42.72	27.28
MR BIPLANE EDV	(ml)	138.60	107.39	116.53	103.97	85.16	64.16
MR BIPLANE ESV	(ml)	50.90	44.44	39.45	52.74	51.41	23.65
ECHO BIPLANE EDV	(ml)	131.65	150.03	92.84	126.97	72.57	76.96
ECHO BIPLANE ESV	(ml)	54.76	59.22	37.46	43.41	20.02	23.98
MR AREA LENG EDV	(ml)	174.70	128.18	125.08	113.83	84.38	57.44
MR AREA LENG ESV	(ml)	65.50	54.94	33.91	52.74	44.28	27.26
MR SM LA MYOC MASS	(gm)	141.91	152.48	140.05	145.40	122.18	143.99
MR SM SA MYOC MASS	(gm)	134.35	145.79	136.90	186.88	207.83	131.55
MR TE MYOC MASS	(gm)	205.24	197.29	213.82	199.98	205.96	158.78
MR ALENG MYOC MASS	(gm)	227.54	218.50	237.19	219.22	228.94	176.14
ECHO TE MYOC MASS	(gm)	142.23	173.47	147.87	172.30	153.36	135.57
MYOC SA AVE THICK	(mm)	12.69	11.59	13.44	12.77	15.06	12.73

Table A.1 Magnetic resonance and echocardiographic cardiac functional parameters measured from the patient study described in Section 6.1.

These abbreviations apply to the data table presented in this Appendix:

ALENG = Area Length	AVE = Average
BPAVWI = Biplane Average Width	DIA = Diastolic
ECHO = Echocardiographic	EDV = End Diastolic Volume
ESV = End Systolic Volume	LA = Long Axis
LV = Left Ventricle	MR = Magnetic Resonance
MYOC = Myocardial Mass	MYOC MASS = Myocardial Mass
SA = Short Axis	SM = Summed Mult-slice
SYS = Systolic	TE = Truncated Ellipse
THICK = Thickness	

PATIENT STUDY CARDIAC PARAMETER MEASUREMENTS (CONT.)

Patient ID #	d	e	f	g	h	i
MR DIA LA LV LENGTH (mm)	72.01	64.89	75.13	84.48	77.94	103.85
MR SYS LA LV LENGTH (mm)	53.39	46.34	48.65	67.14	56.03	64.90
ECHO DIAS LA LV LENGTH (mm)	90.00	98.33	89.67	101.67	91.00	95.00
ECHO SYS LA LV LENGTH (mm)	68.67	81.67	72.33	84.00	75.33	73.00
MR DIA SA LV BPAVWI (mm)	35.17	41.64	43.95	39.66	34.31	38.69
MR SYS SA LV BPAVWI (mm)	23.63	27.72	21.92	31.61	30.23	24.05
MR SM LA EDV (ml)	92.25	119.29	179.83	120.50	103.46	126.59
MR SM LA ESV (ml)	42.49	41.94	50.75	46.96	35.04	39.10
MR SM SA EDV (ml)	108.56	118.08	154.40	111.40	101.68	116.32
MR SM SA ESV (ml)	39.28	41.91	57.32	45.53	51.04	41.60
MR BIPLANE EDV (ml)	79.94	93.34	131.68	102.61	82.00	117.95
MR BIPLANE ESV (ml)	26.85	31.23	48.69	56.23	41.06	29.53
ECHO BIPLANE EDV (ml)	99.14	105.96	114.86	116.74	108.00	124.64
ECHO BIPLANE ESV (ml)	37.74	47.15	43.84	38.83	33.90	35.17
MR AREA LENG EDV (ml)	91.09	99.51	117.00	112.97	95.22	109.25
MR AREA LENG ESV (ml)	27.14	33.06	25.10	63.38	54.51	26.01
MR SM LA MYOC MASS (gm)	106.24	98.86	182.34	131.65	153.54	161.95
MR SM SA MYOC MASS (gm)	114.14	145.40	202.42	170.18	203.83	170.93
MR TE MYOC MASS (gm)	133.74	179.54	257.07	208.07	167.06	203.52
MR ALENG MYOC MASS (gm)	146.35	194.53	284.85	232.74	185.30	225.12
ECHO TE MYOC MASS (gm)	130.43	183.20	182.93	169.87	145.20	176.80
MYOC SA AVE THICK (mm)	9.70	12.51	12.96	11.87	13.11	12.46

Table A.1 (continued) Magnetic resonance and echocardiographic cardiac functional parameters measured from the patient study described in Section 6.1.

These abbreviations apply to the data table presented in this Appendix:

ALENG = Area Length

AVE = Average

BPAVWI = Biplane Average Width

DIA = Diastolic

ECHO = Echocardiographic

EDV = End Diastolic Volume

ESV = End Systolic Volume

LA = Long Axis

LV = Left Ventricle

MR = Magnetic Resonance

MYOC = Myocardial Mass

MYOC MASS = Myocardial Mass

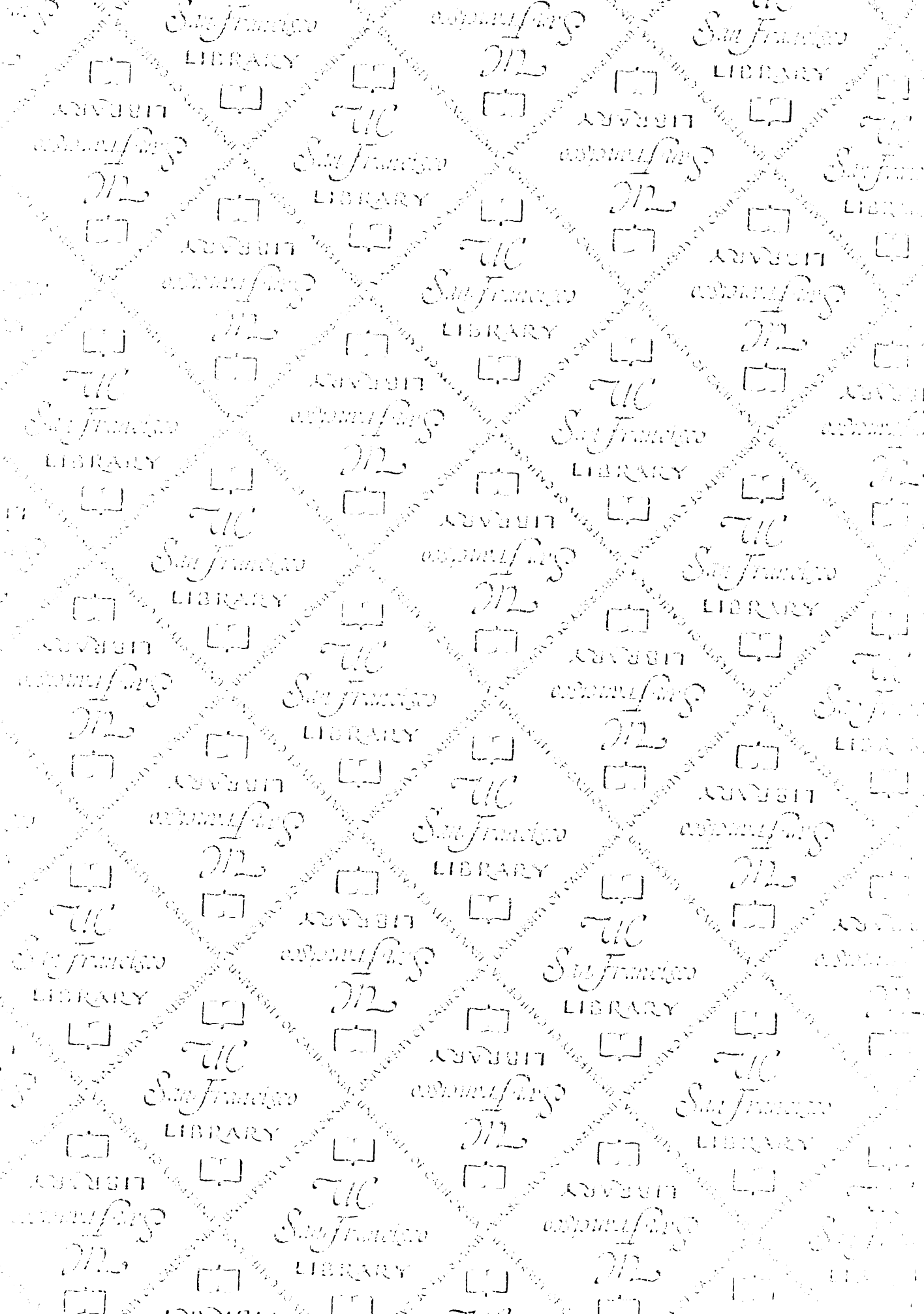
SA = Short Axis

SM = Summed Mult-slice

SYS = Systolic

TE = Truncated Ellipse

THICK = Thickness



For reference

Not to be taken from the room.

6354339



3 1378 00635 4339

